THE PROBLEMATIC ASPECTS OF ENERGY EFFICIENCY '25

EDITORS

MACIEJ ZAJKOWSKI • ZBIGNIEW SOŁJAN

Politechnika Białostocka

THE PROBLEMATIC ASPECTS OF ENERGY EFFICIENCY '25

Editors
Maciej Zajkowski, Zbigniew Sołjan

Politechnika
Białostocka

OFICYNA WYDAWNICZA POLITECHNIKI BIAŁOSTOCKIEJ
BIAŁYSTOK 2026

Reviewers:
Prof. Tomasz Popławski, PhD, DSc, Eng
Marcin Wesołowski, PhD, DSc, Eng

Science editor in the discipline of automation, electronic and electrical engineering:
Prof. Jan Dorosz, PhD, DSc

Copy editor:
Aniela Staszewska, Katarzyna Duniewska

DTP & cover of a book:
Marcin Dominów

ISBN 978-83-68673-38-8 (e-Book)
DOI: 10.24427/978-83-68673-38-8

Publishing House of Bialystok University of Technology
Wiejska 45C, 15-351 Białystok
e-mail: oficyna.wydawnicza@pb.edu.pl
www.pb.edu.pl

Table of contents

Wstęp

Współczesna energetyka znajduje się w okresie intensywnych przemian, wynikających zarówno z rosnących wymagań środowiskowych, jak i dynamicznego rozwoju technologii. Transformacja w kierunku systemów niskoemisyjnych, rozproszonych i inteligentnych wymaga interdyscyplinarnego podejścia, łączącego zagadnienia związane z wytwarzaniem, magazynowaniem i efektywnym wykorzystaniem energii, a także z jej pomiarem, dystrybucją i wpływem na otoczenie.

Niniejsza monografia wpisuje się w ten nurt, prezentując szerokie spektrum zagadnień związanych z nowoczesnymi systemami energetycznymi i technologiami wspierającymi zrównoważony rozwój. Szczególne miejsce zajmują tu rozwiązania oparte na odnawialnych źródłach energii oraz ich integracji z infrastrukturą techniczną, co ma kluczowe znaczenie dla stabilności i elastyczności współczesnych systemów elektroenergetycznych. Równolegle podjęto problematykę lokalnych struktur energetycznych oraz ich roli w kształtowaniu bezpieczeństwa energetycznego i efektywnego zarządzania zasobami na poziomie regionalnym.

Istotnym aspektem poruszanym w monografii są również zagadnienia związane z efektywnością energetyczną oraz wykorzystaniem energii w różnych obszarach techniki – od systemów bezprzewodowego przesyłu energii, przez technologie wykorzystujące niskotemperaturowe źródła ciepła, aż po rozwiązania ograniczające emisję zanieczyszczeń. Uzupełnieniem tych rozważań są analizy wpływu materiałów i struktur technicznych na propagację sygnałów oraz rozwój systemów monitorowania środowiskowego opartych na technologii internetu rzeczy.

Nie bez znaczenia pozostają także zagadnienia pomiarowe, które stanowią fundament oceny efektywności i poprawności działania systemów energetycznych. W tym kontekście szczególną uwagę zwrócono na dokładność i uwarunkowania pomiarów w systemach cieplnych, co ma bezpośrednie przełożenie na ich eksploatację oraz rozliczenia energetyczne.

Monografia stanowi próbę uchwycenia aktualnych kierunków rozwoju energetyki i technologii pokrewnych w sposób spójny i przekrojowy. Zebrane prace ukazują, że skuteczne wdrażanie nowoczesnych rozwiązań wymaga nie tylko zaawansowanej wiedzy technicznej, lecz także integracji różnych obszarów inżynierii oraz uwzględnienia uwarunkowań środowiskowych i społecznych. Publikacja skierowana jest do badaczy, inżynierów oraz wszystkich osób zainteresowanych praktycznymi i teoretycznymi aspektami współczesnej energetyki.

Introduction

The contemporary energy sector is undergoing a period of profound transformation, driven both by increasing environmental requirements and the rapid development of technology. The transition towards low-emission, decentralised and intelligent systems necessitates an interdisciplinary approach that combines issues related to energy generation, storage and efficient utilisation, as well as its measurement, distribution and impact on the environment.

This monograph aligns with these developments by presenting a broad spectrum of topics related to modern energy systems and technologies supporting sustainable development. Particular emphasis is placed on solutions based on renewable energy sources and their integration with technical infrastructure, which is crucial for the stability and flexibility of contemporary power systems. At the same time, attention is given to local energy structures and their role in shaping energy security and effective resource management at the regional level.

An important aspect addressed in the monograph concerns energy efficiency and the utilisation of energy across various fields of engineering – from wireless power transfer systems, through technologies harnessing low-grade heat sources, to solutions aimed at reducing pollutant emissions. These considerations are complemented by analyses of how materials and structural solutions influence signal propagation, as well as the development of environmental monitoring systems based on Internet of Things technologies.

Equally significant are measurement-related issues, which form the foundation for evaluating the performance and reliability of energy systems. In this context, particular attention is paid to the accuracy and conditions of measurements in thermal systems, which directly affect their operation and energy billing.

The monograph represents an attempt to capture current trends in the development of energy systems and related technologies in a coherent and comprehensive manner. The collected works demonstrate that the effective implementation of modern solutions requires not only advanced technical knowledge but also the integration of various engineering domains and consideration of environmental and societal factors. The publication is intended for researchers, engineers, and all those interested in both the theoretical and practical aspects of contemporary energy systems.

DOI: 10.24427/978-83-68673-38-8_1

Chapter 1. Analysis of the structures and areas of activity of energy clusters depending on the type of region in Poland

Zbigniew SKIBKO[1], *Magdalena BUTKIEWICZ*[2]
Bialystok University of Technology, Faculty of Electrical Engineering,
[1]*ORCID: 0000-0002-5238-6019, e-mail: z.skibko@pb.edu.pl,* [2]*e-mail: 86081@student.pb.edu.pl*

Streszczenie. W rozdziale przedstawiono analizę funkcjonowania klastrów energii w dwóch odmiennych regionach Polski – województwach podlaskim i śląskim – w celu określenia wpływu uwarunkowań społeczno-gospodarczych na ich strukturę organizacyjną i zakres działalności. Wyniki wykazały wyraźne różnice pomiędzy badanymi regionami. Profil społeczno-gospodarczy regionu silnie wpływa na charakter i efektywność funkcjonowania klastrów energii. W regionach rolniczych, takich jak województwo podlaskie, pełnią one funkcję integracyjną i zabezpieczającą potrzeby lokalnych społeczności, natomiast w regionach uprzemysłowionych, jak województwo śląskie, stają się platformami współpracy międzysektorowej, sprzyjającymi wdrażaniu innowacji technologicznych i transferowi wiedzy. W województwie podlaskim klastry mają głównie charakter społeczno-usługowy, oparty na współpracy samorządów, spółek komunalnych i instytucji publicznych. Dominującymi obszarami działalności są: produkcja energii (26%) i bilansowanie zapotrzebowania (26%), natomiast magazynowanie i handel energią występują rzadziej. W województwie śląskim klastry przyjmują formę bardziej techniczno-przemysłową, obejmującą spółki komunalne, przedsiębiorstwa przemysłowe, miasta na prawach powiatu i jednostki badawcze. Tam dominują działania związane z produkcją energii (27%) i bilansowaniem zapotrzebowania (26%), ale także z jej dystrybucją (18%) i magazynowaniem (16%).

Abstract. The chapter presents an analysis of the functioning of energy clusters in two different regions of Poland – Podlaskie and Śląskie Provinces – in order to determine the impact of socio-economic conditions on their organisational structure and scope of activity. The results showed clear differences between the regions studied. The socio-economic profile of a region has a strong influence on the nature and effectiveness of energy clusters. In agricultural regions, such as the Podlaskie Province, they perform an integrative function and secure the needs of local communities, while in industrialised regions, such as the Śląskie Province, they become platforms for cross-sectoral cooperation, conducive to the implementation of technological innovations and knowledge transfer. In the Podlaskie Province, clusters are mainly social and service-oriented, based on cooperation between local governments, municipal companies and public institutions. The dominant areas of activity are energy production (26%) and demand balancing (26%), while energy storage and trading are less common. In the Śląskie Province, clusters take a more technical and industrial form, involving municipal companies, industrial enterprises, cities with county rights and research units. Activities related to energy production (27%) and demand balancing (26%) dominate there, but also energy distribution (18%) and storage (16%). (

Słowa kluczowe: klaster energii, województwo podlaskie, województwo śląskie, OZE

Keywords: energy cluster, Podlaskie Province, Śląskie Province, RES

Introduction

In recent years, there has been a dynamic increase in interest in renewable energy sources (RES), which are increasingly finding their way into both homes and industrial consumers [1]. Renewable energy sources are an excellent alternative to fossil fuels, which generate significant amounts of greenhouse gases and intensify the process of global climate change [2, 3]. Global warming caused by greenhouse gas (GHG) emissions is a serious challenge and a key issue in modern environmental protection. It is the source of serious health problems, weather changes, rising sea levels and changes in the ecosystem [4, 5]. The industrial and energy sectors are considered to be the main sources of greenhouse gas emissions [6]. In the face of rising global temperatures and increasingly extreme weather events, it is becoming urgent to implement sustainable energy solutions [7]. At the heart of these efforts is the urgent need to move away from fossil fuels towards clean, sustainable and efficient energy solutions. This is a response not only to the growing demand for energy, but also to the need to protect the planet and ensure a secure future for future generations [7].

Currently, energy-related issues in Poland are governed by numerous legal regulations designed to help European Union countries transition to a green economy. The goal is to achieve climate and resource neutrality and reduce dependence on fossil fuels. All planned measures are included in: climate strategies for 2030 and 2050, directives on energy from renewable sources, directives on energy efficiency, the Effort Sharing Regulation (ESR) and the EU Emissions Trading System (EU ETS) [8, 9]. The implementation instrument is the 'Fit for 55' package, which is intended to help implement the objectives of the European Climate Law in practice. Among other things, it includes a requirement to reduce emissions by 55% by 2030 compared to 1990 levels, and a requirement to achieve net-zero greenhouse gas emissions by 2050. This means that by 2050, greenhouse gas emissions in the EU are to be offset by their absorption [8, 9, 10, 11]. To meet the expectations set out in European Union legislation, many changes need to be made in the energy sector, industry, agriculture and socio-economic systems. [12,13]. Renewable energy sources (RES) play a key role in the transition [14]. Energy cooperatives and energy clusters are to help achieve the energy target.

An energy cluster is an agreement whose subject matter is cooperation in the generation, storage, balancing of demand, and distribution of electricity or heat, with the aim of providing its parties with economic, social, and environmental benefits or increasing the flexibility of the power system. An energy cluster agreement must be concluded in writing under pain of nullity. The agreement should primarily include the rights and obligations of the parties, the scope of cooperation, the area of activity with an indication of energy consumption points and points of entry into the grid, and the authorisation of the energy cluster coordinator to access energy market information and measurement data for each member of the cluster. Prior to the amendment (Act of 20 February 2015), the regulations did not cover energy storage as part of the cluster's activities. The amendment to the regulations in 2023 not only enabled the accumulation of surplus energy, which allows for more efficient management of its consumption, but also increased the energy security of cluster participants by reducing the risk of supply interruptions [15, 16, 17].

The area of operation of an energy cluster is determined on the basis of the location of energy consumption points. The registration of a cluster defines its territorial boundaries – covering the area of one district or a maximum of five neighboring municipalities – and imposes an obligation on local government units or enterprises controlled by them to participate. The cluster's activities may not include cross-border connections with other countries. Only entities connected to the distribution network of the same electricity distribution system operator with a rated voltage below 110 kV may be members of the cluster [15, 16, 17]. There are currently several hundred energy clusters operating in Poland, but the most majority of them are not listed in the register kept by the President of the Energy Regulation Office. Registration of an energy cluster is voluntary, but it allows access to available support mechanisms, such as exemption from the RES fee and the cogeneration fee [16, 17].

The scope of activity of an energy cluster may vary and be adapted to local technical, social and economic conditions, covering many areas of activity [18]:

- generation of electricity and heat based on conventional fuels (including cogeneration, i.e. simultaneous generation of energy and heat);
- generation of electricity and heat from various renewable energy sources;
- production of gaseous and liquid fuels;
- distribution of electricity, heat and fuels within its own distribution system;
- sale of energy or fuels to end users at attractive prices;
- production and distribution or sale of cooling;
- storage of energy or energy carriers;
- management of agricultural waste;
- management of household waste;
- management of forest waste;
- utilisation of the energy potential of local watercourses and other forces of nature.

Despite the dynamic growth in the number of publications devoted to energy communities and microgrids, there is still a noticeable shortage of in-depth research on the actual functioning of energy clusters in Polish regions, especially in rural areas such as the Podlaskie Province. The existing literature focuses mainly on theoretical aspects, the optimisation of energy management systems (EMS) and the analysis of individual cases, neglecting a broader comparative approach. There is a lack of comprehensive empirical analyses showing how the institutional structure of a cluster – comprising municipalities, enterprises, social organisations and universities – affects its operational profile, including energy production, storage and balancing, as well as the degree of utilisation of local renewable energy sources (RES).

To fill this gap, this study proposes a comparison of energy clusters operating in two regions: the Podlaskie Province, representing an area with a dispersed settlement structure and an agricultural economy, and the Silesian Province, characterised by a high degree of urbanisation, developed industrial infrastructure and greater access to capital. A comparison of these two types of regions will allow us to identify how differences in socio-economic conditions translate into the organisation, functioning and effectiveness of energy clusters.

Analysis of clusters in the Podlaskie Province

Table 1 presents the results of a review of energy clusters operating in the Podlaskie Province (as of 26 October 2025). The analysis includes the identification of cluster members and their nature (local government units, companies, educational institutions, social welfare homes etc.).

TABLE 1. Energy clusters in the Podlaskie Province

Klaster Jaćwing	• Urząd Gminy Szypliszki • Urząd Gminy Rutka-Tartak • Energia Przyszłości Filipów Sp. z o. o. • WWP "American-Plastic Bis" Andrzej Markiewicz
Klaster Energii – EKOOPER	• Gmina Zabłudów • Politechnika Białostocka • Uniwersytet Medyczny • Zakład Doskonalenia Zawodowego w Białymstoku
Klaster Powiatu Białostockiego	• Powiat Białostocki • Dom Pomocy Społecznej w Choroszczy • Dom Pomocy Społecznej w Uhowie • I Liceum Ogólnokształcące im. Adama Mickiewicza w Łapach • Centrum Kształcenia Zawodowego w Łapach • Zespół Szkół w Czarnej Białostockiej • Dom Dziecka w Supraślu • Dom Pomocy Społecznej "Jawor" w Jałówce • Zespół Szkół Mechanicznych im. Stefana Czarnieckiego w Łapach • Powiatowy Zarząd Dróg w Białymstoku • Powiatowy Środowiskowy Dom Pomocy w Łaźniach

Klaster Energii Powiatu Monieckiego	• Gmina Goniądz • Gmina Jasionówka • Gmina Jaświły • Gmina Krypno • Gmina Mońki • Moniecka Spółdzielnia Mleczarska w Mońkach • Przedsiębiorstwo Energetyki Cieplnej w Mońkach Sp. z o. o.
Klaster Energi Sokólsko-Białostocki	• Gmina Supraśl • Gmina Krynki • Gmina Szudziałowo • Powiat Sokólski
Klaster EnergyREGION Michałowo	• Gmina Michałowo • Gmina Gródek • Gmina Tykocin • Gmina Zabłudów • Zielona Energia Michałowo • IEN Energy Sp. z o. o. • Dom Pomocy Społecznej "Jawor" • Gminny Ośrodek Kultury w Michałowie
Klaster Energii Gmin Powiatu Sokólskiego	• Gmina Dąbrowa Białostocka • Gmina Janów • Gmina Kuźnica • Gmina Nowy Dwór • Gmina Suchowola • Gmina Sidra • Powiat Sokólski • DOEKO Group Sp. z o. o.
Białostocki Klaster Energetyczny	• Wodociągi Białostockie Sp. z o. o. • Miasto Białystok • PUHP LECH Sp. z o. o.
Siemiatycki Klaster Energii	• Miasto Siemiatycze • Przedsiębiorstwo Komunalne Sp. z o. o. • Gmina Dziadkowice • Gmina Mielnik • Powiat Siemiatycki • Samodzielny Publiczny Zakład Opieki Zdrowotnej • Eneris Sp. z o. o.
Nowa Suwalska Energia	• Przedsiębiorstwo Energetyki Cieplnej w Mońkach Sp. z o. o. • Park Naukowo-Technologiczny • Przedsiębiorstwo Wodociągów i Kanalizacji • Suwalskie Kopalnie Surowców Mineralnych • Miasto Suwałki • Malow

An analysis of the composition of energy clusters reveals considerable diversity – from structures dominated by municipalities and public institutions, through hybrid arrangements involving municipal companies, to initiatives with a strong educational background involving universities. They are accompanied by limited liability companies established by local governments to perform tasks in the field of energy and municipal services. The role of local government units as the main coordinator and organisational stabiliser remains unchanged, which results from the requirements of the Act [15, 16].

Analysis of cluster structures in the Podlaskie Province

Figs. 1 and 2 present the results of an analysis of the internal organisational structure of energy clusters, with particular emphasis on the typology and number of members and the profile of activities (energy production, storage, balancing, trading). The Podlaskie Province is characterised by a dispersed settlement structure, a predominance of rural areas and an agricultural economy, which determines the specific nature and form of local energy initiatives.

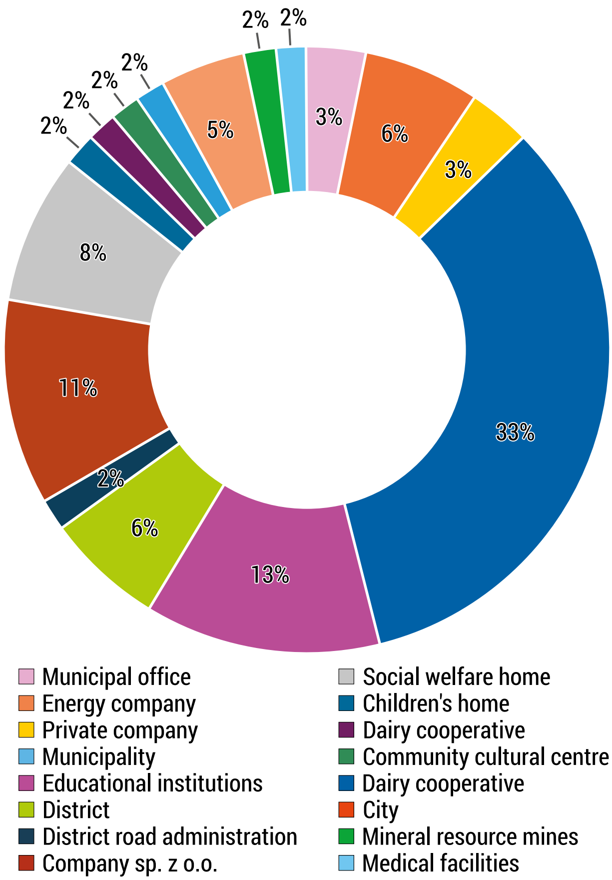

FIGURE. 1. Percentage share of institutions comprising the cluster in the Podlaskie Province

An analysis of the data presented in Fig. 1 shows that clusters in the Podlaskie Province most often consist of municipalities, followed by limited liability companies and social care homes. Municipalities and companies are most often involved because the law imposes an obligation on local government units or companies controlled by them to participate.

Each cluster has its own activity profile. One cluster may have several activity profiles. Most often, clusters are involved in energy production (26%) and balancing electricity demand (26%) – Fig. 2. This is followed by energy storage (20%) and energy trading (14%). Only one cluster reported activities in the field of heat production.

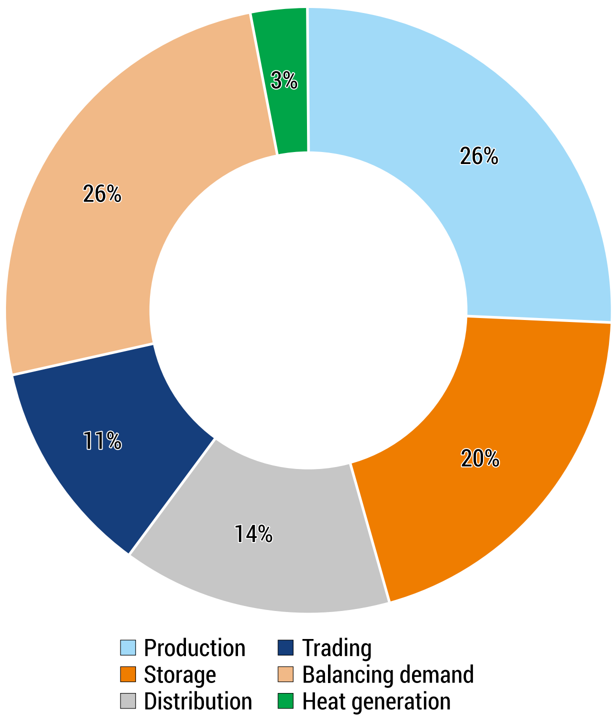

FIGURE 2. Percentage distribution of cluster activity sectors

Analysis of clusters in the Śląskie Province

Table 2 presents the results of a review of energy clusters operating in the Śląskie Province (as of 26 October 2025). Unlike the Podlaskie Province, this region is characterised by a high level of urbanisation, a significant concentration of industry and a well-developed technical infrastructure.

TABLE 2. **Clusters of the Silesian Province**

Klaster Energii w Gliwicach	Smart EPC Sp. z o. o. • Gliwice – miasto na prawach powiatu • Katowicka Specjalna Strefa Ekonomiczna S.A. Podstrefa Gliwice • Śląskie Centrum Logistyki S.A. • Przedsiębiorstwo Energetyki Cieplnej – Gliwice Sp. z o. o. • Przedsiębiorstwo Komunikacji Miejskiej Sp. z o. o. • Przedsiębiorstwo Wodociągów i Kanalizacji Sp. z o. o. • Przedsiębiorstwo Zagospodarowania Odpadów Sp. z o. o. • Śląska Sieć Metropolitalna Sp. z o. o. • ZPBE Energopomiar Sp. z o. o.
Ruda Śląska Klaster Energii i Wodoru	• Miasto Ruda Śląska • Przedsiębiorstwo Wodociągów i Kanalizacji Sp. z o. o. w Rudzie Śląskiej • Miejskie Przedsiębiorstwo Gospodarki Mieszkaniowej Towarzystwo Budownictwa Społecznego Sp. z o. o. • Aquadrom • Prezero Service Południe Sp. z o. o. • Węglokoks Energia ZCP Sp. z o. o.
Klaster Rybnicki	• Miasto Rybnik • Gmina Gaszowice • Gmina Jejkowice • Gmina Świerklany • Gmina Czerwionka-Leszczyny • DOEKO GROUP Sp. z o. o.
Klaster Energii Aglomeracji Częstochowskiej	• Gmina Miasto Częstochowa • Gmina Poczesna • Gmina Olsztyn • Gmina Mstów • Gmina Rędziany • DOEKO Group Sp. z o. o.
Klaster Eenergii Powiatu Częstochowskiego	• Gmina Blachownia • Gmina Koniecpol • Gmina Mykanów • Powiat Częstochowski • Gmina Kołomnice • Gmina Konopiska • Gmina Janów • Gmina Kamienica Polska • Gmina Lelów • Gmina Kruszyna • Gmina Dąbrowa Zielona • Gmina Przyrów • Gmina Starcza

Klaster Energii Powiatu Kłobuckiego	• Gmina Kłobuck • Gmina Krzepice • Gmina Lipie • Powiat Kołobucki • Gmina Miedźno • Gmina Opatów • Gmina Panki • Gmina Popów • Gmina Przystajń • Gmina Wręczyca Wielka • Związek Gmin i Powiatów Subregionu Północnego Województwa Śląskiego
Klaster Energii Powiatu Myszkowskiego	• Miasto Myszków • Gmina i Miasto Koziegłowy • Gmina Niegowa • Gmina Poraj • Powiat Myszkowski • DOEKO Group Sp. z o. o. • Związek Gmin i Powiatów Subregionu Północnego Województwa Śląskiego
Klaster Energii Ziemi Wodzisławskiej	• Miasto Rydułtowy • Miasto Radlin • Miasto Pszów • Gmina Marklowice • Gmina Godów • Gmina Mszana • Gmina Gorzyce • DOEKO Group Sp. z o. o.
Katowicki Klaster Energii	• Katowickie Inwestycje S.A. • Katowicka Specjalna Strefa Ekonomiczną S.A. • Miejskie Przedsiębiorstwo Gospodarki Komunalnej Sp. z o. o. • Katowickie Wodociągi S.A. • Katowickie Towarzystwo Budownictwa Społecznego Sp. z o. o. • Przedsiębiorstwo Komunikacji Miejskiej Katowice Sp. z o. o. • Narodowa Orkiestra Symfoniczna Polskiego Radia • Dalkia Polska Energia S.A. • Gonar-Bis Sp. z o. o.
Dąbrowski Klaster Energii	• Dąbrowskie Wodociągi – Nemo Wodny Świat • Zagłębiowskie Centrum Onkologii • Enalpha S.A. • Instytut Gospodarczy • Miasto Dąbrowa Górnicza
Klaster Energii Gmin i Powiatu Cieszyńskiego	• Powiat Cieszyński • Gmina Chybie • Gmina Wisła • Gmina Hażlach • Gmina Strumień • Gmina Ustroń • Gmina Zebrzydowice • Gmina Istebna • Gmina Goleszów • Agencja Rozwoju Regionalnego S.A. • Stowarzyszenie Samorządowe Ziemi Cieszyńskiej • Wodociągi Ziemi Cieszyńskiej Sp. z o. o.

Klaster Energii Zielone Bielsko-Biała	• Miasto Bielsko-Biała • Agencja Rozwoju Regionalnego S.A. • MZK Sp. z o. o. • ZIAD S.A. • AQUA S.A. • Zakład Gospodarki Odpadami S.A. • Therma Sp. z o. o. • Beskidzki Hurt Towarowy S.A. • PreZero S.A. • KSSE S.A. • TBS Sp. z o. o. • Parafia Ewangelicko-Augsburska w Bielsku-Białej
Klaster Energii Powiatu Bielskiego	• Gmina Bestwina • Gmina Wilamowice • Gmina Porąbka • Gmina Kozy • Gmina Wilkowice • Gmina Buczkowice • Gmina Szczyrk • Gmina Jaworze • Gmina Jasienica • EKO-WTÓR Jakubiec Sp. z o. o. • Agencja Rozwoju Regionalnego S.A. • Powiat Bielski
Klaster Energii "Przyjazna Energia w Powiecie Gliwickim"	• Gmina Wielowieś • Gmina Toszek • Gmina Rudziniec • Gmina Sośnicowice • Gmina Pilchowice • Gmina Knurów • Gmina Gierałtowice • Gmina Pyskowice • Przyjazna Energia Sp. z o. o.
Tyski Klaster Energii	• Miasto Tychy • Miasto Bieruń • Katowicka Specjalna Strefa Ekonomiczna S.A. • Regionalne Centrum Gospodarki Wodno-Ściekowej S.A. • Master – Odpady i Energia Sp. z o. o. • Okręgowa Spółdzielnia Mleczarska w Bieruniu • Przedsiębiorstwo Energetyki Cieplnej Sp. z o. o. • Sertop Sp. z o. o. • Tyskie Linie Trolejbusowe Sp. z o. o. • Bieruńskie Przedsiębiorstwo Inżynierii Komunalnej Sp. z o.o.
Bytomski Klaster Energii	• Gmina Bytom • Bytomskie Wodociągi Sp. z o. o. • Przedsiębiorstwo Energetyki Cieplnej Sp. z o. o. • Katowicka Specjalna Strefa Ekonomiczna S.A.

Zawierciański Klaster Energii	• Miasto Zawiercie • Zakład Gospodarki Komunalnej Sp. z o. o. • Spółdzielnia Socjalna Zielone Śląskie • Klastry Energii Sp. z o. o. • Zakład Komunikacji Miejskiej Sp. z o. o. • Rejonowe Przedsiębiorstwo Wodociągów i Kanalizacji Sp. z o. o. • Dabex Sp. z o. o. • Elgum Automotive Sp. z o. o. • Grupa Łapaj Sp. z o. o. • Lindem Sp. z o. o. • AXA Stenman Poland Sp. z o. o.
Ogrodzieniecki Klaster Energii	• Miasto Ogrodzieniec • ZAMEK Sp. z o. o. • Przedsiębiorstwo Komunalne Sp. z o. o. • Fundacja Bonera • Klastry Energii Sp. z o. o.
Orzeski Klaster Energii	• Miasto Orzesze • Spółdzielnia Socjalna Zielone Śląskie • Gmina Ornontowice • Klastry Energii Sp. z o. o.
Klaster Energii Zabrzańskie Innowacje Energetyczne	• Miasto Zabrze • KOMAG ENERGIA Sp. z o. o. • Instytut Techniki Górniczej KOMAG • Instytut Technologii Paliw i Energii • Miejski Ośrodek Sportu i Rekreacji Sp. z o. o. • Zabrzańskie Przedsiębiorstwo Energetyki Cieplnej Sp. z o. o. • Stadion w Zabrzu Sp. z o. o. • Zabrzańskie Przedsiębiorstwo Wodociągów i Kanalizacji Sp. z o. o. • Muzeum Górnictwa Węglowego w Zabrzu
Klaster Energii Racibórz	• Miasto Racibórz • Przedsiębiorstwo Komunalne Sp. z o. o. • Wodociągi Raciborskie Sp. z o. o. • Zakład Zagospodarowania Odpadów Sp. z o. o. • Klastry Energii Sp. z o. o.
Klaster Energii Bobrowniki--Wojkowice	• Gmina Bobrowniki • Gmina Psary • Miasto Wojkowice • SIM Zagłębie Sp. z o. o. • Klastry Energii Sp. z o. o.

A summary of data on energy clusters in the Śląskie Province reveals their clearly differentiated institutional structure, with a dominant share of municipal, infrastructure and industrial entities. Unlike the more community-based model of Podlaskie clusters, Śląska energy initiatives are mainly based on municipal companies, energy operators, water supply, heating and transport companies, reflecting the highly urbanised and industrialised nature of the region. Cities with county rights and special economic zones also play a significant role, providing access to capital, technology and investment facilities. Research institutes and scientific and technical units, such as KOMAG and the Institute of Fuel and Energy Technology, are also present in the membership structures, indicating the growing role of innovation and knowledge transfer in the development of local energy.

Analysis of cluster structures in the Śląskie Province

Figs. 3 and 4 present the results of an analysis of the internal organisational structure of energy clusters, with particular emphasis on the typology and number of members and their activity profile. The data presented in Fig. 3 shows that clusters in the Silesian Province most often consist of municipalities, followed by companies, educational institutions and cities. The least common are institutions such as museums, stadiums, foundations, recreation centres, parishes, associations and medical facilities.

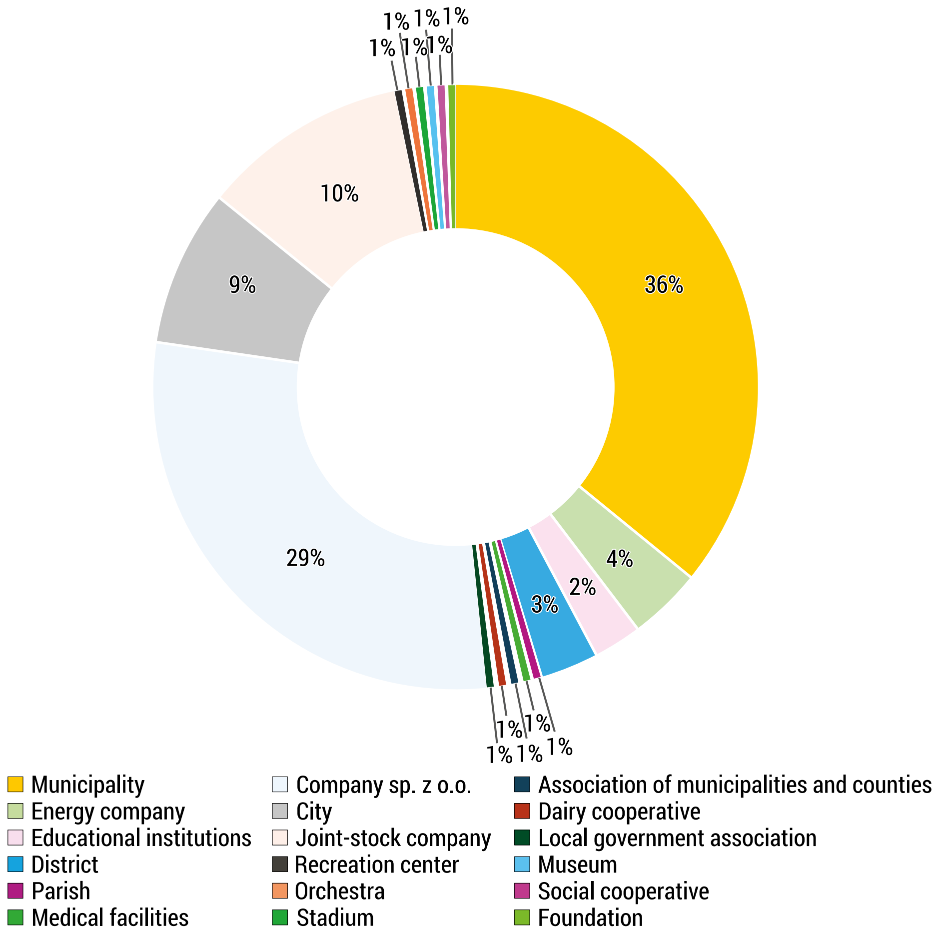

FIGURE 3. Percentage share of institutions comprising the cluster in the Śląskie Province

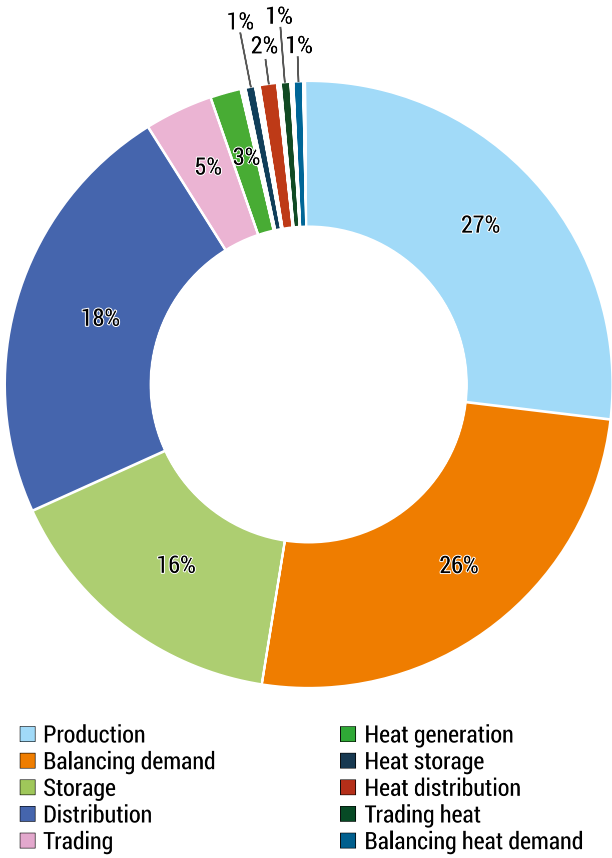

FIGURE 4. **Percentage share of institutions comprising the cluster in the Śląskie Province**

Clusters in the Śląskie Province are most often involved in energy production, demand balancing, distribution and storage – Fig. 4. Broader activity can be observed in the heat generation, storage, distribution and trading sectors. There was no storage, trading, distribution or balancing of heat demand in the Podlaskie Province.

Comparison of clusters in the Podlaskie and Śląskie provinces

In the Podlaskie Province, clusters are mainly based on municipalities (33%), educational institutions (8%) (mostly secondary schools), municipal companies (11%) and care institutions (10%), which translates into the social and service nature of activities and local infrastructure security. The dominant areas of activity are energy production (26%) and demand balancing (26%), with a smaller share of storage (20%) and energy trading (11%). The Podlaskie model therefore focuses on meeting local energy needs, with a strong involvement of local governments and public institutions, which distinguishes it from the more industrial and diversified approach of the Śląskie region.

The Śląskie Province is dominated by municipalities (36%) with a strong share of municipal companies (29%) and educational institutions (10%). The dominant areas of activity are energy production (27%) and demand balancing (26%), with a smaller share of storage (16%) and energy distribution (18%). This structure indicates that Śląskie clusters have more advanced technological and logistical facilities, which allows them to carry out comprehensive activities in the field of energy – from production and distribution to storage and effective management of energy resources.

Although municipalities play an important role in the structure of energy clusters in both regions, the Śląskie Province clearly shows a stronger presence of industrial and infrastructure entities, such as municipal enterprises, service companies, waterworks and heating plants (Table 2). This composition gives Śląskie initiatives a more technical and commercial character, different from the social and service model dominant in Podlaskie clusters.

Summary

The article presented a detailed description and typology of energy clusters operating in the Podlaskie and Śląskie provinces, focusing on their organisational structure and operational profiles. The article presents a summary of the functioning of energy clusters in two extremely different regions of Poland: the Podlaskie and Śląskie provinces (as of 26 October 2025). The results of the analysis reveal significant differences in both institutional structure and activity profiles.

The distribution of sectors of activity among the analysed clusters indicates a strong focus on local energy generation and balancing, coupled with a shortage of storage infrastructure. The lack of adequate energy storage resources limits their ability to respond flexibly to changing market conditions and demand, which may hamper further operational development and integration into the wider energy system. In contrast, the Śląskie clusters (Fig. 4) show a more balanced distribution of activities – in addition to production and balancing, energy distribution and storage are also important, which may indicate a higher degree of technical sophistication and better links to the region's network infrastructure.

The results of the analysis clearly indicate that the socio-economic profile of the region has a significant impact on the organisational structure and functional scope of energy clusters. In agricultural and rural regions, such as the Podlaskie Province, energy clusters primarily serve as integrators of local communities and guarantors of energy security for public sector institutions. In urbanised and industrialised areas, such as the Śląskie Province, clusters function as platforms for cross-sector cooperation, bringing together local government units, industry representatives and the scientific community, which promotes the commercialisation of innovative solutions and technology transfer.

References

[1] Kuźmiński, Ł., Halama, A., Nadolny, M., Dynowska, J. (2023). Economic Instruments and the Vision of Prosumer Energy in Poland. Analysis of the Potential Impacts of the "My Electricity" Program. *Energies*, *16*, 1680. https://doi.org/10.3390/en16041680

[2] González-Niño, M. E., Sierra-Herrera, O. H., Pineda-Muñoz, W. A., Muñoz-Galeano, N., López-Lezama, J. M. (2025). Exploring Technology Trends and Future Directions for Optimized Energy Management in Microgrids. *Information*, *16*, 183. https://doi.org/10.3390/info16030183

[3] Aldoseri, M., Khan, A. M. (2025). Sustainable Development and Environmental Harmony: An Investigation of the Elements Affecting Carbon Emissions Risk. *Sustainability*, *17*, 9468. https://doi.org/10.3390/su17219468

[4] Olabi, A. G., Mohammad Ali Abdelkareem (2022). Renewable energy and climate change. *Renewable and Sustainable Energy Reviews*, *158*, 1364–032. https://doi.org/10.1016/j.rser.2022.112111

[5] Curtin, J., McInerney, C., Gallachóir, B. Ó, Hickey, C., Deane, P., Deeney, P. (2019). Quantifying stranding risk for fossil fuel assets and implications for renewable energy investment: A review of the literature. *Renewable and Sustainable Energy Reviews*, *116*, 109402. https://doi.org/10.1016/j.rser.2019.109402

[6] Dong, H., Ohnishi, S., Fujita, T., Geng, Y., Fujii, M., Dong, L. (2014). Achieving carbon emission reduction through industrial & urban symbiosis: A case of Kawasaki. *Energy*, *64*, 277–286, https://doi.org/10.1016/j.energy.2013.11.005

[7] Rial, R. C. (2024). Biofuels versus climate change: Exploring potentials and challenges in the energy transition. *Renewable and Sustainable Energy Reviews*, *196*, 114369. https://doi.org/10.1016/j.rser.2024.114369

[8] Directorate-General for Research and Innovation (European Commission). (2023). *Scaling up Innovative Technologies for Climate Neutrality: Mapping of EU Demonstration Projects in Energy Intensive Industries*. Publications Office of the European Union. https://data.europa.eu/doi/10.2777/926968

[9] Regulation (EU) 2021/1119. (2021). *Regulation of the European Parliament and of the Council of 30 June 2021 establishing the framework for achieving climate neutrality and amending Regulations (EC) No 401/2009 and (EU) 2018/1999 ('European Climate Law')*. https://eur-lex.europa.eu/eli/reg/2021/1119/oj

[10] European Commission. Directorate General for Internal Market, Industry, Entrepreneurship and SMEs. (2019). *Masterplan for a Competitive Transformation of EU Energy-Intensive Industries Enabling a Climate-Neutral, Circular Economy by 2050*. Publications Office of the European Union. https://data.europa.eu/doi/10.2873/854920

[11] Dhondt, N., Mendez Alva, F., Van Eetvelde, G. (2024). Introducing Industrial Clusters in Multi-Node Energy System Modelling by the Application

of the Industry–Infrastructure Quadrant. *Sustainability*, *16*, 2585. https://doi.org/10.3390/su16062585

[12] Nyangchak, N. (2022). Emerging green industry toward net-zero economy: A systematic review. *Journal of Cleaner Production*, *378*, 134622. https://doi.org/10.1016/j.jclepro.2022.134622

[13] Borowski, P. F. (2025). Renewable energy sources towards a zero-emission economy. *Energy Resources*, *18*, 5473. https://doi.org/10.3390/en18205473

[14] Elkhatat, A., Al-Muhtaseb, S. (2024). Climate Change and Energy Security: A Comparative Analysis of the Role of Energy Policies in Advancing Environmental Sustainability. *Energies*, *17*, 3179. https://doi.org/10.3390/en17133179

[15] Act of 20 February 2015 on Renewable Energy Sources. (2024). Journal of Laws of 2024, item 1361, as amended.

[16] Act of 17 August 2023 amending the Act on Renewable Energy Sources and certain other acts. (2023). Journal of Laws of 2023, item 1762.

[17] Report on the activities of the President of the Energy Regulatory Office in 2024. (2024). Energy Regulatory Office. https://www.ure.gov.pl/pl/urzad/informacje--ogolne/edukacja-i-komunikacja/publikacje/sprawozdania-zdzialaln/2916,Sprawozdania-z-dzialal-nosci-Prezesa-URE.html

[18] Tkaczyk, B., adw. Liżewski, M., Guzowska, J. (2023). Klastry energii i spółdzielnie energetyczne. Kompendium wiedzy. https://mae.com.pl/klaster/wpcontent/uploads/2023/12/Przewodnik-Klastry-energii-i-spoldzielnie-energetyczne.pdf

DOI: 10.24427/978-83-68673-38-8_2

Chapter 2. Comparison of Forecasted and Actual Energy Yields from PV Installations. Integration with Energy Storage Systems

Martyna KOŻUCHOWSKA, Marcin A. SULKOWSKI
Bialystok University of Technology, Faculty of Electrical Engineering,
[1]*e-mail: 83763@student.pb.edu.pl*
[2]*e-mail: m.sulkowski@pb.edu.pl*

Abstract. This chapter analyzes and compares the forecasted energy yields from a photovoltaic installation generated using several simulation programs with the actual energy production from the installation. It also discusses the advantages and disadvantages of energy storage systems and identifies scenarios where their use is beneficial. Simple payback periods are calculated for two PV installation variants to compare investment return times.

Streszczenie. W rozdziale przeanalizowane i porównane zostały prognozowane uzyski energii z instalacji fotowoltaicznej wygenerowane za pomocą kilku programów symulacyjnych, a następnie zostały one porównane z rzeczywistą produkcją energii przez instalacje. Omówiono także zalety i wady tego rozwiązania oraz to, kiedy i dla jakich instalacji warto zastosować magazyn energii. Wyznaczone zostały również proste okresy zwrotu dla dwóch wariantów instalacji PV w celu porównania czasu zwrotu inwestycji

Słowa kluczowe: magazynowanie energii, efektywność energetyczna, odnawialne źródła energii, fotowoltaika

Keywords: energy storage, energy efficiency, renewable energy sources, photovoltaic installations

Introduction

Due to the continuous rise in electricity prices, an increasing number of individuals are choosing to install photovoltaic systems in their homes or businesses. The primary goal is to achieve greater independence from the public power grid. When combined with an energy storage system, such installations allow users to utilize the energy generated by their own PV system at a later time, particularly when the system is not actively producing electricity. Currently, this is the most popular and widely accessible solution for acquiring electricity from renewable energy sources. This trend has been largely driven by ongoing technological advancements, which have led to reduced installation costs and improved system efficiency.

One of the key characteristics of PV installations is the variability of energy production depending on the time of day, season, and weather conditions. Such fluctuations can disrupt the operation of the power grid, leading to phenomena such as voltage increases or distortions in other parameters that define energy quality. Energy storage systems help stabilize grid parameters by enabling energy to be fed into the grid during periods of high demand or allowing users to purchase energy when prices are low and use it when prices are high.

A crucial factor influencing the decision to install a PV system is its profitability and payback period, which depend on the amount of energy the system can produce. During the design phase, a report is generated that presents the forecasted energy yield of a specific PV installation based on input data provided to the simulation software. This raises an important question: will the forecasted energy yield reflect the actual energy production of the PV system? Many prospective PV system owners wonder whether discrepancies between forecasted and actual production will occur, and if so, how significant they will be. Will these differences affect the payback period and overall profitability of the installation? Will it be possible to store some of the energy and use it during periods when the system is not producing?

Therefore, it is worthwhile to analyze the data obtained from PV system simulations and compare them with the actual energy production of a PV installation located and configured according to the simulation parameters.

Technical Data of the PV Installation and Panel Layout

The analyzed photovoltaic installation has a total capacity of P = 49.92 kW and is mounted on a flat roof covered with roofing felt. The system comprises:

- 104 monocrystalline photovoltaic modules, each rated at P = 480 Wp;
- A P = 50 kW **inverter**.

The panels are oriented **southward** and mounted on ballasted support structures with a tilt angle of 15°. The installation is located in Bialystok, Poland (geographical coordinates: 23°10'E, 53°08'N), and all simulation scenarios are based on this location.

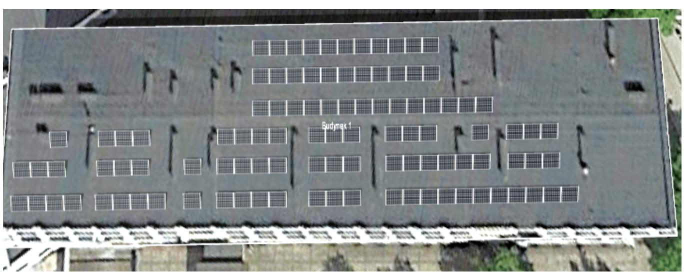

FIGURE 1. Top-down view of the building's roof with the photovoltaic panel layout generated using Sunny Design [5]

The actual layout of the photovoltaic panels on the roof was modeled using the Sunny Design software, which is dedicated to forecasting electrical energy production. The layout reflects the real-world configuration of the system.

Factors Affecting the Energy Output of a Photovoltaic Installation

The efficiency and energy yield of a photovoltaic system are influenced by a wide range of factors, which can be broadly categorized into **environmental** and **technical** parameters.

Initial Design Considerations

During the early design phase of a PV installation, the building's electricity consumption profile is analyzed, typically using a network analyzer, to determine its energy demand characteristics. This enables the designer to tailor the system's size and orientation so that the highest energy production coincides with peak consumption periods.

Environmental Factors

The most critical environmental factor is solar irradiance, which depends on:

- The geographic location of the PV system.
- The tilt angle of the panels relative to the sun's rays.
- The azimuth, i.e., the directional orientation of the panels.

If the system lacks energy storage and peak consumption occurs in the morning and afternoon, an east-west orientation may be optimal. Although this configuration slightly reduces the total annual energy yield compared to a south-facing setup, it better aligns the production curve with the building's consumption profile. Conversely, a south-facing system without storage maximizes annual output and is ideal when peak demand occurs around midday.

If the system includes energy storage, surplus energy can be stored and used during non-generating hours or when electricity prices are high. This increases self-consumption and improves economic performance.

Temperature Effects

Temperature is another key factor. PV module datasheets specify a temperature coefficient, typically ranging from −0.3%/°C to −0.4%/°C. While standard testing occurs at 25°C, real-world operating temperatures are often significantly higher. As temperature increases, module power output decreases proportionally. Thus, on hot sunny days, module efficiency may be lower than on cooler days with strong irradiance.

Shading and Surroundings

Beyond selecting an appropriate location and system parameters, special attention must be paid to the surrounding environment. A major issue is shading, caused by nearby trees, buildings, or chimneys. If even a fragment of one panel in a string is shaded, the performance of the entire series-connected group drops to the level of the weakest (i.e., shaded) cell. In practice, this leads to significant losses in total energy production from the PV system [1].

One method to mitigate such losses is the use of bypass diodes, which allow electrical current to flow around shaded cells. These diodes enable energy to bypass the affected panel, minimizing production losses.

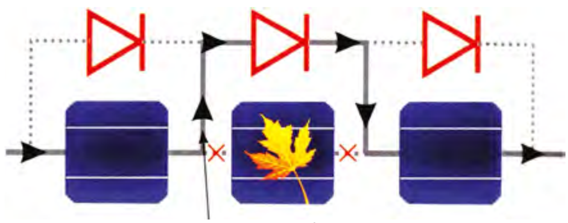

FIGURE 2. Example of bypass diode application, current flow through PV cells when one cell is shaded [2]

Technical Components

Another critical factor is the selection of system components. The market offers PV modules with varying power ratings, silicon structures, and efficiencies. Choosing modules with higher efficiency, defined as the ratio of electrical energy output to solar energy input, allows for greater energy yield from a given surface area.

The inverter to which the PV panels are connected also plays a significant role. Key considerations include:

- Number of MPPT inputs (Maximum Power Point Tracking): If the system has only one MPPT input, shading of a single module causes the entire system to operate at the reduced power level of the shaded module. In contrast, systems with multiple MPPT inputs allow unaffected panel groups to continue operating at full

capacity. This is especially beneficial in installations with panels oriented in different directions (e.g., east and west), where strings can be separated and connected to individual MPPT inputs to optimize performance.
- DC input voltage: Lower voltage thresholds enable the system to begin energy production at lower irradiance levels. This means that on days with weak sunlight, the system can start generating energy earlier, increasing the total daily yield.

In summary, careful selection of system components and installation parameters, tailored to the building's energy consumption profile and environmental conditions, is essential for maximizing the efficiency and profitability of a PV installation.

Analysis and Comparison of Simulation Results from Various Software Tools with Actual Energy Production from the PV Installation

To simulate the energy yields of a photovoltaic installation, dedicated software tools can be used. This enables a comparison between forecasted results and actual energy production. In this study, simulations were conducted using three programs: PV*SOL [7], PVGIS [6], and Sunny Design [5].

In Sunny Design [5] and PV*SOL [7], the building's location was selected, and the photovoltaic panels were arranged on the roof according to their actual physical layout. After entering the relevant system parameters, the software generated graphs and data on expected energy production. An example of a production forecast graph generated by PV*SOL is shown below:

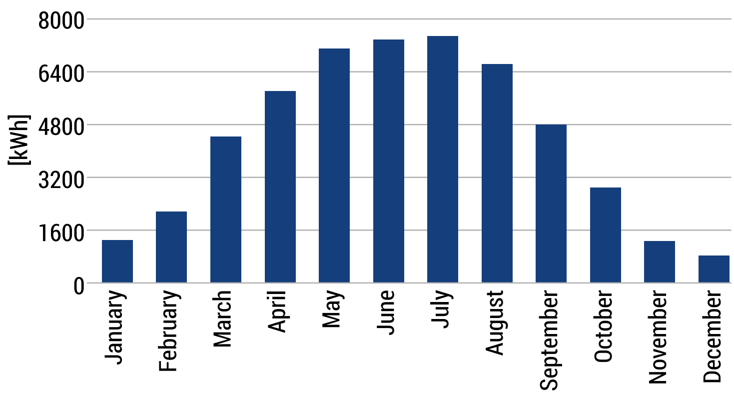

FIGURE 3. Sample forecasted energy production graph generated using PV*SOL [7]

Simulations in PVGIS [6] were based solely on the location and specified system parameters, including azimuth. No panel layout was performed on the building's roof. The production forecasts from PVGIS are illustrated below:

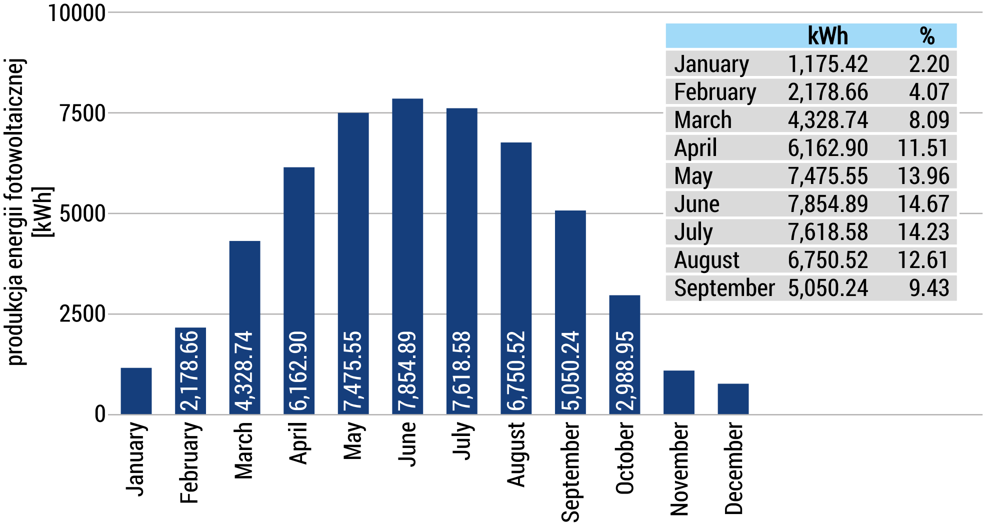

FIGURE 4. Sample forecasted energy production graph generated using PVGIS [6]

After completing all simulations, the following results were obtained:

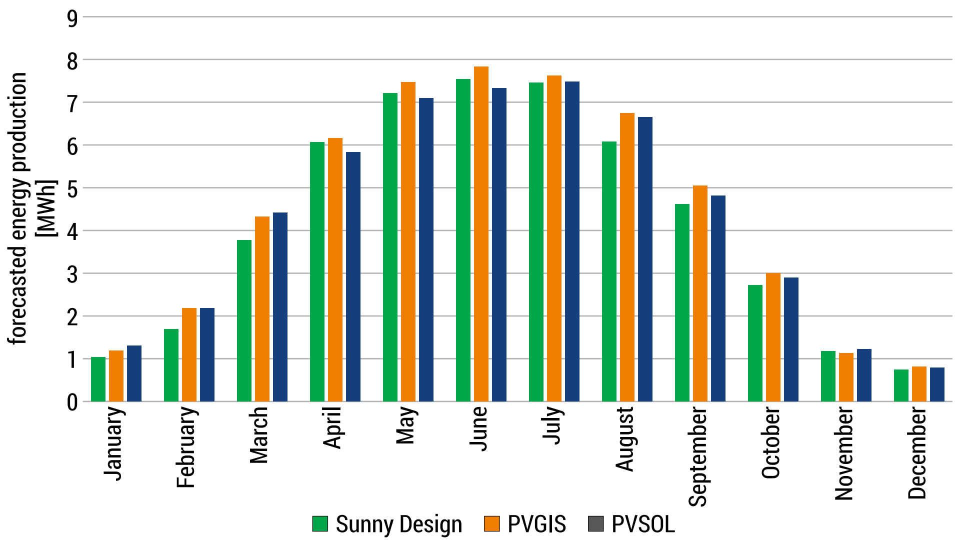

FIGURE 5. Graph presenting forecasted energy yields from the PV installation

TABLE 1. Forecasted energy yield values from selected simulation programs

Month	Sunny Design [MWh]	PVGIS [MWh]	PVSOL [MWh]
January	1.033	1.1754	1.3061
Febuary	1.682	2.1787	2.1786
March	3.766	4.3287	4.4225
April	6.063	6.1629	5.8404
May	7.2	7.4756	7.1017
June	7.53	7.8549	7.3405
Jul y	7.462	7.6186	7.4901
August	6.085	6.7505	6.6691
September	4.615	5.0502	4.832
October	2.706	2.989	2.8985
November	1.183	1.1304	1.2363
December	0.747	0.8221	0.8095
Σ	**50.072**	**53.537**	**52.1253**

Upon analyzing the forecasted energy yields, it can be observed that Sunny Design generally provides lower monthly values compared to the other two programs. These differences are likely due to each program using a different simulation model – some more advanced than others – and relying on weather data from various meteorological stations.

PVGIS consistently shows the highest forecasted energy yields across most months. These discrepancies may also stem from the fact that Sunny Design and PV*SOL included detailed panel layouts with physical components, whereas PVGIS did not incorporate such spatial modeling. The highest annual energy production is predicted by the simulation performed using PVGIS. The lowest annual energy production is simulated by Sunny Design.

It is important to note that simulation values are based on long-term historical data, and the forecasted energy yield is typically calculated as an average of these values. Given that each of the three simulations provides different energy yield estimates, a key question arises: Which forecast most closely reflects actual energy production?

To answer this, actual energy production data from a PV installation with the same location and parameters used in the simulations was analyzed.

The monthly energy production values for the years 2024 and 2025 were as follows:

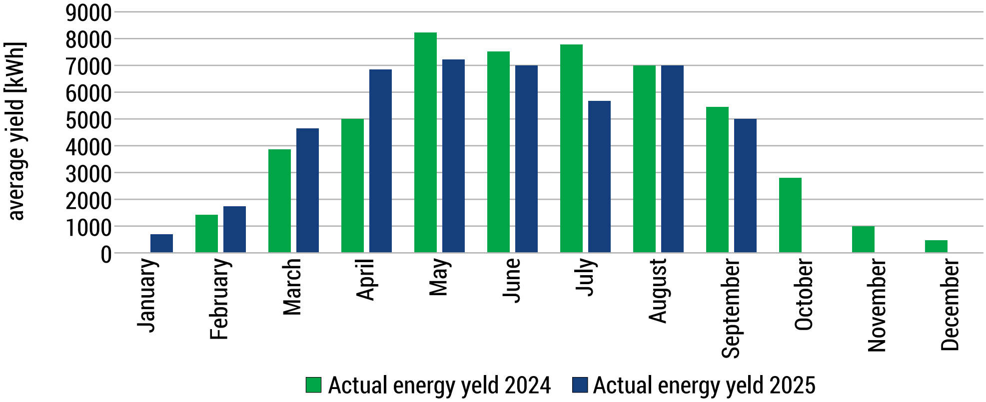

FIGURE 6. **Graph comparing actual energy production**

The graph shows that monthly energy production varies significantly between years. This is due to weather conditions – specifically, the number of sunny days per month – which fluctuate annually. To compare actual results with simulated ones, the average of the real production values was calculated.

The comparison between forecasted and actual average monthly energy production is presented below:

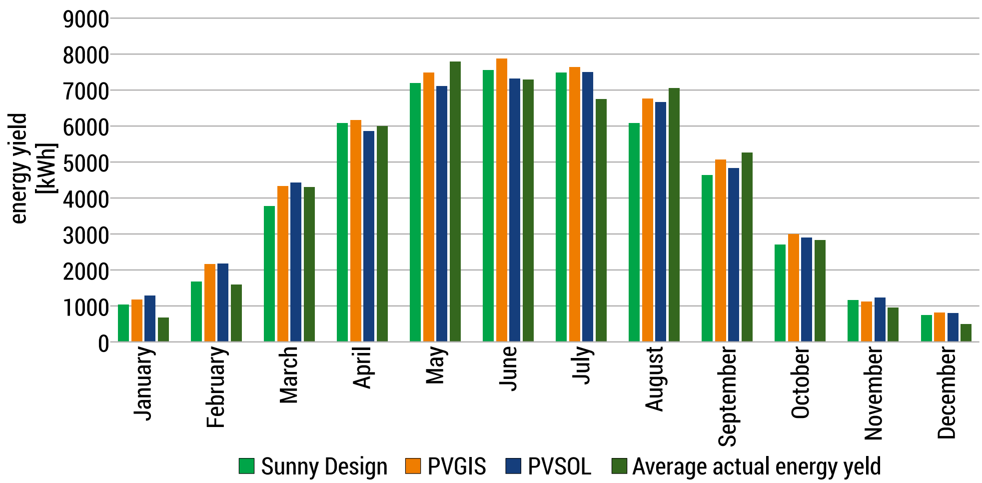

FIGURE 7. **Graph comparing simulated energy yields with average actual production**

Based on the comparative graph and Table 2, it is evident that forecasts for December, January, and February are significantly overestimated by all three programs. Sunny Design consistently shows the lowest forecasted values across most months compared to the other two simulations.

TABLE 2. Comparative table of forecasted energy yields and average actual energy production

Month	Sunny Design [kWh]	PVGIS [kWh]	PVSOL [kWh]	Average actual energy yield [kWh]
January	1033	1175.4	1306.1	684
Febuary	1682	2178.7	2178.6	1595
March	3766	4328.7	4422.5	4305
April	6063	6162.9	5840.4	5985
May	7200	7475.6	7101.7	7790
June	7530	7854.9	7340.5	7280
July	7462	7618.6	7490.1	6760
August	6085	6750.5	6669.1	7035
September	4615	5050.2	4832	5260
October	2706	2989	2898.5	2820
November	1183	1130.4	1236.3	969
December	747	822.1	809.5	494
Σ	**50072**	**53537**	**52125.3**	**50977**

The average annual actual energy production is approximately P = 51,000 kWh. This value is higher than the production forecast generated by Sunny Design, but lower than the production forecast from the other two programs. However, the data does not allow for a definitive conclusion as to which program provides the most accurate forecasts. Each tool offers values close to actual production in some months, while in others the forecasts are either overestimated or underestimated.

To further refine the analysis, the average forecasted energy yield from all three programs was calculated and compared to the average actual production:

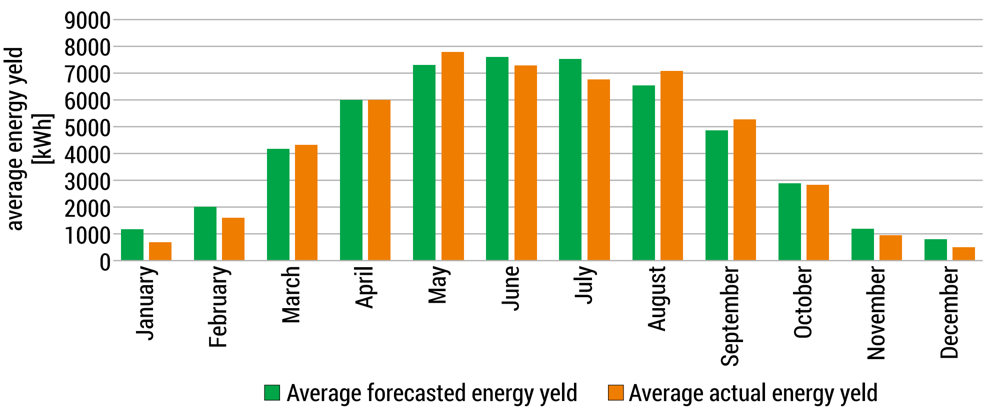

FIGURE 8. Graph comparing average forecasted energy production with average actual production

This graph shows that the average forecasted values are generally closer to actual production. In June and July, as well as from November to February, actual production is slightly lower than forecasted. In other months, actual values are equal to or even exceed the forecasts.

In conclusion, no simulation software provides a perfect model for predicting real-world energy production. Each program uses different weather datasets and simulation algorithms of varying complexity. The most reliable approach is to calculate the average forecast from multiple programs, which yields the most probable and realistic estimate of annual energy production from a PV installation.

Is It Worth Implementing an Energy Storage System?

As the name suggests, an energy storage system is designed to **accumulate surplus energy** produced by a photovoltaic (PV) installation during its operation, so that it can later be used to power devices connected to the electrical network when the PV system is not generating energy [3]. This solution is particularly beneficial for users seeking greater independence from the public power grid and aiming to reduce electricity purchase costs during periods of high market prices.

Advantages of Energy Storage [4]

Implementing an energy storage system offers several key benefits:

- Increased energy independence: Users can reduce the risk of power outages by using stored energy to supply critical devices.
- Higher self-consumption: Surplus energy can be used later, increasing the self-consumption rate from approximately 20% (without storage) to 70–80% (with storage).
- Reduced electricity costs: Higher self-consumption directly lowers the amount of energy purchased from the grid.
- Grid support: Sudden spikes in renewable energy generation can overload the grid and cause instability. Storage systems help by absorbing excess energy and releasing it gradually, improving grid stability.
- Smart energy management: Modern energy management systems can intelligently control charging and discharging cycles based on:
  - forecasted building energy demand,
  - predicted weather conditions,
  - market electricity prices.

Limitations and Considerations [4]

Despite their advantages, energy storage systems also have drawbacks:

- High upfront cost: Batteries and associated infrastructure are expensive.
- Limited lifespan: Storage systems degrade over time and require eventual replacement.
- Energy losses: Charging and discharging processes involve efficiency losses.

- Installation constraints: Finding a suitable location for optimal operation is essential.
- Economic viability: Under net-metering schemes, users can feed energy into the grid and retrieve 70–80% of it free of charge. In such cases, the cost of installing a storage system may outweigh the benefits, making the investment economically unjustified.

When Is Storage Worthwhile?

The decision to implement energy storage depends on several factors:

- Billing system: Under net-metering, storage may be unprofitable. Under net-billing, it can yield higher returns by allowing users to consume self-generated energy later rather than selling it at fluctuating market prices.
- Consumption profile: If the building's energy demand curve aligns closely with the PV production curve, storage may be unnecessary, unless used for backup power or arbitrage (buying energy at low prices and using it when prices are high).
- Surplus energy levels: If the system generates significant excess energy, storing it can lead to substantial savings and increased self-consumption [4].

Profitability and Payback Period of the Investment – Simple Payback Analysis

This section analyzes two variants of photovoltaic installations: one with an energy storage system and one without. Both installations are assumed to operate under a net-billing settlement scheme. For each variant, a simple payback period is calculated to compare the time required to recover the investment.

Variant I – PV Installation with Energy Storage

Assumptions:

- Average annual energy production: approximately P = 50.977 MWh.
- Total investment cost: approximately 240,000 PLN.
- Self-consumption rate: 70%, equivalent to P = 35,683.9 kWh.
- Electricity price: 1.80 PLN/kWh.
- Annu savings: 35,683.9 kWh * 1.80 PLN/kWh = 64,231.02 PLN.

Simple Payback Period (SPP) is calculated as:

$$SPP = \frac{\text{Investment Cost}}{\text{Annual Energy Savings}} = \frac{240\ 000\ \text{PLN}}{64\ 231{,}02\ \text{PLN/year}} = 3{,}7\ \text{year} \quad (1)$$

Thanks to the use of an energy storage system, which increased the self-consumption rate to 70%, the investment, despite the additional cost of the battery, achieves a relatively short payback period of less than 4 years.

Variant II – PV Installation without Energy Storage

Assumptions:

- Average annual energy production: approximately P = 50.977 MWh.
- Total investment cost: approximately 150,000 PLN.
- Self-consumption rate: 20%, equivalent to P = 10,195.4 kWh.
- Electricity price: 1.80 PLN/kWh.
- Annual savings: 10,195.4 kWh * 1.80 PLN/kWh = 18,351.72 PLN.

Simple Payback Period (SPP) is calculated as:

$$SPP = \frac{\text{Investment Cost}}{\text{Annual Energy Savings}} = \frac{150\,000 \text{ PLN}}{10\,195{,}4 \text{ PLN/year}} = 8{,}2 \text{ year} \qquad (1)$$

Without an energy storage system, despite lower initial costs, the payback period is more than twice as long, due to the significantly lower self-consumption rate. Additional revenue could be generated by selling surplus energy to the grid. However, under the net-billing scheme, this is difficult to estimate due to dynamic market prices. During periods of high PV generation, electricity prices may become very low or even negative, and grid voltage may rise to levels that prevent the system from feeding energy into the grid.

Summary

Based on the analysis of forecasted energy production from various simulation programs, it can be concluded that no single software tool provides a perfect prediction of actual monthly energy yields. This is primarily due to the fact that each program relies on different weather data sources and employs simulation algorithms of varying complexity.

Similarly, actual energy production varies from year to year, even for the same month, and cannot be precisely predicted. Production is influenced by numerous environmental factors, which have a significant impact on the final energy yield.

Energy storage systems, which are gaining popularity, are not universally cost-effective. Therefore, a thorough analysis is required to determine whether their implementation is economically justified in a given scenario.

In the profitability analysis conducted for the PV installation discussed in this study, whose forecasted yields were previously presented, it was shown that, despite the higher initial investment associated with purchasing an energy storage system, the payback period was twice as short compared to a system without storage.

The economic viability of a photovoltaic installation depends on many factors. Consequently, conducting a detailed analysis of forecasted energy production is highly beneficial. It demonstrates that relying solely on data from a single simulation program may lead to significant discrepancies when compared to actual performance.

References

[1] Frydrychowicz-Jastrzębska, G., Krawczyk, P. (2018). Produkcja energii elektrycznej przez system fotowoltaiczny dachowy. *Poznan University of Technology Academic Journals. Electrical Engineering*, *94*, 203–214. https://doi.org/10.21008/j.1897-0737.2018.94.0018

[2] Szymański, B. (2022). *Instalacje fotowoltaiczne* (edycja 2022).

[3] ecoABM. (n.d.). Retrieved October 21, 2025, from https://ecoabm.com/pl/baza-wiedzy/artykuly/wady-i-zalety-magazynow-energii-w-instalacjach-pv-czy-warto-inwestowac-w-baterie

[4] Głuchy, D. (2016). Czynniki warunkujące współpracę magazynów energii z OZE. *Poznan University of Technology Academic Journals. Electrical Engineering*, *87*, 191–204.

[5] Sunny Design. (n.d.). Retrieved October 20, 2025, from https://www.sunnydesignweb.com/sdweb/#

[6] Fotowoltaiczny System Informacji Geograficznej. (n.d.). pvgis.com. Retrieved October 20, 2025, from https://pvgis.com/pl

[7] PV*SOL premium (n.d.). Retrieved October 20, 2025, from https://pvsol.software

DOI: 10.24427/978-83-68673-38-8_3

Chapter 3. Analysis of the impact of an energy-efficient brick wall and its structure on wireless communication

Agnieszka CHOROSZUCHO

Bialystok University of Technology, Faculty of Electrical Engineering

ORCID: 0000-0001-7884-9264, e-mail: a.choroszucho@pb.edu.pl

Streszczenie. Cegła (zwłaszcza cegła pełna) ma wysoką pojemność cieplną, co oznacza, że nagrzewa się powoli i oddaje ciepło do otoczenia, co może przyczyniać się do wzrostu efektywności energetycznej budynku. Nowoczesne, porowate cegły lub ściany wielowarstwowe z dodatkową izolacją są bardziej energooszczędne. Ważne jest, aby zweryfikować, czy komunikacja bezprzewodowa w tego typu konstrukcjach spełnia oczekiwania użytkowników. Rozdział przedstawia analizę wpływu ściany z cegły perforowanej na propagację fal. Analiza objęła obszar zawierający ścianę z cegły perforowanej. Zbadano, jak rozmiar otworów wpływa na wartości natężenia pola za ścianą. Rozważono dwa warianty ściany różniące się rozmiarem otworów. Dodatkowo przeprowadzono analizę wielowariantową, uwzględniając zmienność przewodności dla każdego modelu ściany. Analizę przeprowadzono z wykorzystaniem metody różnicowej w dziedzinie czasu (FDTD). Wszystkie obliczenia przeprowadzono przy częstotliwości 5 GHz, która jest wykorzystywana np. w Wi-Fi. Zmiany wielkości pustych przestrzeni powodują zmianę procentowej zawartości masy ceramicznej w cegle. Różnice te nie są jednak tak znaczące w przypadku zmniejszania lub zwiększania długości pustych przestrzeni. Rozkład pola zależy przede wszystkim od złożonych zjawisk fizycznych zachodzących w cegłach (np. wielokrotnych odbić). Na podstawie przedstawionych danych można lepiej zrozumieć zjawiska fizyczne i precyzyjniej zaplanować rozmieszczenie nadajników.

Abstract. Brick (especially solid brick) has a thermal storage capacity, meaning it heats up slowly and releases heat to the surroundings, which can contribute to a building's energy efficiency. Modern, porous bricks or multi-layer walls with additional insulation are more energy-efficient. It's important to verify whether wireless communication in these types of structures meets user expectations. The chapter presents an analysis of the influence of a wall made of perforated bricks on wave propagation. The analysis involved an area containing a perforated brick wall. The analysis examined how the size of the holes affected the field intensity values behind the wall. Two wall variants differing in hole size were considered. Additionally, a multivariate analysis was carried out, taking into account the variation in conductivity for each wall model. The analysis was carried out using the Fine Difference Time Domain method (FDTD). All calculations were carried out at a frequency of 5 GHz that is used in e.g. Wi-Fi. Changes in the size of hollows result in a change in the percentage of ceramic mass in the brick. However, the differences are not so significant in the case of reducing or increasing the length of hollows. The field distribution depends primarily on complex physical phenomena occurring within the bricks (e.g., multiple reflections). Based on the data presented, we can better understand the physical phenomena and more precisely plan the transmitter placement.

Słowa kluczowe: efektywność energetyczna, systemy komunikacji bezprzewodowej, materiały budowlane, metoda różnic skończonych w dziedzinie czasu

Keywords: energy efficiency, wireless communication systems, building materials, Finite Difference Time Domain method (FDTD)

Introduction

Ceramic bricks insulate very well and have a high heat retention capacity. The heated material gradually releases heat to the surroundings and does not cool down dramatically. Advantages of bricks in terms of energy efficiency:

- Heat storage: brick stores heat, allowing one to maintain a more stable temperature in your home, reducing the need for heating in winter and cooling in summer.
- Thermal insulation properties: when combined with appropriate insulating materials, brick walls can significantly reduce heat loss.
- Acoustic insulation: bricks effectively muffle sounds, which increases the comfort of residents.
- Naturalness: brick is a natural material, which affects the healthy microclimate in the building and is environmentally friendly.

Energy demand depends primarily on the heating and ventilation method. Energy consumption differences between individual systems can be even severalfold. The lowest energy demand is observed for an electrically powered heat pump heating system – an average of 21.6 kWh/(m^2·year). Much higher demand is observed for gas heating (an average of 74.4 kWh/m^2·year) and biomass heating (an average of 107.2 kWh/m^2·year). The impact of walls on energy demand is much smaller, although not negligible.

Differences in energy demand between wall variants can be as high as 15%. Single-layer walls are just as good a solution as insulated walls. The lowest energy demand was observed for single-layer walls made of 36.5 cm thick YTONG ENERGO blocks. It's worth noting that walls made of 36.5 cm thick YTONG ENERGO PP2/0.35 blocks have a U-value of 0.25 W/m^{2}K, while walls made of 25 cm thick ceramic blocks with a 12 cm layer of polystyrene have a U-value of 0.24 W/m^{2}K. Despite the slight difference in favor of the double-layer wall, the building made of YTONG ENERGO blocks demonstrated a better energy demand indicator.

An undeniable advantage of single-layer partitions is their precise installation technology, which eliminates linear thermal bridges at joints, positively influencing internal gains. Depending on the construction team, these gains can actually be even higher compared to the relatively imprecise masonry techniques using standard mortar. Furthermore, the practice of installing insulation systems sometimes involves the use of certain simplifications that negatively influence the thermal insulation of the partition. Examples include only partial insulation of thermal bridges or reducing insulation thickness by smoothing the surface of the external partitions.

While ensuring energy efficiency, it is also important to consider the functionality of such a home. Nowadays, more and more devices operate wirelessly. This is due, among other things, to the trend toward SMART homes, and the elimination of wiring, which often makes it difficult to conceal while maintaining a room's aesthetic. Thanks to the use of standard devices, the installation of wireless data transmission systems is in many cases easier and faster than the installation of cable networks. Technologies of this type constitute an important supplement to wired networks. They can be used where technical considerations make it difficult to lay wired networks. Wireless data transmission networks allow for uncomplicated and fast connection of many devices, while maintaining the probability of dynamic configuration of the set of communicating components [1–3].

The effects occurring during the propagation of electromagnetic waves inside buildings do not always allow for maintaining good communication. The biggest problem is the geometry and material from which the construction elements are made. Checking the quality of the network involves conducting many tests in real conditions, which is expensive and laborious. Numerical analysis allows for quick and accurate performance of a multi-variant analysis of the quality of the wireless connection. The use of numerical modeling algorithms enables the determination of electromagnetic field distributions in small and large-scale systems. Despite the inevitable approximations in the constructed models, the use of numerical analysis allows obtaining solutions to complex constructions. The propagation of electromagnetic waves in discussed constructions belongs to a group of issues in which numerical algorithms can be an important, useful tool for assessing field phenomena and provide assistance in designing a wireless network.

Due to the complex nature of the occurring physical phenomena and the significant diversity of geometry and material structures in building structures, the results presented in the available literature are often fragmentary. In selected cases, they concern systems that are largely theoretical in terms of geometry and materials used. This is partly due to the choice of method for calculating field phenomena.

Correct determination of electrical properties of materials is an essential condition for accurate representation of field phenomena in modeled construction. The evaluation of wave propagation in the high frequency range involves the need to analyse the influence of the structure itself and building materials with different values, especially in terms of electric permittivity ($\varepsilon = \varepsilon_0 \varepsilon_r$) and conductivity ($\sigma$) [4]. Basic building materials are normally imperfect dielectrics. For this cause, the chapter additionally presents a summary of the values used for electrical parameters of building materials.

A review of publications and a discussion on the influence of various factors on the electrical parameters of brick, concrete, glass and wood are presented in [5]. According to the chapter, the authors observed that it is practically impossible to know the exact values of the parameters for all environments. They state that measurements should be made for specific variants of models, taking into account the frequency or conditions of the surrounding environment, which affect the composition of the material. Many publications do not take into account the above factors and, for example, concrete is treated as a material for which the authors do not take into account the diversity of components, which depend on the expected mechanical properties of concrete, the type of construction or the construction technology used.

The review of the source materials shows that the issues discussed in this work constitute an important, still unexplored issue. The aim of this study is to design and assess the operating conditions of wireless communication systems. Most studies focus on the analysis of the impact of the arrangement of walls and other construction elements on the propagation of electromagnetic waves [6]. The following issues are considered to a lesser extent: complex structure of wall materials and the variety of building materials used (i.e. types of bricks).

In the literature, walls made of basic building materials are analyzed, which are often treated as uniform homogeneous structures. Despite the diverse composition and properties of individual components, the particle sizes, e.g. aggregate; meet the conditions of quasi-stationarity. The dimensions of the model remain relatively large compared to the unordered components, e.g. concrete [7]. The second reason for the homogenization of the properties of a given material is related to the limited possibilities of mapping a complex structure due to the capabilities of the computer or software.

In this chapter, the author wanted to demonstrate the change in conductivity in various wall models.Different building materials (e.g. concrete, solid and hollow bricks, aerated concrete) have a significant effect on the electric field values. The main reason for the analysis was the use by other authors [8, 9] of different electrical parameters of bricks, concrete or aerated concrete. For example, the variety of conductivity of the brick is very wide 0.0174–0.12 S/m. The same applies to other electrical parameters describing building materials.

This chapter presents an analysis of the effect of varying the width of the brick holes on electromagnetic wave propagation and the electric field intensity. The multivariate calculations also took into account the variation in the brick conductivity, which depends on humidity, environmental conditions, and the local climate. Commonly used bricks containing 18 holes each were considered. The analysis utilized the FDTD differential method, which allowed for the observation of instantaneous field distributions and phenomena occurring within the bricks. Numerous assumptions were made when developing the numerical model.

Building materials

In the literature, walls made of basic building materials are often treated as uniform homogeneous structures. Despite the diverse composition and properties of individual components, the particle sizes, e.g. aggregate; meet the conditions of quasi-stationarity. The dimensions of the model remain relatively large compared to the unordered components, including concrete [10]. The second reason for the homogenization of the properties of a given material is related to the limited possibilities of mapping a complex structure due to the capabilities of the computer or software.

For the reasons given, the analyzed walls are described as homogeneous plates of various sizes, whose properties are uniform, isotropic and expressed by three parameters: relative electric permittivity, relative magnetic permittivity and conductivity. Building structures are created based on basic building materials whose complex and variable internal structure affectsmaterial parameters, impacting building and electrical properties. The discussion of these types of materials allows for taking into account the building technologies used in a given country.

Lime-sand (silicate) products and aerated concrete are produced from almost identical raw materials, but different production technologies mean that the resulting materials have different properties. In both cases, the basic ingredients are lime, sand and water. Silicate materials, like building ceramics, are characterized by high volumetric density resulting from the small amount of free space in the material.

Bricks are a type of building material typically made of sand, lime, or clay. They are generally used to construct walls, pavements, and other types of architecture. The geometry of bricks is very diverse and based on the proportion of height (*h*) to width (*b*) and length (*l*) of 1:2:4 (Fig. 1).

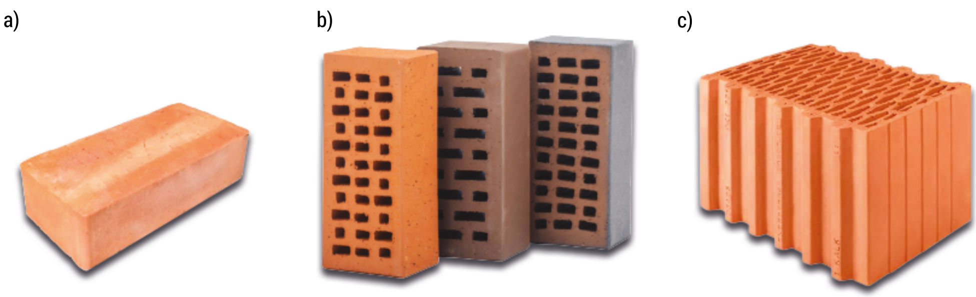

FIGURE 1. Examples of masonry elements: (a) full brick; (b) hollow brick; (c) hollow block

The authors of the publication [11] measured the electrical parameters for three types of solid bricks (red, brown and grooved), with water content close to zero. The analysis concluded that:

- at frequencies {3, 9, 24} GHz the value of ε_r' is similar and is within the limits of 3.7–4;

- regardless of the brick type, displacement current losses are comparable at two frequencies (3 GHz and 9 GHz);
- whereas for f = 24 GHz the value of ε_r' is convergent to the ε_r' obtained at f = 3 GHz and 9 GHz, and the value of ε_r" is five times higher in comparison with the two analyzed frequencies, i.e. for 3 GHz and 9 GHz ε_r" is 0.12 and for 24 GHz ε_r" = 0.6.

Depending on the frequency, the available literature reports relative permittivity values in the range of 2.82–19, while conductivity values range from 0.00278 to 0.2 S/m.

In an era of growing environmental awareness and rising energy prices, building energy efficiency is becoming a key issue not only among investors and architects but also among everyday property users. One of the most important aspects that affect energy savings is adequate thermal insulation. Brick buildings have traditionally dominated in Poland, and their thermal insulation properties raise many questions and concerns. The right techniques and materials can help us strive for warmer, more economical, and environmentally friendly interiors

In the context of brick construction, thermal insulation plays a particularly crucial role. Brick, although extremely durable and aesthetically pleasing, lacks high insulating efficiency. Therefore, to eliminate this drawback, it is worth using modern insulating materials that are adapted to the specific characteristics of brick buildings.

Numerical analysis method

The choice of the calculation method is largely dictated by the relative size of the model and the resulting approximations in the representation of physical phenomena. The choice of a computational algorithm requires consideration of the needs and constraints related to the specificity of the analysis of field phenomena in wireless transmission systems. The fundamental factors determining the use of numerical simulation methods remain interdependent and are largely opposed in nature. A classic example is the contradiction between increasing the size of the model while maintaining the expected precision of the material structure mapping and the accuracy of modeling real systems. The contradictions of the indicated factors are emphasized when striving to analyze larger and larger systems. The factor related to the numerical cost of calculations also becomes important.

The considered issues of electromagnetic wave propagation belong to the group of open problems. Despite the relatively small range of operation of local wireless communication systems (e.g. within buildings), the mapping of field phenomena is associated with the reproduction of wave propagation phenomena in an open, theoretically infinite area. In local wireless communication systems, the boundaries of wave propagation are not limited to the building area; hence, the complexity and size of the considered area must be taken into account, as well as the adoption of such boundary conditions that will accurately reflect the modeled system.

The geometry of the modeled building structures is at least comparable to or greater than the length of electromagnetic waves in the analyzed microwave frequency band. Due to the failure to meet the quasi-stationarity condition, the considered task comes down to solving the boundary-initial problem described by differential equations [12]. The component materials occurring in the studied systems are treated as continuous media, characterized by means of homogenized electrical parameters *ε*r, *m*r *s*.

The FDTD method was used to determine the electromagnetic field distribution in the analysed model [4, 6]. It is useful for calculating time-varying electromagnetic fields for high frequency and broadband signals. Maxwell's curl equations in time and space are the basis of the FDTD method [12]:

$$\nabla \cdot \mathbf{E} = -\frac{\partial \mathbf{B}}{\partial t} \tag{1}$$

$$\nabla \cdot \mathbf{H} = \mathbf{J}_p + \mathbf{J}_D + \mathbf{J}_I \tag{2}$$

$$\nabla \cdot \mathbf{D} = \rho \tag{3}$$

$$\nabla \cdot \mathbf{B} = 0 \tag{4}$$

$$\nabla \cdot \mathbf{J} = -\frac{\partial \rho}{\partial t} \tag{5}$$

where: **E** means the electric field (vector), **H** is the magnetic field (vector). Electric charges and electric currents are the sources of these fields, which are indicating as local densities, namely the charge density ρ and the current density **J**, $\mathbf{J}_P$. – the density of displacement current is and the density of conduction current ($\mathbf{J}_D$), while $\mathbf{J}_I$ denotes the current density vector that forces the field.

The description of the problems using equations (1)–(5) permits us to determine the field distribution in the unsteady state, as well as in the steady state. After applying the decomposition, equations (1)–(2) are introduced as 6 coupled first-order differential equations that describe the components of the electric and magnetic fields [12]:

$$\frac{\partial E_x}{\partial t} = \frac{1}{\varepsilon}\left(\frac{\partial H_z}{\partial y} - \frac{\partial H_y}{\partial z} - \sigma E_x\right) \tag{6}$$

$$\frac{\partial E_y}{\partial t} = \frac{1}{\varepsilon}\left(\frac{\partial H_x}{\partial z} - \frac{\partial H_z}{\partial x} - \sigma E_y\right) \tag{7}$$

$$\frac{\partial E_z}{\partial t} = \frac{1}{\varepsilon}\left(\frac{\partial H_y}{\partial x} - \frac{\partial H_x}{\partial y} - \sigma E_z\right) \tag{8}$$

$$\frac{\partial H_x}{\partial t} = \frac{1}{\mu}\left(\frac{\partial E_y}{\partial z} - \frac{\partial E_z}{\partial y}\right) \tag{9}$$

$$\frac{\partial H_y}{\partial t} = \frac{1}{\mu}\left(\frac{\partial E_z}{\partial x} - \frac{\partial E_x}{\partial z}\right) \tag{10}$$

$$\frac{\partial H_z}{\partial t} = \frac{1}{\mu}\left(\frac{\partial E_x}{\partial y} - \frac{\partial E_y}{\partial x}\right) \tag{11}$$

The field changes in the model area are determined assuming appropriately defined locations of the E and H vector components. In the time-domain differential method formulation, a shifted mesh design is considered for the electric and magnetic field components. The grid shape reflects the physical interpretation of EM phenomena.

Yee cell contains six suitably arranged field intensity component vectors: electric and magnetic. All analysed models aredivided of into an appropriate number of cells. Appropriately, distributing the components of vectors describing the intensity of the electric field **E** and magnetic field **H** within each cell realize the FDTD scheme in this area. The determined distributions of physical quantities are assigned at certain points of the area (*x*, *y*, *z*). Discrete, finite integration step size of the field is presented by Δ_x, Δ_y, Δ_z.

The components of the electromagnetic field are calculated at different points in space. Iterative integration of Maxwell's equations is based on the use of a two-step scheme. In choosen step n, the electric field distribution is determined, while the values of the components of the magnetic field intensity vector are calculated from the displacement at the moment Δ_t. Applying Euler's scheme of central differences to the approximation of partial derivatives in the area and after time, the equations (6)–(11) take the structure, e.g.:

$$\frac{{}^{n+1}_{i,j,k}E_z - {}^{n}_{i,j,k}E_z}{\Delta_t} = \frac{1}{\varepsilon_{i,j,k}}\left(\frac{{}^{n+\frac{1}{2}}_{i+\frac{1}{2},j,k}H_y - {}^{n+\frac{1}{2}}_{i-\frac{1}{2},j,k}H_y}{\Delta_x} - \frac{{}^{n+\frac{1}{2}}_{i,j+\frac{1}{2},k}H_x - {}^{n+\frac{1}{2}}_{i,j-\frac{1}{2},k}H_x}{\Delta_y} - \sigma_{i,j,k}\,{}^{n+\frac{1}{2}}_{i,j,k}E_z\right) \tag{12}$$

The geometry of the analyzed models

The adopted classification of materials results from the relationship between the sizes of the components of the materials in relation to the length of the propagating electromagnetic wave. The work carried out was aimed at assessing the phenomena occurring inside the structure. The influence of electrical parameters of the material and the construction on the field distribution at frequencies used in WiFi wireless networks defined by standards created for the construction of wireless networks based on communication in the 5 GHz bands, was presented.

The focus of the analysis was an area consisting of a wall (0.12 m) made of a selected building material. On both sides of the wall, there was air. The geometry of the wall in the direction perpendicular to the direction of wave propagation were much larger than the wavelength in air (λ_p = 0.125 m). It was possible to reduce the length of the model by applying the appropriate boundary conditions (perfectly match layer, PML), in particular periodic boundary conditions (PBC) [12].

The adopted assumptions allow, in accordance with the goal, to determine the impact of the materials considered on the field intensity values, in an isolated system, omitting other factors. Additionally, an analysis of the impact of the variation of the length of the hollows in the brick was carried out. The model of the brick and parameters which were changed were shown in Fig. 2.

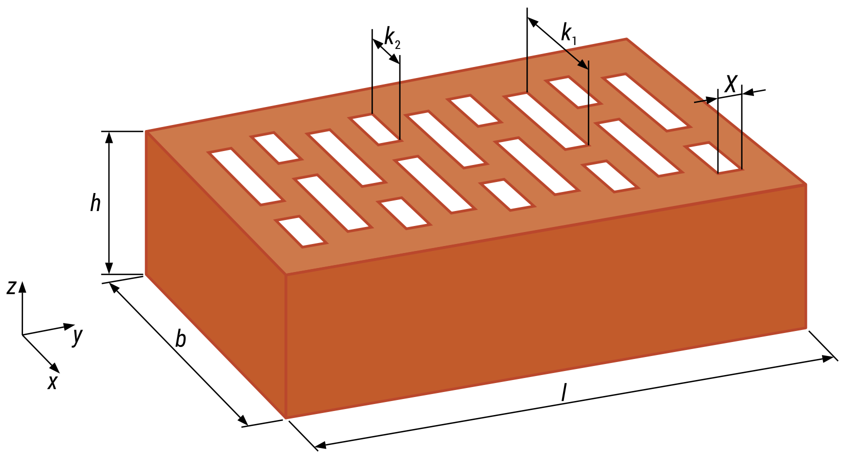

FIGURE 2. **Analyzed perforated brick**

The model length assumed in the calculations ensured the observation of the field intensity distribution in front of the wall and behind the wall in the area with the longitudinal dimension (in line with the propagation vector of the plane wave). The analysis of the electric field distributions and the quantitative assessment in the individual variants were carried out based on the observation of the electric field component max(E_z) in the area behind the wall. The assumed analysis area allowed for the consideration of possible deformations in the field distribution, related to the non-uniform structure of the materials considered and changes in the field at a certain distance from the wall. The field forcing in the system was a harmonic plane wave polarized linearly, propagating in the direction consistent with the Oy axis.

The wall was treated as a non-homogeneous material in terms of its internal structure and assumed material properties. The height (h), width (b) and length (l) of all analyzed bricks were 0.065×0.12×0.25 m, respectively (Fig. 2). Due to the homogeneity of the material structure, the width of the entire model area measured along the Ox axis could take any values. The area of the models considered was subject to discretization by entering a uniform grid of Yee cells ($\Delta_x = \Delta_y = 0.05$ mm).

Due to the fact that various values of electrical parameters of building materials are found in the literature, the analysis also takes into account the variability of the conductivity value $\sigma = 0 \div 0.2$ S/m [25]. The average length of air holes in a brick is 0.011 m (x), with different widths (k_1 and k_2) along the width of the brick ($b = 0.12$ m). After all the processes (drying and hardening), some parts of the brick may have an unusual size. For this reason, the influence of a different relative volume of the clay mass ($V_{\%}$) on the electric field values was analyzed. This factor was modified by changing the size of the ventilation holes (Table 1). The *vp* model is a reference model with actual dimensions of the holes. The percentage of the total brick volume inside the brick with different size of the holes was marked by $V_{\%}$.

TABLE 1. Relative volume of the clay mass in the perforated brick

Model	Figure of brick	(k_1) [m]	(k_2) [m]	$V_{\%}$
v1 (from *vp* less 0.012 m)		0.031	0.009	86.80%
vp		0.043	0.021	78.88%

Results of the analysis of the influence of wall material on the field intensity values

Fig. 3 presents characteristics depending on the conductivity and type of building material (solid brick and perforated brick). These are field values obtained after a plane wave passed through the wall at a distance of 2 m from the wall. It can be seen that although the hollow brick contains air holes, the field values are higher for solid brick, but at low conductivity values, i.e., up to 0.04 S/m. At higher conductivities, the field values are higher for perforated bricks. Additionally, Fig. 3 shows a comparison of the values obtained numerically and analytically for solid brick.

This section presents an analysis of the influence of the variation of the width of the hollows (k_1, k_2) in bricks on the values of the electric field intensity. The analysis also takes into account the changes of the conductivity 0–0.2 S/m.

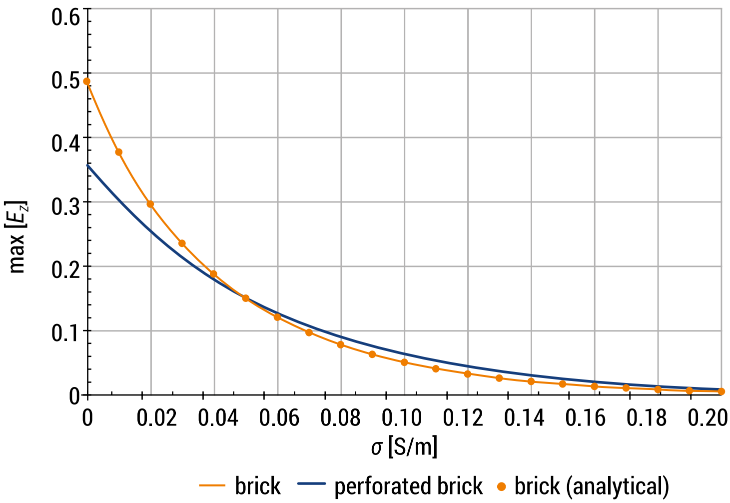

FIGURE 3. Maximum values of the E_z component behind a wall made of typical bricks

The analyzed differences in field values can be explained in macroscopic terms, by taking into account the share of ceramic mass in the volume of the brick. A higher value of $V_{\%}$ causes less wave front distortion in the area behind the wall. This results from the greater resultant homogeneity of the material. However, due to attenuation, this negatively affects the maximum field values. Fig. 4 presents a comparison of field intensity values for the analyzed wall variants for different conductivity values.

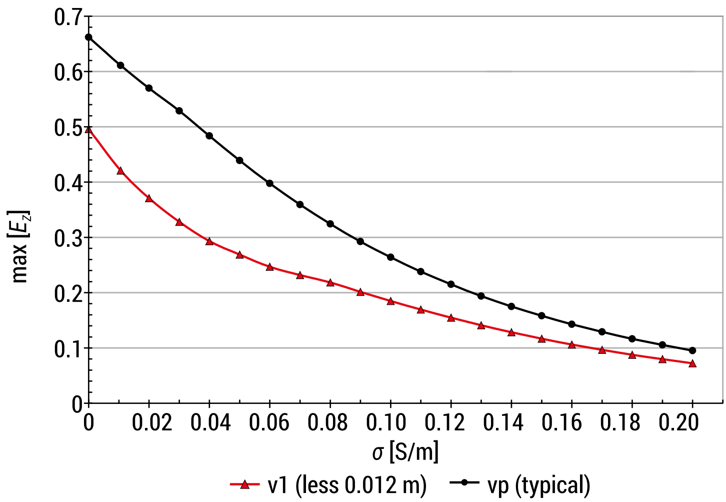

FIGURE 4. Maximum values of the E_z component behind a wall made of perforated bricks

When analyzing the model containing the smallest holes (*v1*) it was found that an almost 8% difference in *V*% compared to the reference model (*vp*) results in a large decrease in the field value by up to 35%. This result is caused by a porous material made of air holes. When passing through different areas of bricks, local changes in the wave velocity cause the appearance of momentary field images, which can increase the E_z values.

Table 2 presents numerically calculated values of the observed electric field component E_z for models with a wall made with different lengths of hollows. With the same values of electrical parameters of bricks (ε_r' = 4.44 and σ = 0.01 S/m), which were also selected for the analysis of the variant with a non-uniform wall, the results are for σ = 0.01 S/m. As can be seen, the greatest discrepancies in the results are precisely for small values of conductivity.

Table 2. Max(E_z) component behind a wall made of different length of perforated bricks

Model	Brick	$V_{\%}$	max(E_z) [–]
v1 (less 0.012 m)		86.80%	0.42
vp		78.88%	0.61

Assuming the same conductivity value (0.01 S/m), it was observed that the lowest electric field values were obtained for the model with the smallest holes (*v1*).

Conclusions

Bricks are one of the most popular building materials, significantly affecting a building's insulating properties. Choosing the right type of brick is crucial for the energy efficiency of buildings. Different types of bricks differ not only in appearance but also, above all, in their thermal properties. Here are some of the basic types:

- Solid brick – characterized by high density and strength, but its insulating properties may be limited.
- Perforated brick – known for its lightness and porosity, it improves thermal insulation by allowing more air to enter the building. Ideal for building exterior walls.
- Ceramic brick – has the best insulating properties, retains heat perfectly and regulates humidity inside the building.

- Silicate brick – although less effective in terms of insulation, it is characterized by high fire resistance and very good acoustics.

As one can see, the brick has many advantages and for this reason, it is also necessary to examine the quality of wireless communication. The chapter presents the FDTD method, which has proven to be indispensable in the analysis of non-homogeneous building materials, where analytical methods fail. The presented analysis results were aimed at determining the impact of the building material and the electrical parameters describing it on the field intensity values.

The results show that in the case of hollow bricks, the phenomena that occur inside the brick are very random and unpredictable. Based on the numerical analysis carried out and the results obtained, it can be stated that the phenomena occurring during wave propagation have an unpredictable nature, which, especially at low conductivity values, strengthens or weakens the field values.

References

[1] Glikstein, O., Pinhasi, G. A., Pinhasi, Y. (2024). Scaled Model for Studying the Propagation of Radio Waves Diffracted from Tunnels. *Electronics*, *13*, 1983. https://doi.org/10.3390/electronics13101983

[2] Edirisinghe, S., Galagedarage, O., Dias, I., Ranaweera, C. (2023). Recent Development of Emerging Indoor Wireless Networks towards 6G. *Network*, *3*, 269–297. https://doi.org/10.3390/network3020014

[3] Rufo, S., Aguiar-Castillo, L., Rufo, J., Perez-Jimenez, R. (2024). Neural Network-Based Detection of OCC Signals in Lighting-Constrained Environments: A Museum Use Case. *Electronics*, *13*, 1828. https://doi.org/10.3390/electronics13101828

[4] Aminian, A., Rahmat-Samii, Y. (2006). Spectral FDTD: a novel technique for the analysis of oblique incident plane wave on periodic structures. *IEEE T Transactions on Antennas and Propagation*, *54*(6), 1818–1825. https://doi.org/10.1109/TAP.2006.875484

[5] Stavrou, S., Saunders, S. R. (2003). Review of constitutive parameters of building materials. *Twelfth International Conference on Antennas and Propagation (ICAP 2003)*, *1*, 211–215. https://doi.org/10.1049/cp:20030052

[6] Ghodgaonkar, D., Varadan, V. V., Varadan, V. K. (1990). Free Space Measurements of Complex Permittivity and Complex Permeability of Magnetic Materials at Microwave Frequencies. *IEEE Transactions on Instrumentation and Measurement*, *19*(2), 387–394. https://doi.org/10.1109/19.52520

[7] Zhao, Z. B., Cui, X., Li, L., Gao, C. (2008). Analysis of shielding performance of reinforced concrete structures using the method of moments. *IEEE Transactions on Magnetics*, *44*(6), 1474–1477. https://doi.org/10.1109/CEEM.2015.7368676

[8] Peña, D., Feick, R., Hristov, H. D., Grote, W. (2003). Measurement and modeling of propagation losses in brick and concrete walls for the 900-MHz band. *IEEE Transactions on Antennas and Propagation*, *51*(1), 31–39. https://doi.org/10.1109/TAP.2003.808539

[9] Tan, S. Y., Tan, M. Y., Tan, H. S. (2000). Multipath delay measurements and modeling for interfloor wireless communications. *IEEE Transactions on Vehicular Technology*, *49*(4), 1334–1341. https://doi.org/10.1109/25.875253

[10] Iskander, M. F., Yun, Z., Zhang, Z. (2001). Outdoor/indoor propagation modeling for wireless communications systems. In *Antennas and Propagation Society International Symposium, USNC/URSI* (Vol. 2). Held in conjunction with: USNC/URSI National Radio Science Meeting (Cat. No. 01CH37229), 8 July 2001–13 July 2001, Boston, MA, USA. 150–153. https://doi.org/10.1109/APS.2001.959643

[11] Shah, M. A., Hasted, J. B., Moore, L. (1965). Microwave absorption by water in building materials: Aerated concrete. *British Journal of Applied Physics*, *16*(11), 1747–1754. https://doi.org/10.1088/0508-3443/16/11/319

[12] Taflove, A., Hagness, S. C. (2005). *Computational Electrodynamics: The finite – difference time – domain method*. Artech House.

DOI: 10.24427/978-83-68673-38-8_4

Chapter 4.
Smart IoT Air Quality Monitoring System

Alan KONDRUSIK[1]*, Agnieszka CHOROSZUCHO*[2]

Bialystok University of Technology, Faculty of Electrical Engineering

[1]*e-mail: alan.kondrusik@sd.pb.edu.pl,* [2]*e-mail: a.choroszucho@pb.edu.pl*

Streszczenie. Rozdział przedstawia projekt inteligentnego czujnika jakości powietrza opartego na mikrokontrolerze ESP32 i przystępnych cenowo czujnikach środowiskowych do zastosowań wewnętrznych. Opracowano prototyp urządzenia zdolnego do pomiaru temperatury, wilgotności, ciśnienia, stężenia LZO oraz poziomu pyłów zawieszonych. Dane były analizowane i wizualizowane za pomocą platformy ThingSpeak, a system sterowany był z poziomu smartfona. Testy przeprowadzono w warunkach statycznych i dynamicznych, symulujących zmienne środowisko. Wyniki potwierdziły skuteczność, stabilność i wiarygodność działania urządzenia, wskazując jego potencjał w praktycznym monitorowaniu jakości powietrza.

Abstract. The chapter presents a smart air quality monitoring system based on the ESP32 microcontroller and cost-effective environmental sensors designed for indoor applications. A prototype device was developed to measure temperature, humidity, pressure, VOC concentration, and particulate matter levels. The collected data were analyzed and visualized using the ThingSpeak platform, with system control implemented via a smartphone. Tests were conducted under both static and dynamic conditions simulating variable environmental factors. The results confirmed the effectiveness, stability, and reliability of the device, demonstrating its potential for practical air quality monitoring applications.

Słowa kluczowe: jakość powietrza, automatyka budynkowa, czujniki, ESP32, mikrokontrolery

Keywords: air quality, building automation, sensors, ESP32, microcontrollers

Introduction

In today's world, dynamic technological development creates both new challenges and opportunities in many industrial sectors. There is a trend toward miniaturizing devices, digitizing processes, increasing energy efficiency, reducing costs, and improving the quality of life. One of the key directions of this development is artificial intelligence, which finds applications in process automation, healthcare, and environmental monitoring. With increasing industrialization and technological advancement, the problem of air pollution is growing and poses a serious threat to human health and ecosystems. Particulate matter, smog, and exhaust emissions in urban environments contribute to climate change, environmental degradation, and respiratory ailments. In highly developed countries, pollution levels are particularly high, generating the need to implement advanced technologies for precise air quality monitoring [1]. Modern systems, such as intelligent environmental stations equipped with multi-parameter sensors, enable accurate, fast, and energy-efficient real-time measurements [2]. Integration with computer systems and artificial intelligence enables automatic data processing and analysis without user intervention. Such solutions are a key element of efforts to control and reduce harmful emissions, supporting the protection of public health and the environment.

In the face of growing demands for ecology and energy efficiency, the development of modern, energy-efficient, and easy-to-use measurement systems is essential. Analysis of available technologies, scientific literature, and standards such as WHO guidelines enables the design of devices that combine high measurement accuracy with functionality and reliability. In the context of building automation, such stations can play an important role in monitoring environmental parameters – such as air quality, temperature, and humidity – and in optimizing the operation of HVAC systems, contributing to improved occupant comfort and reduced energy consumption [3].

This chapter presents a proprietary concept for a smart air quality measurement station and an analysis of its operation, demonstrating the practical application of the ESP32 platform and cost-effective environmental sensors for monitoring environmental parameters.

ESP32 – open source hardware/software

Electronic devices, depending on their function, typically incorporate at least one control circuit responsible for controlling and coordinating the processes occurring within the system. However, not all designs require such a component – simpler solutions utilize only analog circuits, such as audio amplifiers or filters, or purely mechanical devices, such as clocks or switches. Modern electronic systems, particularly those designed for communication with the user, measuring environmental parameters, or implementing complex algorithms, utilize microcontrollers or microprocessors. These include smartphones, household appliances, building automation systems, and industrial controllers. In the presented project, the key element of the entire system is the microcontroller, responsible for its proper operation.

The selection of the control unit was based on an analysis of several key criteria. The most important was the presence of an integrated Wi-Fi module, enabling remote communication with the device via a local network or the Internet. This solution allows for easy transmission of measurement data to external servers for further analysis. After comparing available microcontrollers, we decided to use a chip from the ESP32 family from Espressif [4]. This choice was justified by its high computational performance, extensive programming support, low price, and built-in wireless connectivity. The ESP32-WROOM-32U module (Fig. 1) also features an IPEX connector for connecting an external antenna, significantly improving the stability and range of Wi-Fi communication.

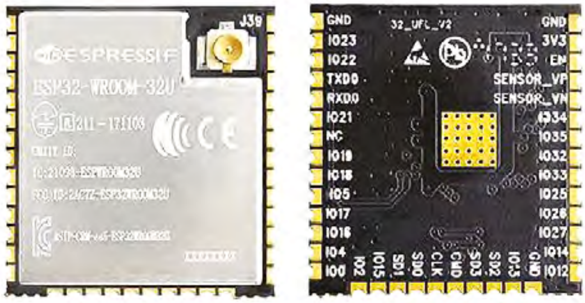

FIGURE 1. Appearance of the ESP32-WROOM-32U module [2]

Description of the structure and components of the measurement system

In the design process of any electronic device, a key step is the development of a custom electrical diagram, which specifies how all components are connected into a coherent and functional system. This diagram reflects the designer's operational concept and forms the basis for subsequent project implementation stages. Its accuracy is fundamental – even a minor error can lead to design flaws, which in mass production can generate significant financial losses. Design documentation should clearly present the device's structure and operating principle, which is particularly important when collaborating with the client, where a clear presentation of technical assumptions is essential. Another crucial element of the design process is the appropriate selection of electronic components, consistent with the functional requirements and parameters specified in the technical specifications.

Before commencing the actual design of the measurement system for the air quality monitoring system, an analysis of available electronic components was conducted. Among these, those that enabled the creation of a complete, efficient, and cost-effective measurement system were selected. The selection of components was based on project experience and an analysis of the technical literature. In order to verify the operation and accuracy of low-cost environmental sensors, a prototype test system based on the ESP32 microcontroller, equipped with temperature and gas sensors, was developed (Fig. 2).

The station's design was designed to ensure stable power supply and uniform current and voltage distribution to all system components. This approach minimizes interference and measurement errors during device operation. During the prototyping phase, breadboards were used to serve as a temporary mounting platform for electronic components. The final design was implemented on a pre-designed printed circuit board (PCB) measuring 8x7 cm, prepared in the EasyEDA engineering environment [5].

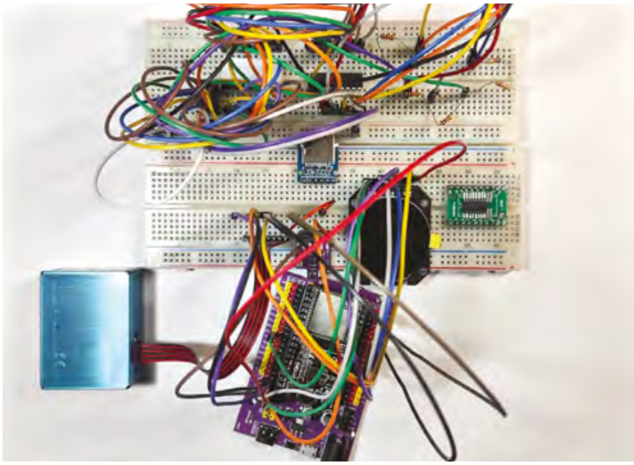

FIGURE 2. Prototype measurement system based on the ESP32 microcontroller

Male-to-male and female-to-male cables were used to connect the individual system components, enabling flexible and permanent connection of measurement elements. A popular AMS1117 linear voltage regulator [6] was used to ensure stable power supply for each sensor. The system's power source is a 9 V/3 A DC power supply, which supplies voltage in parallel to the microcontroller and regulator. The heart of the control system is an ESP32 microcontroller, powered by 3.3 V, responsible for the acquisition, processing, and transmission of measurement data. A 1.28" round TFT display [6] with a resolution of 240×240 px, based on IPS technology, was used to present the results, ensuring good readability and contrast.

The measurement module was equipped with BME680 [8] and PMS5003 [9] environmental sensors, enabling the measurement of temperature, humidity, pressure, volatile organic compounds, and suspended particulate matter. Additionally, the design included a TEMT6000 [10] light sensor, which automatically adjusts the screen brightness depending on the ambient light level, thus reducing power consumption. Each of the components used (Fig. 3) was individually tested before the measurements began. Additional small electronic components were also used to support the system's operation.

The BME680 temperature and humidity sensor was selected for the project because it is one of the most widely used and cost-effective environmental sensors in engineering applications. It is unique in its ability to simultaneously measure four basic air parameters: temperature, humidity, atmospheric pressure, and volatile organic compound (VOC) concentration. Additional parameters, such as carbon dioxide (CO_2) concentration and the air quality index (IAQ), are calculated programmatically based on dedicated algorithms.

The sensor, housed in a compact metal housing, is widely used in indoor air quality monitoring systems. Inside the sensor is a MOX (Metal Oxide Semiconductor) sensor, which detects VOCs by adsorption of molecules onto a metal oxide surface. Unlike many other detectors, the BME680 measures the combined level of all organic compounds, making it a non-specific sensor for individual gases but more versatile in general air quality analysis.

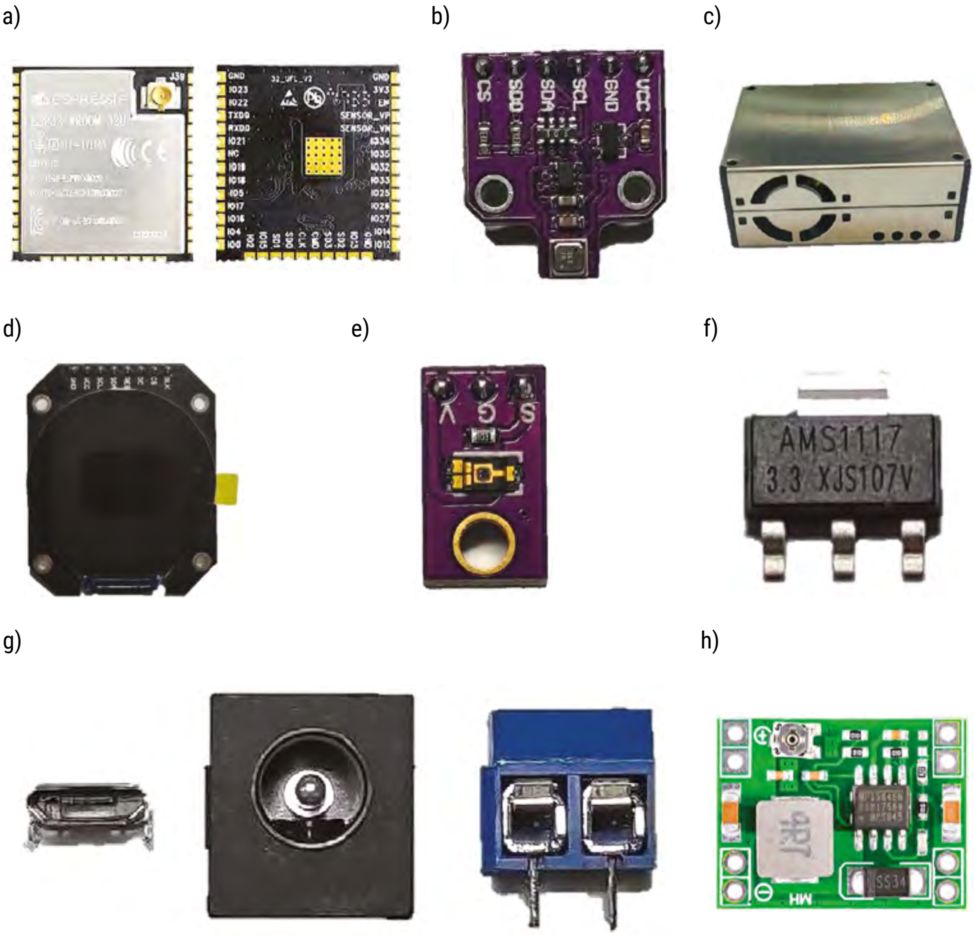

FIGURE 3. ESP32-WROOM-32U (a); BME680 (b); PMS5003 (c); 1.28” TFT display (d); TEMT6000 sensor (e); AMS1117 (f); power connectors used (g); converter (h)

The manufacturer, Bosch Sensortec, developed dedicated BSEC (Bosch Software Environmental Cluster) software [8] for this system, which includes a set of intelligent computational algorithms. It enables automatic determination of the air quality index (IAQ), estimation of VOC and CO_2 concentrations, and correction of environmental measurements. Thanks to its various operating modes, the sensor boasts very low power consumption – in power-saving mode, it consumes approximately 0.1 mA, while in standard mode, it consumes approximately 1 mA, allowing for efficient management of the entire system's energy budget.

The second important measurement element of the system is the PMS5003 sensor from Plantower, designed for the detection of suspended particulate matter using a laser (optical) method. This module combines small sizes with high measurement precision. Plantower specializes in the development and production of modern air quality sensors, ensuring reliable operation in industrial and consumer applications. The PMS5003 sensor utilizes a laser light scattering method, a patented hexagonal shielding structure, and enables real-time measurement [9].

The device's measurement range covers PM1.0, PM2.5, and PM10 dust fractions, with a particle size range of 0.3–10 μm, and a resolution of 1 $\mu g/m^3$. The PMS5003 sensor communicates with the ESP32 microcontroller via a UART interface, while the BME680 sensor uses an I^2C bus.

To fully illustrate the communication and data flow between the individual system components, a detailed block diagram (Fig. 4) was developed, which illustrates the operating logic of the smart measuring station and the interactions between the measurement modules and the microcontroller.

An electronic device should be housed in a properly designed enclosure that protects fragile electronic components. It provides a fundamental barrier against environmental factors and mechanical damage. A properly designed enclosure can also protect the device from dust, moisture, water, extreme temperatures, as well as electromagnetic interference (EMI) and radio frequency interference (RFI). Furthermore, it limits direct user access to live parts, improving operational safety.

After developing the printed circuit board (PCB) design, it was possible to begin designing an ergonomic and aesthetically pleasing enclosure. For this purpose, precise dimensional measurements of all electronic components, including the PCB, connectors, display, and sensors, were taken. This data was then transferred to a 3D CAD environment, where spatial modeling of individual components and their placement within the enclosure were performed.

This approach enabled the precise arrangement of components in three-dimensional space, optimizing the placement of mounting holes, buttons, communication ports, and ventilation openings. By transferring the actual dimensions of the electronic components to the digital model, it was possible to design a compact, functional, and easy-to-assemble enclosure (Fig. 5).

The Autodesk Fusion 360 environment [11] was used to create the proprietary 3D enclosure model, which was used for analysis, visualization, and verification of the design's ergonomics. This environment enables both parametric modeling and the creation of realistic visual renderings.

All housing components, except the transparent plexiglass cover, were 3D printed using FFF (Fused Filament Fabrication) technology. The prototype was manufactured using a biodegradable polymer – polylactide (PLA), which is low-cost, easy to process, and environmentally friendly. This material is widely used in engineering and educational projects due to its dimensional stability and the absence of a closed build chamber during printing.

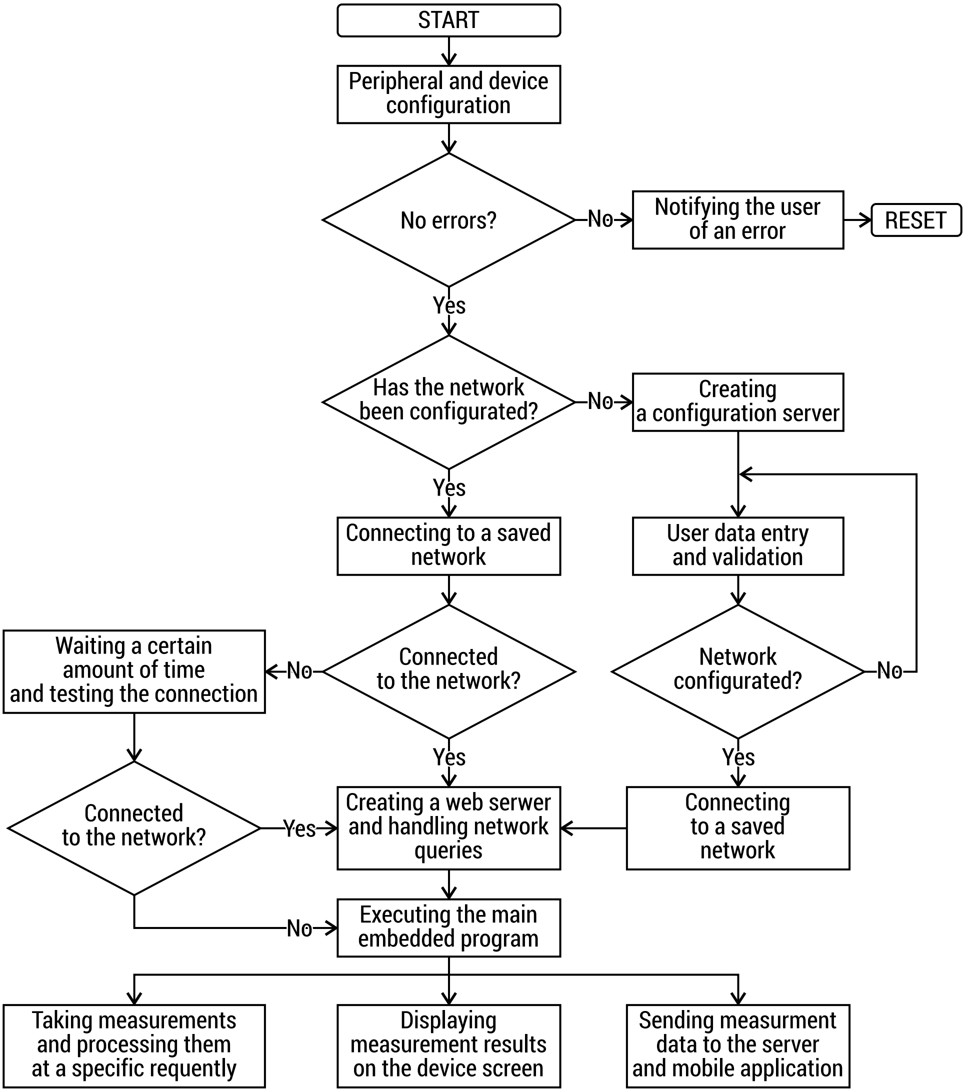

FIGURE 4. Block diagram of the measurement system program

The device is programmed to provide measurement data both locally – on the built-in TFT display and remotely via a dedicated mobile app for Android (version 5.0 and higher). This allows the user to monitor air parameters without the need for physical contact with the device, significantly improving user comfort. This solution allows for real-time readings of temperature, humidity, atmospheric pressure, VOC concentration, and particulate matter (PM) from anywhere within the local network range.

To ensure proper remote monitoring, the measuring station and the mobile device must be connected to the same Wi-Fi network, maintaining adequate signal strength throughout the entire user area (e.g. home, office, laboratory). This solution aligns with the principles of building automation systems (BAS), increasing their functionality and usability [12, 13].

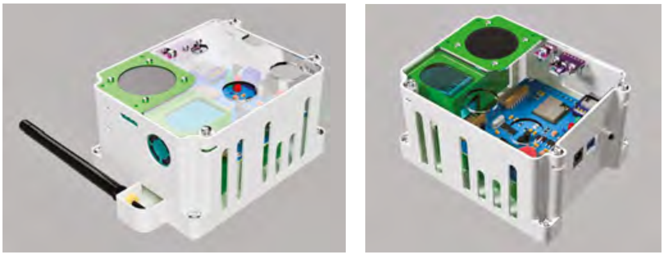

FIGURE 5. Three-dimensional model of the device (isometric views)

Fig. 6 presents screenshots of the complete, fully functional interface of the mobile application, enabling remote monitoring and visualization of environmental parameters. The application was developed using MIT App Inventor, a high-level visual programming language developed by the Massachusetts Institute of Technology (MIT) [14].

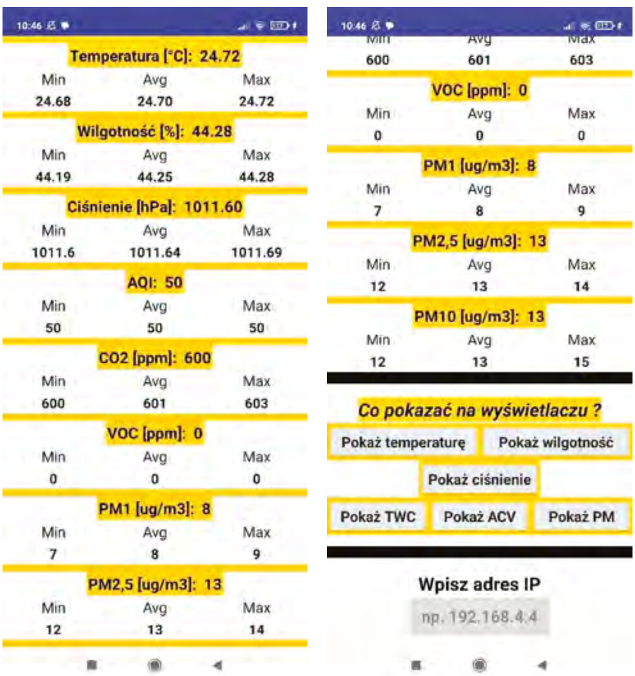

FIGURE 6. Graphical interface of the mobile application for an Android smartphone

Devices designed for monitoring air parameters should be able to communicate with the Internet, enabling remote access to measurement data and central management of results without the need for physical presence at the device. This solution significantly enhances the system's functionality and allows for integration with other IoT infrastructure components.

As part of the project, an ESP32 microcontroller was programmed to transmit measurement data to the ThingSpeak cloud platform, developed by MathWorks (Fig. 7) [15]. This platform enables automatic recording, analysis, and visualization of results in real time, enabling continuous monitoring of environmental changes. Data is presented in the form of dynamic graphs, updated without user intervention, eliminating the need for manual reading and archiving.

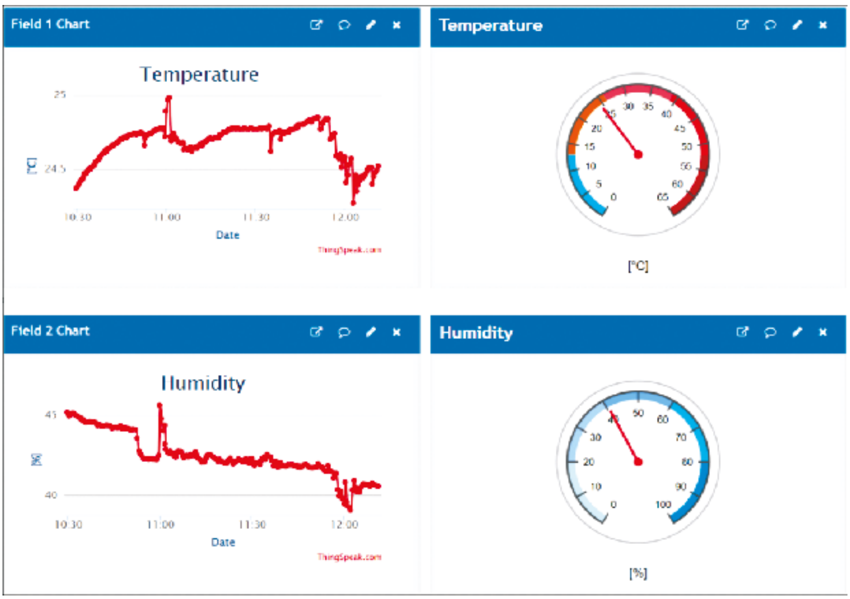

FIGURE 7. Example visualization of air temperature and humidity using a graph and a circular gauge

An additional advantage of this solution is the ability to remotely access data from any mobile device or computer, regardless of the network to which the measurement station is connected. This allows users to monitor measurement results from anywhere, which is particularly important in home, educational, and industrial applications.

After building the entire system, it was decided to perform some measurements and check the correct operation of the program (Fig. 8).

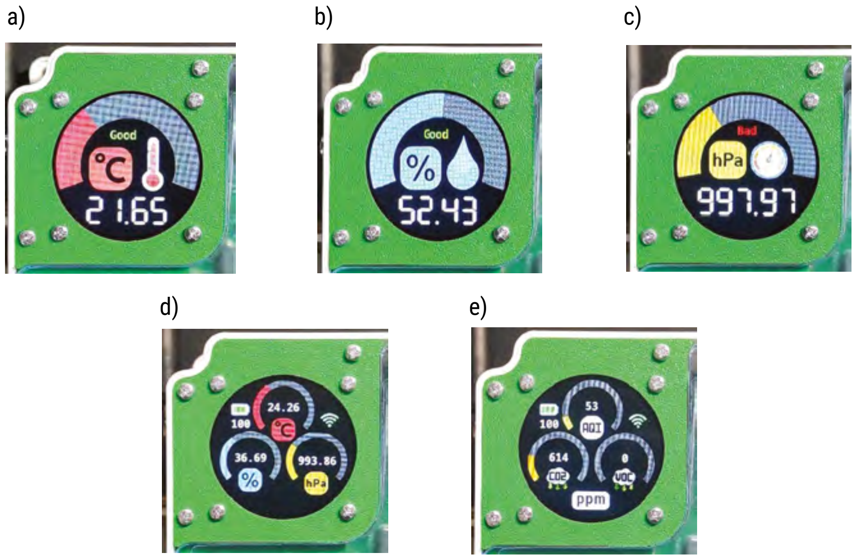

FIGURE 8. Photo illustrating the display of selected parameters of the BME680 sensor on a physical device: a) temperature; b) humidity; c) atmospheric pressure; d) a summary of the three mentioned parameters; e) a summary of the AQI, CO_2 and VOC parameters

Analysis of results

To assess the correct operation of the designed measurement system, tests were conducted in an environment with dynamically changing air parameters. The tests were conducted in a residential room with an area of approximately 20 m^2 and a volume of 54 m^3. The device operated continuously for 24 hours, placed at a fixed measurement point to ensure repeatable test conditions. All measurement data was transmitted in real time via Wi-Fi to the ThingSpeak platform, where it was analyzed and visualized. Prior to the actual measurement, the device underwent a 48-hour calibration, which allowed the sensors to stabilize and obtain reliable results.

Fig. 9 presents the temperature, relative humidity, and atmospheric pressure measurement results recorded during the experiment. The data indicates the correct and stable operation of the measurement system and the high sensitivity of the sensors to environmental changes. Natural fluctuations in values were observed during the study period, resulting from typical indoor activities, such as opening windows or changing microclimate conditions.

Preliminary results confirm that the designed system operates correctly and meets its functional requirements, providing reliable measurement of basic indoor air parameters. Further research is planned with an expanded scope – including measurement of gaseous pollutants and suspended particulate matter – to fully verify the performance of the developed device.

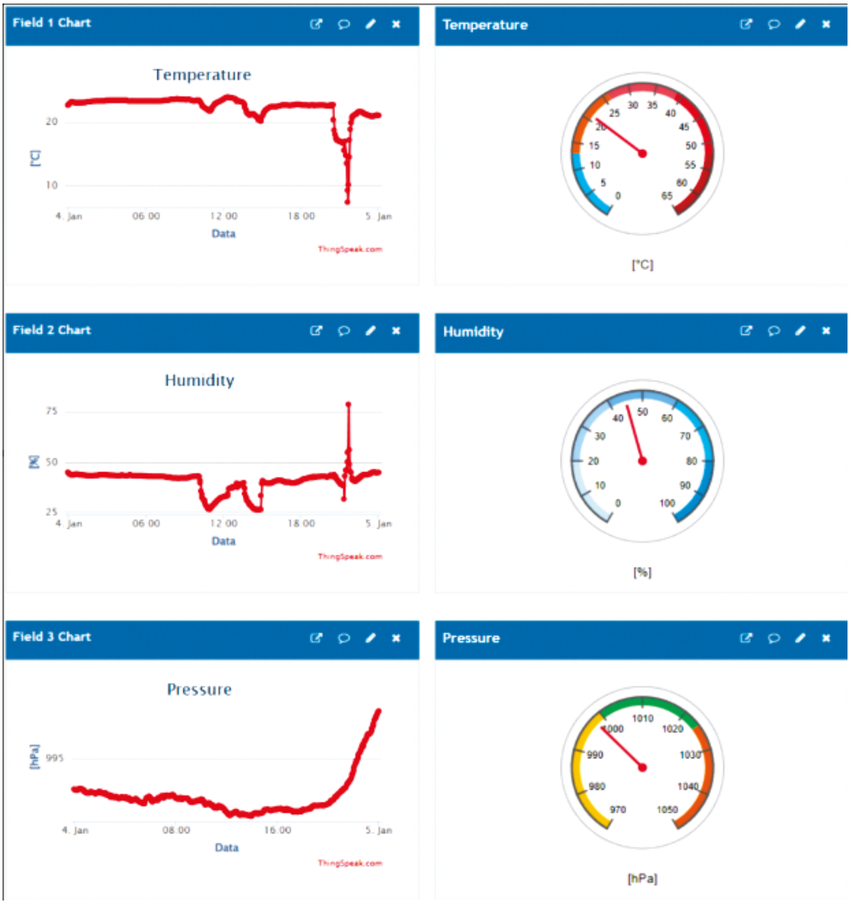

FIGURE 9. **Temperature, humidity and pressure measurements in a dynamic environment**

Future research phases will expand the scope of testing to include measurements of additional air quality parameters, such as carbon dioxide (CO_2) concentration, volatile organic compounds (VOCs), and the relative humidity index (AQI). Additionally, the device will be analyzed for its accuracy in detecting suspended particulate matter of various granularities – PM1.0, PM2.5, and PM10 [16]. This will allow for a comprehensive assessment of the system's effectiveness in monitoring the indoor environment and its response to changing ambient conditions. The planned experiment will be conducted in an environment corresponding to typical office work conditions. The aim will be to replicate natural changes in air quality resulting from everyday activities, such as the presence of people, the use of office equipment, and room ventilation. Test conditions will be maintained in a room with an area of approximately 8 m^2 and a volume of 22 m^3, equipped with standard office furniture and equipment. Measurements will be conducted between 10:00 AM and 8:00 PM, allowing for the recording of a full daily activity cycle. Initial preparations will include a 48-hour calibration of the device under reference conditions, according to a previously developed procedure.

Previous prototype tests have already confirmed the high effectiveness of the developed system, both in terms of measurement stability and the accuracy of recorded data. The device demonstrated its ability to operate reliably in continuous mode and respond immediately to changes in air quality. When combined with the ThingSpeak platform, measurement results are presented in real time, making the system a fully functional IoT solution. The planned expansion of the tests will not only allow for the validation of the accuracy of individual sensors but also for a comprehensive assessment of the device's practical usefulness in various environments – from office to residential.

Summary and conclusions

This article presents a proprietary design for a compact measuring station designed for precise monitoring of environmental parameters. The device records key meteorological data such as temperature, humidity, atmospheric pressure, and air quality indicators (including particulate matter and VOCs). The obtained results confirmed the high accuracy and stability of the sensors, demonstrating the effectiveness of the developed measurement concept.

The system was designed for integration with IoT platforms and modern building automation systems. This enables automatic control of ventilation, heating, or air conditioning based on actual ambient conditions, resulting in greater user comfort and more efficient energy management. Access to data via a web-based analytical platform enables real-time visualization and remote monitoring from any location.

In summary, the developed measuring station represents a modern and flexible IoT solution that can be used in both smart buildings and standalone environmental monitoring systems. Further development work will include increased structural robustness, calibration precision, and module miniaturization, enabling even broader application of the developed technology in practical applications.

References

[1] Manisalidis, I., Stavropoulou, E., Stavropoulos, A., Bezirtzoglou, E. (2020). Environmental and Health Impacts of Air Pollution: A Review. *Frontiers in Public Health*, *20*(8), 14. https://doi.org/ 10.3389/fpubh.2020.00014

[2] Poyyamozhi, M., Murugesan, B., Rajamanickam, N., Shorfuzzaman, M., Aboelmagd, Y. (2024). IoT – A Promising Solution to Energy Management in Smart Buildings: A Systematic Review, Applications, Barriers, And Future Scope. *Buildings*, *14*(11), 3446. https://doi.org/10.3390/buildings14113446

[3] Sinopoli, J. (2009). *Smart buildings systems for architects, owners and builders*. Butterworth-Heinemann.

[4] ESPRESSIF. (n.d.). Retrieved from https://www.espressif.com/en/products/socs/esp32

[5] EasyEDA. (n.d.). Retrieved from https://easyeda.com/pl

[6] Advanced Monolithic Systems. (n.d.). AMS1117, 1A Low Dropout Voltage Regulator. Retrieved from http://www.advanced-monolithic.com/pdf/ds1117.pdf

[7] msalamon. (n.d.). Okrągły wyświetlacz TFT IPS 1,28" GC9A01 240x240px SPI Czarny. Retrieved from https://sklep.msalamon.pl/produkt/okragly--wyswietlacz-tft-ips-

[8] 128-czarny

[9] BOSCH. (n.d.). Gas sensor BME680. Retrieved from https://www.bosch-sensortec.com/products/environmental-

[10] sensors/gas-sensors/bme680

[11] PLANTOWER. (n.d.). Laser PM2.5 Sensor. PMS5003. Retrieved from https://www.plantower.com/en/products_33/74.html

[12] msalamon. (n.d.). Czujnik natężenia światła TEMT6000. Retrieved from https://sklep.msalamon.pl/produkt/temt6000-czujnik-natezenia-swiatla

[13] AUTODESK. Retrieved from https://www.autodesk.com/pl/products/fusion-360/overview

[14] Lavrinovica, I., Judvaitis, J., Laksis, D., Skromule, M., Ozols, K. (2024). A Comprehensive Review of Sensor-Based Smart Building Monitoring and Data Gathering Techniques. *Applied Sciences*, *14*(21), 10057. https://doi.org/10.3390/app142110057

[15] Jia, M., Komeily, A., Wang, Y., Srinivasan, R. S. (2019). Adopting Internet of Things for the development of smart buildings: A review of enabling technologies and applications. *Automation in Construction*, *101*, 111–126. https://doi.org/10.1016/j.autcon.2019.01.023

[16] MIT APP INVENTOR. (n.d.). Retrieved from https://appinventor.mit.edu

[17] ThingSpeak. (n.d.). Retrieved from https://thingspeak.mathworks.com/

[18] Jo, Jun Ho et al. Wdrożenie systemu monitorowania jakości powietrza opartego na Internecie Rzeczy (IoT) do badania stężenia pyłu zawieszonego (Pm10) w tunelach metra. *Międzynarodowe Czasopismo Badań Środowiskowych i Zdrowia Publicznego*, *17*(15), 5429.

DOI: 10.24427/978-83-68673-38-8_5

Chapter 5. Analysis of the influence of load resistance on the efficiency in WPT systems

Agnieszka CHOROSZUCHO[1], *Jacek Maciej STANKIEWICZ*[2], *Norbert WAŚKIEWICZ*[3]

[1]*Bialystok University of Technology, Faculty of Electrical Engineering*
e-mail: a.choroszucho@pb.edu.pl
[2]*e-mail: alfjoker@poczta.onet.pl*
[3]*Bialystok University of Technology, Faculty of Computer Science*
e-mail: norbert.waskiewicz.109529@student.pb.edu.pl

Streszczenie. W rozdziale przedstawiono analizę systemu bezprzewodowego przesyłu energii (WPT) z wykorzystaniem okresowo rozłożonych cewek planarnych. Celem analizy było zbadanie wpływu rezystancji obciążenia na sprawność tych systemów. Sprawdzono, dla jakich rezystancji dany system może osiągnąć maksymalną sprawność i moc obciążenia. W analizie uwzględniono liczbę zwojów. Do analizy wykorzystano dwa podejścia (analityczne i numeryczne). Analizę numeryczną przeprowadzono z wykorzystaniem Metody Elementów Skończonych (MES). Metoda analityczna została odniesiona do rozwiązania równoważnego obwodu elektrycznego. Wyniki analizy wykazały, że większe wartości maksymalnej sprawności osiągnięto dla modelu z cewką kołową niż dla cewki kwadratowej, a różnica nie przekroczyła 19%. Wraz ze wzrostem liczby zwojów rosną wartości rezystancji obciążenia, dla których osiągnięto maksymalną sprawność i moc odbiornika. Wyniki pozwolą na projektowanie systemów WPT z odpowiednim doborem rezystancji obciążenia w celu osiągnięcia maksymalnej sprawności.

Abstract. The chapter presents an analysis of a Wireless Power Transfer (WPT) system with the use of periodically distributed planar coils. The aim of the analysis was to investigate the impact of the load resistance on the efficiency for these systems. Tests were carried out to understand for which resistances a given system can achieve maximum efficiency and load power. The analysis took into account the number of turns. Two approaches (analytical and numerical) were used for the analysis. The numerical analysis was performed using the Finite Element Method (FEM). The analytical method was related to the solution of the equivalent electric circuit. The results of the analysis showed that greater values of maximum efficiency were achieved for the model with a circular coil than for a square coil, and the difference did not exceed 19%. With the growth in the number of turns, the values of the load resistance grow, for which the maximum efficiency and power of the receiver were achieved. The results will allow the design of WPT systems with the proper selection of load resistance in order to achieve maximum efficiency.

Słowa kluczowe: bezprzewodowe przesyłanie mocy, indukcyjne przesyłanie mocy, rezystancja obciążenia, analiza numeryczna

Keywords: wireless power transfer, inductive power transfer, load resistance, numerical analysis, circuit analysis

Introduction

Nowadays, there is a growing number of devices using Wireless Power Transfer (WPT) technology [1, 2]. Current trends, visible in wireless vehicle charging systems [5, 6] and modern electronics [3, 4, 5], have also led to the extension of the concept of the so-called inductive power transfer (IPT). Among others, in the case of the growing number of mobile devices, or remotely operated sensors [6, 7], a constant supply of energy is necessary to ensure continuous operation. In this context, WPT is considered as an alternative method of fast charging wireless devices.

In order to implement IPT, a pair of coils [6, 8] is used together with, for example, additional intermediate coils [9, 10], or a system of coils [11, 12]. Technological solutions with multiple coils usually operate at high frequencies [13]. At low frequencies ($f < 1000$ kHz), systems of resonating coils (resonators) are considered [14, 15]. In these solutions, in the space between the transmitter and receiver, several additional resonators support energy transfer. So far, a detailed analysis of the series configuration of the resonators has been carried out. However, the analysis of the series-parallel distribution of planar coils working as a group of energy transmitters and receivers is not yet fully developed. In addition, wireless charging is considered in systems located in hard-to-reach places, e.g. in the case of groups of beacons [16], or in buildings with sensors inside walls and ceilings [17]. This technology is widely developed in medicine [18]. A very important aspect in WPT systems is also the impact of the environment on the quality of system operation and achieving high efficiency of the system [19].

The power supply or charging of many devices located in close proximity to each other can be simplified by using WPT systems, made as networks with periodically arranged coils that form surface elements for transmitting or receiving energy. This solution increases the density of the transmitted power, and also enables the simultaneous powering of many devices fromone source. Potential applications of this type of WPT systems focus mainly on the simultaneous charging of a number of sensors [20]. From the point of view of applications in high-power systems, the periodic WPT elements proposed in the chapter can be considered for the design of distributed vehicle charging systems in large parking lots.

The design and analysis of the mentioned WPT systems involves the use of three-dimensional numerical models used to calculate the distribution of the magnetic field in the system. In order to minimize the complexity of the problem and the number of degrees of freedom of the model, the chapter proposes two ways of analyzing the system based on the structure and parameters of a single segment. Numerical analysis and a solution based on the electrical circuit were considered. The use of numerical modeling methods significantly simplifies the problem of engineering calculations of the proposed systems, introducing the possibility of their design using software for numerical calculations. Both proposed approaches reduce the size and complexity of commonly utilized numerical and circuit models.

Analyzed models

The presented analysis was focused on selected configurations of planar systems, enabling wireless energy transfer (through inductive coupling between the energy source and receiver), in which it is possible to process and transfer it. The considered systems were based on multi-segment surfaces, composed of identical components with selected geometry (periodically distributed over these surfaces) acting as a source and receiver with a dispersed but ordered distribution of elementary energy sources/receivers. This configuration requires taking into account the frequency range of the power source, as well as the geometry of the system.

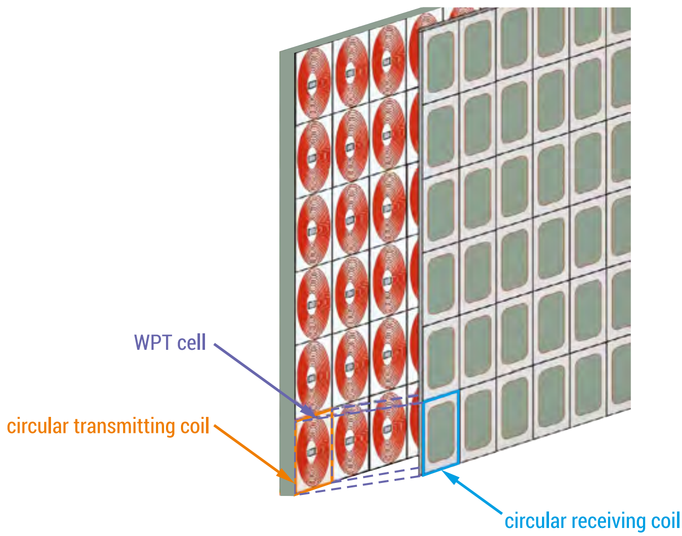

FIGURE 1. The analyzed periodic WPT system with planar coils

Each coil has a compensation capacitor in series with the coil. The Tx coils create the transmitting surface, and Rx coils the receiving surface. Between those surfaces, wireless energy transfer takes place. The transmitting surface has a sinusoidal voltage source (U_{sc}). The receiving coils are combined to the loads (Z_l). Multiple receivers can be supplied simultaneously.

Methods analysis

Each of the methods (analytical, numerical, experimental) has advantages and disadvantages. Knowledge of the methods and needs imposed by the analyzed system allows for the appropriate selection of the method of task implementation and elimination of errors. Knowledge of numerical methods enables the proper use of calculation packages (e.g. Matlab, Maple, Mathematica), as well as provides the necessary basis for independent solving of specific, increasingly complex, engineering problems. This requires, on the one hand, the awareness of the essence of the problems to be solved, and on the other hand, knowledge of the methods of solving them.

The Finite Element Method (FEM) is one of the numerical methods for solving differential equations. These equationsdescribe phenomena and processes known in nature, physics and technology. The use of FEM in solving technical problems results from the possibility of achieving the result of an equation that cannot be solved analytically or is too complex and time-consuming.

Discretization is the first step in creating the FEM model. It consists in dividing the area into smaller elements. Elements have common nodes (points) and additionally contain information about mutual proximity. Discretization is crucial in FEM issues, because it determines the length of the calculations and the accuracy of the results. Simulation of physical processes using the Finite Element Method, in the final stage, consists in solving a system of algebraic equations. The number of unknowns is closely related to the number of nodes that make up the mesh and the number of unknowns in each node. By increasing the mesh density, we increase the calculation time and at the same time increase the accuracy of the solution. The Comsol Multiphysics 4.3b package was used to prepare a numerical model presenting the proposed solution and to perform computer simulations (Fig. 2). Comsol can model wave problems in the frequency domain using the additional *Radio Frequency* module. A detailed description of the boundary conditions can be found in the Comsol documentation [22, 23]. The compensation capacitor (C_{cp}) was modelled as a lumped element. To model the infinite dielectric background, two layers (PML) were used at the top and bottom of the WPT cell [24].

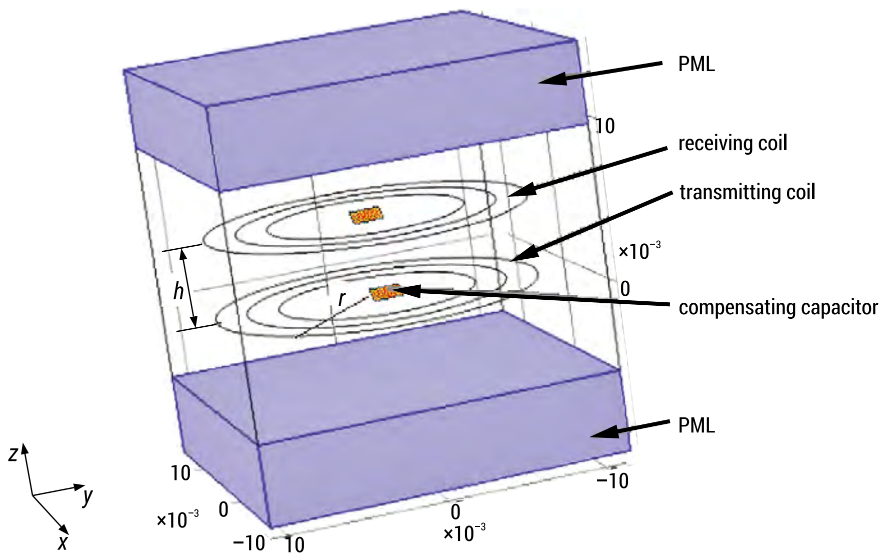

FIGURE 2. Geometry of the numerical model

In the calculations, a magnetic vector potential (Equation (1)) and the Helmholtz equation (Equation (2)) were used:

$$\mathbf{A} = \left[\mathbf{A}_x \mathbf{A}_y \mathbf{A}_z \right] \tag{1}$$

$$\nabla \cdot \left(\frac{1}{\mu} \nabla \cdot \mathbf{A} \right) - \mathrm{j}2\pi f \sigma \, \mathbf{A} = \mathbf{J}_{ex} \tag{2}$$

$\mathbf{J}_{ex}$ – an external current density [A/m^2] results from a voltage supply (U_{sc}). Equations (1)–(2) by FEM were solved.

The power transfer efficiency is calculated from:

$$\eta = \frac{P_{ld}}{P_{sc}} \cdot 100\% \tag{3}$$

where: the active power of the Rx coil is represented by Equation (4) and the power of the Tx coil is calculated form Equation (5):

$$P_{ld} = R_o \left| \underline{I}_{ld} \right|^2 \tag{4}$$

$$P_{sc} = U_{sc} \cdot \underline{I}_{sc} \tag{5}$$

Results

Calculations were made at the frequency of 1000 kHz, at the distances $h = r/2$ and $h = r = 10$ mm, for the small and large coils, $U_{sc} = 1$ V, number of turn coils $n = 10$ and 30. The influence of the load resistance ($Z_l = R_o$) on the power and efficiency of the WPT system was investigated.

Characteristics η, P_{sc} and P_{ld} powers are shown on the graphs (Figs. 3–6). The numerical analysis results are represented as solid lines (marked as numerical in the legend). The results of the analytical analysis [21] are represented by dots (marked as analytical in the legend).

The results show that as the number of turns n grows, this difference becomes smaller and smaller. The shape of the characteristics is maintained regardless of n. As n grows, the range of the load resistance R_o, for which η exceeds 50% grows. η or the load power P_{ld} grows with the growth of R_o, and then, after reaching the maximum value, they begin to drop. As n grows, the maximum value of P_{ld} power or η is achieved at increasingly greater R_o values.

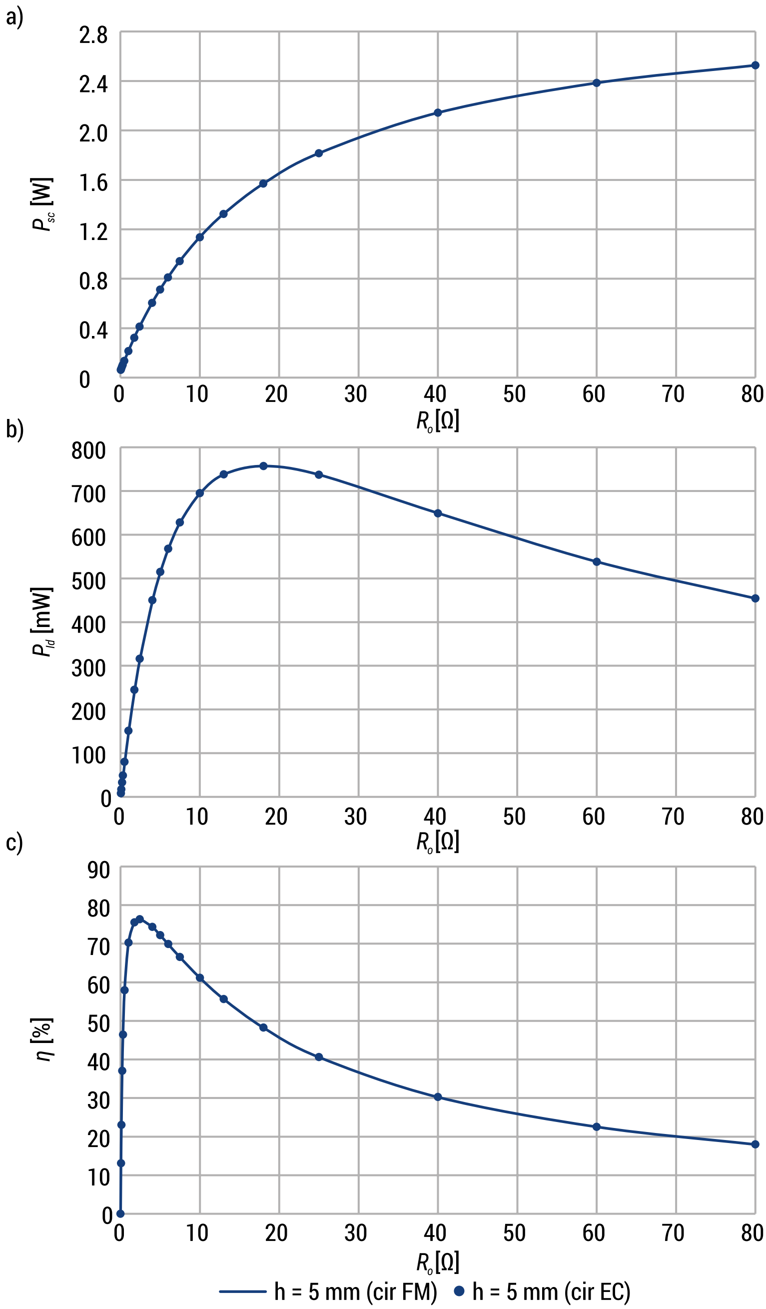

FIGURE 3. Results for r = 10 mm, n = 10, h = 5 mm: (a) P_{sc}, (b), P_{ld}., (c) η

Doubling the distance between the coils h causes a growth in the maximum power P_{sc}, and a drop in the maximum power P_{ld}, regardless of the analyzed case. η also drops, the largest drop in value occurs for n = 10. In this case, η does not exceed 50%.

The R_o range, for which η exceeds 50%, also drops. The maximum values of η and P_{ld} are achieved for lower R_o values compared to lower h. The shape of the characteristics is preserved regardless of n.

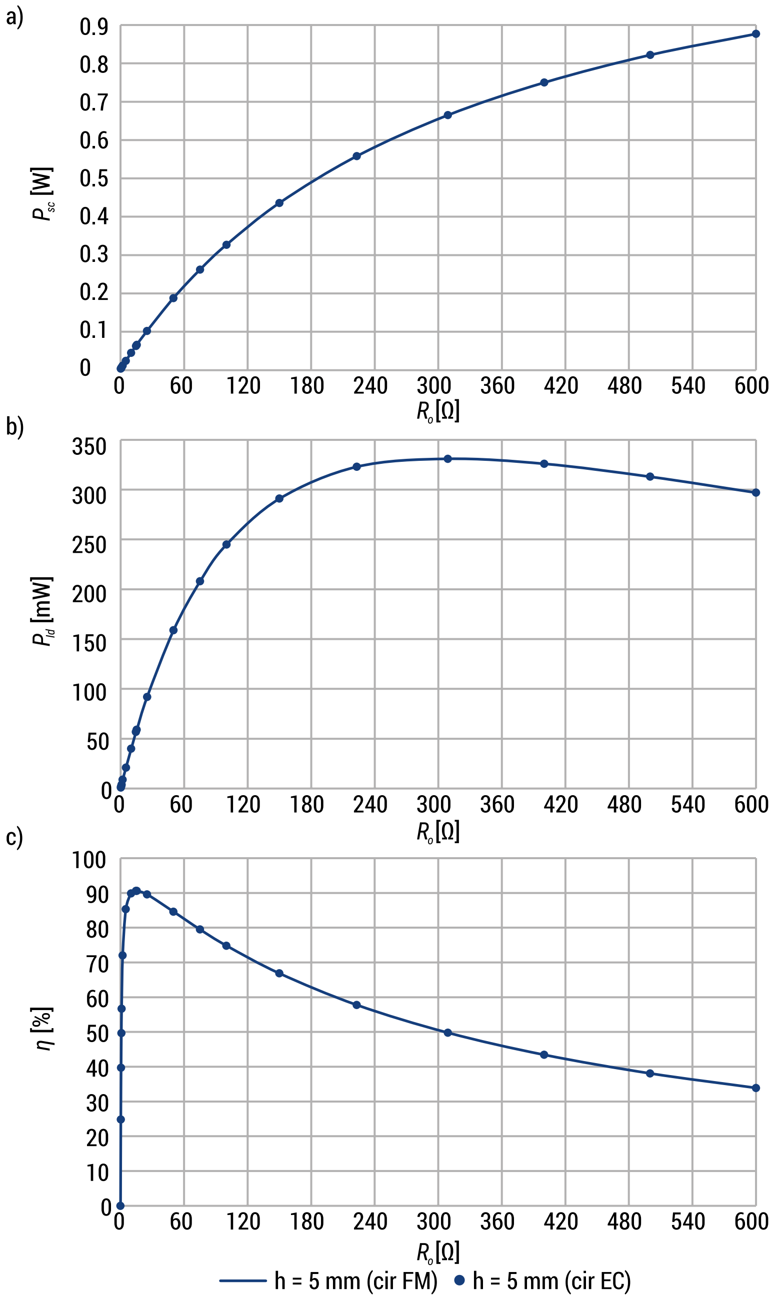

FIGURE 4. Results for r = 10 mm, n = 30, h = 5 mm: (a) P_{sc}, (b), P_{ld}., (c) η

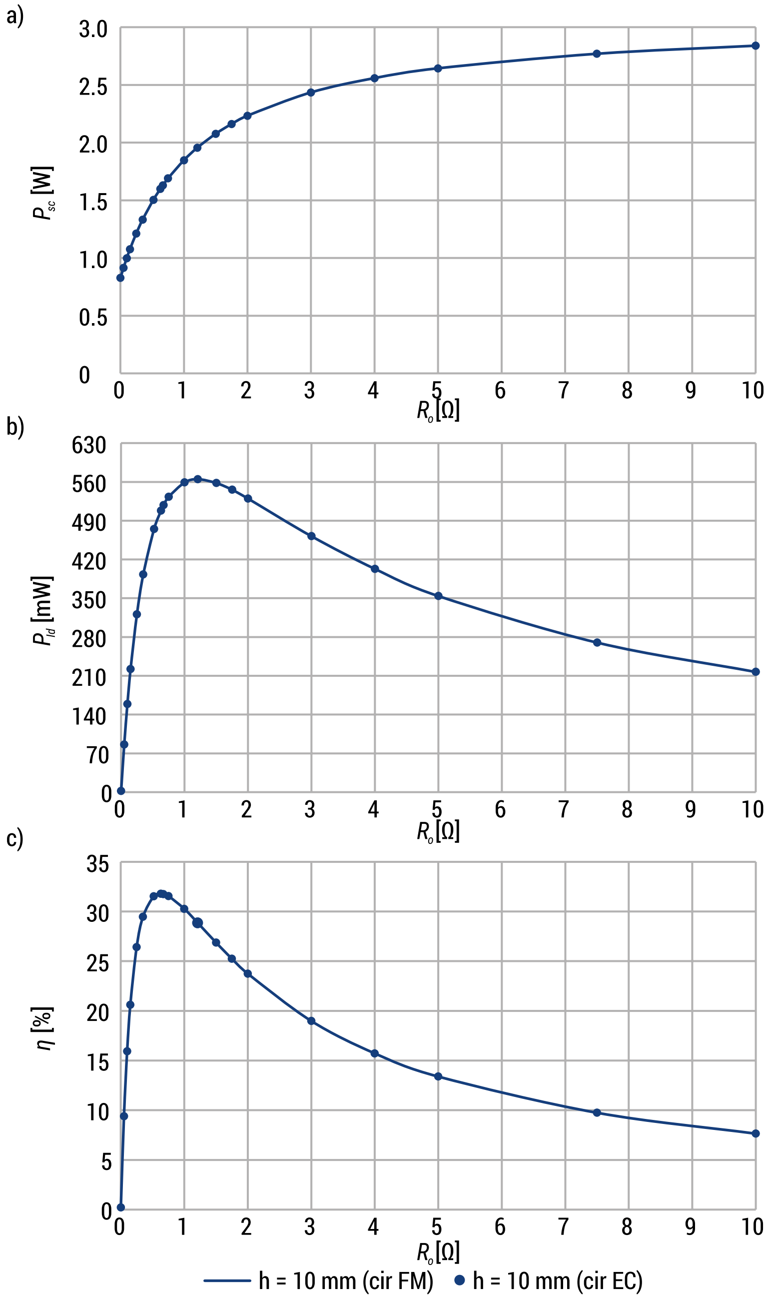

FIGURE 5. Results for r = 10 mm, n = 10, h = 10 mm: (a) P_{sc}, (b), P_{ld}., (c) η

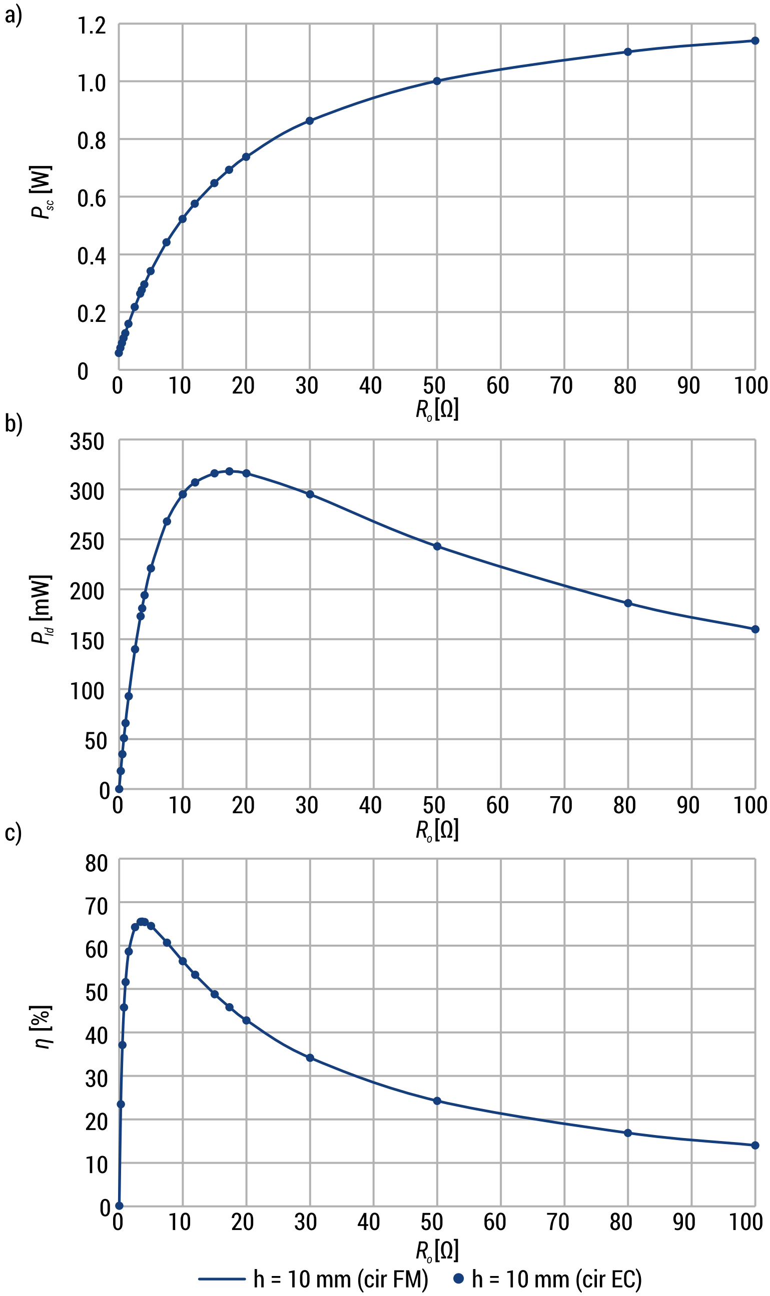

FIGURE 6. Results for r = 10 mm, n = 30, h = 10 mm: (a) P_{sc}, (b), P_{ld}., (c) η

Summary and conclusions

The idea of wireless energy transmission has been discussed for many years. In recent years, however, there is an increasing trend towards practical applications of WPT. This paper presented a WPT system with a periodic distribution of low-power planar coils. A multi-variant analysis was performed in order to find the load resistance values at which the system efficiency is the highest. The analysis took into account the variability of the number of turns, and the distance between the transmitting and receiving coils.

The proposed use of an equivalent circuit, represented by a single WPT cell, gave a simpler and faster solution. The applied analysis methods can be used to assess the properties of the WPT system and related parameters.

The paper presents a numerical and analytical analysis of the WPT system at a frequency of 1000 kHz. The impact of the load resistance change on the power and efficiency for the coils was investigated. There is an almost two-fold drop in the maximum η of the system (the maximum η then does not exceed 30% for a square coil and 50% for a circular one). This relationship was observed when the distance between the transmitting and receiving coils was doubled. Depending on the size of the coil and n, R_o values are variable. With the growth of these parameters, the values of R_o grow, for which the maximum η and P_{ld} power were achieved. Growing the distance between the coils in the WPT system reduces the value of R_o, for which the maximum η and P_{ld} power is achieved. The achieved results can be used in the design of WPT systems, selecting the R_o value in such a way as to achieve the greatest values of η or P_{ld}.

References

[1] Barman, S. D., Reza, A. W., Kumar, N., Karim, M. E., Munir, A. B. (2015). Wireless powering by magnetic resonant coupling: Recent trends in wireless power transfer system and its applications. *Renewable and Sustainable Energy Reviews*, *51*, 1525–1552. https://doi.org/10.1016/j.rser.2015.07.031

[2] Sun, L., Ma, D., Tang, H. (2018). A review of recent trends in wireless power transfer technology and its applications in electric vehicle wireless charging. *Renewable and Sustainable Energy Reviews*, *91*, 490–503. https://doi.org/10.1016/j.rser.2018.04.016

[3] Eteng, A. A., Rahim, S. K. A., Leow, C. Y., Chew, B. W., Vandenbosch, G. A. E. (2016). Two-Stage Design Method for Enhanced Inductive Energy Transmission with Q-Constrained Planar Square Loops. *PLoS One*, *11*(2), e0148808. https://doi.org/10.1371/journal.pone.0148808

[4] Kim, T.-H., Yun, G.-H., Lee, W. Y. (2018). Asymmetric Coil Structures for Highly Efficient Wireless Power Transfer Systems. *IEEE Transactions on Microwave Theory and Techniques*, *66*(7), 3443–3451. https://doi.org/10.1109/TMTT.2018.2828438

[5] Tang, S. C., Lun, T. L. T., Guo, Z., Kwok, K.-W., McDannold, N. J. (2017). Intermediate range wireless power transfer with segmented coil transmitters for implantable heart pumps. *IEEE Transactions on Power Electronics*, *32*(5), 3844–3857. http://doi.org/10.1109/TPEL.2016.2584558

[6] Rim, C. T., Mi, C. (2017). *Wireless Power Transfer for Electric Vehicles and Mobile Devices*. John Wiley & Sons, Ltd. (pp. 473–490). https://doi.org/10.1002/9781119329084

[7] Fujimoto, K., Itoh, K. (2018). *Antennas for Small Mobile Terminals* (2nd ed., pp. 30–70). Artech House.

[8] Zhang, Z., Pang, H., Georgiadis, A., Cecati, C. (2019). Wireless Power Transfer – An Overview. *IEEE Transactions on Industrial Electronics*, *66*(2), 1044–1058. https://doi.org/10.1109/TIE.2018.2835378

[9] Rozman, M., Fernando, M., Adebisi, B., Rabie, K. M., Collins, T., Kharel, R., Ikpehai, A. (2017). A New Technique for Reducing Size of a WPT System Using Two-Loop Strongly-Resonant Inductors. *Energies*, *10*(10), 1614. https://doi.org/10.3390/en10101614

[10] Liu, X., Wang, G. (2016). A Novel Wireless Power Transfer System With Double Intermediate Resonant Coils. *IEEE Transactions on Industrial Electronics*, *63*, 2174–2180.

[11] El Rayes, M. M., Nagib, G., Abdelaal, W. G. A. (2016). A Review on Wireless Power Transfer. International Journal of Engineering Trends and Technology, *40*(5), 272–280. https://doi.org/10.14445/22315381/IJETT-V40P244

[12] Nikoletseas, S., Yang, Y., Georgiadis, A. (2016). *Wireless Power Transfer Algorithms, Technologies and Applications in Ad Hoc Communication Networks* (pp. 31–51). Springer.

[13] Stevens, C. (2015). Magnetoinductive waves and wireless power transfer. *IEEE Transactions on Power Electronics*, *30*(11), 6182–6190. https://doi.org/10.1109/TPEL.2014.2369811

[14] Zhong, W., Lee, C. K., Hui, S. Y. R. (2013). General analysis on the use of Tesla's resonators in domino forms for wireless power transfer. *IEEE Transactions on Industrial Electronics*, *60*(1), 261–270. https://doi.org/10.1109/TIE.2011.2171176

[15] Alberto, J., Reggiani, U., Sandrolini, L., Albuquerque, H. (2019). Accurate Calculation of the Power Transfer and Efficiency in Resonator Arrays for Inductive Power Transfer. *Progress in Electromagnetics Research B*, 83, 61–76. https://doi.org/10.2528/pierb18120406

[16] Martin, P., Ho, B. J., Grupen, N., Muñoz, S., Srivastasa, M. (2014). An iBeacon Primer for Indoor Localization. In *Proceedings of the 1st ACM Conference on Embedded Systems for Energy-Efficient Buildings (BuildSys'14), Memphis, USA, 3–6 November 2014* (pp. 190–191).

[17] Kim, D., Abu-Siada, A., Sutinjo, A. (2018). State-of-the-art literature review of WPT: Current limitations and solutions on IPT. *Electric Power Systems Research*, *154*, 493–502. https://doi.org/10.1016/j.epsr.2017.09.018

[18] Li, X., Zhang, H., Peng, F., Li, Y., Yang, T., Wang, B., Fang, D. (2012). A Wireless Magnetic Resonance Energy Transfer System for Micro Implantable Medical Sensors. *Sensors*, *12*(8), 10292–10308. https://doi.org/10.3390/s120810292

[19] Yang, Y., Cui J., Cui, X. (2020). Design and Analysis of Magnetic Coils for Optimizing the Coupling Coefficient in an Electric Vehicle Wireless Power Transfer System. *Energies*, *13*(16), 4143. https://doi.org/10.3390/en13164143

[20] Fitzpatrick, D. C. (2014). *Implantable Electronic Medical Devices* (pp. 7–35). Academic Press.

[21] Stankiewicz, J. M., Choroszucho, A. (2021). Comparison of the efficiency and load power in periodic Wireless Power Transfer systems with circular and square planar coils. *Energies*, *14*(16), 4975. https://doi.org/10.3390/en14164975

[22] *Introduction to the RF Module*, COMSOL; Version: COMSOL 4.3b; COMSOL Inc.: Burlington, MA, USA, 2013.

[23] *RF Module User's Guide*, COMSOL; Version: COMSOL 4.3b; COMSOL Inc.: Burlington, MA, USA, 2013.

[24] Zienkiewicz, O. C., Taylor, R. L., Zhu, J. Z. (2013). *The finite element method: its basis & fundamentals* (7th ed.). Butterworth-Heinemann.

DOI: 10.24427/978-83-68673-38-8_6

Chapter 6. Innovative technology of compact marine jet scrubbers

Dariusz BUTRYMOWICZ[1], Tadeusz ZIELIŃSKI[2], Jerzy GAGAN[3], Kamil ŚMIERCIEW[4], Michał ŁUKASZUK[5], Andrzej PAWLUCZUK[6], Adam DUDAR[7]

[1,3,4,5,6,7]Bialystok University of Technology, Faculty of Mechanical Engineering
[1]e-mail: d.butrymowicz@pb.edu.pl, ORCID: 0000-0003-3869-8347;
[2]Marine Projects Ltd.;
[3]e-mail: j.gagan@pb.edu.pl, ORCID: 0000-0002-7607-9654;
[4]e-mail: k.smierciew@pb.edu.pl, ORCID: 0000-0003-3869-8347;
[5]e-mail: m.lukaszuk@pb.edu.pl, ORCID: 0000-0002-8973-2405;
[6]e-mail: andrzej.pawluczuk@pb.edu.pl, ORCID: 0000-0003-3869-8347;
[7]e-mail: a.dudar@pb.edu.pl, ORCID: 0000-0001-6585-1795

Streszczenie. W rozdziale przedstawiono wyniki badań przeprowadzonych nad innowacyjnym układem oczyszczania spalin wykorzystującym technologię strumieniową, przeznaczonym do okrętowych silników wysokoprężnych o mocy 0,25 MW i 1,0 MW. Prace w zakresie rozpoznania zjawisk występujących w skruberze strumienicowym wykonano dla modelowej siłowni o mocy 40 kW. Prace obejmowały budowę i uruchomienie specjalnych stanowisk badawczych oraz wykonanie pomiarów emisji dla szerokiego spektrum stanów pracy. Odrębne zadanie badawcze dotyczyło efektywności odsiarczania spalin w zależności od parametrów pracy skrubera strumieniowego. Zidentyfikowano dominującą rolę stosunku ciśnień w skruberze oraz wyznaczono jego krytyczną wartość progową. Na podstawie kompleksowej serii badań eksperymentalnych sformułowano uogólnioną korelację opisującą efektywność skrubera, stanowiącą krajowe odniesienie do doboru optymalnych warunków pracy układu skrubera.

Abstract. The chapter presents the outcomes of investigations carried out on a novel exhaust flue gas cleaning system employing jet-ejector technology, intended for 0.25 MW and 1.0 MW marine diesel engines. Preliminary development research have been carried out at the test unit of 40 kW power. The research included the construction and commissioning of dedicated test stands and the execution of emission measurements for a broad spectrum of operating states. A separate research task addressed the desulphurisation efficiency of exhaust gases in relation to the operating parameters of the jet scrubber. A dominant role of the scrubber pressure ratio was identified, along with the determination of its critical threshold value. Based on a comprehensive series of experimental tests, a generalised correlation was formulated to describe the scrubbing efficiency, providing a domestic reference for selecting optimal operating conditions of scrubber systems.

Słowa kluczowe: skruber strumienicowy, odsiarczanie gazów spalinowych, sprawność skrubera

Keywords: jet ejector scrubber, desulphurisation of flue gases, scrubbing efficiency.

Introduction

Marine diesel engines used on marine vessels are responsible for considerable emissions of airborne pollutants, adversely affecting both atmospheric conditions and marine ecosystems. Key emission components include sulphur oxides (SOx), nitrogen oxides (NOx), and particulate matter [1, 2, 3]. Consequently, emissions from large-scale maritime operations are now classified as a major and steadily intensifying environmental challenge.

In response to these concerns, since 2013 the International Maritime Organization (IMO) has mandated that ships carry Ship Energy Efficiency Management Plans (SEEMPs), outlining guidelines for improving onboard operational energy efficiency [4]. IMO projections require that all newly constructed vessels achieve a 30% enhancement in energy efficiency by 2025 compared to ships built in 2014 [5]. Despite these targets, heavy fuel oil (HFO) continued to dominate maritime energy use – constituting 79% of the sector's consumption in 2018. Parallel to these measures, rigorous fuel monitoring and reporting requirements have become part of the global emission reduction framework.

The regulatory milestone commonly known as "IMO 2020" significantly restricted sulphur content in marine fuels. Outside Emission Control Areas (ECAs), allowable sulphur levels were reduced from 3.5% to 0.50% (by mass), becoming enforceable under revised provisions of MARPOL Annex VI [6]. This step was expected to reduce sulphur dioxide (SO_2) emissions by up to 85%. Under the amended regulations, compliance may be achieved either by using low-sulphur fuel oils or by equipping vessels with exhaust gas cleaning systems. Fuel blending – mixing low- and high-sulphur fuels – remains an additional pathway to conformity.

A common compliance measure adopted by shipowners is the installation of exhaust gas cleaning units, broadly referred to as scrubbers.

IMO recognises scrubbers as an acceptable alternative to low-sulphur fuels. These systems are available in two principal variants: wet and dry [7]. Wet scrubbers exploit the solubility of SOx in water and operate in three configurations: open-loop (using seawater), closed-loop (using recirculated alkaline-enhanced fresh water), and hybrid systems capable of switching between both modes. Dry scrubbers use solid sorbents to bind sulphur oxides. Owing to their proven performance, wet systems remain the preferred technology for maritime installations.

Between 2012 and 2018, global maritime emissions rose from 977 to 1,076 million tonnes CO_2-equivalent – an increase of 9.6%. These figures encompass emissions from international, domestic, and fishing operations. During the same period, the share of maritime transport in global anthropogenic emissions grew from 2.76% to 2.89%. Long-term forecasts suggest that emissions may reach 130% of the 2008 level by 2050 (IMO, 2020). In parallel, SEEMP plans have been mandated since 2013 [14], and IMO benchmarks continue to push for improved vessel performance [5]. Despite these interventions, HFO remains the dominant fuel option for global shipping. The timeline of tightening sulphur limits is presented in Table 1.

TABLE 1. Time schedule of sulphur limit reductions in MARPOL Annex VI (2005)

	sulphur limits in marine fuel, %	
Year	**Inside ECA-SO_x**	**Outside ECA-SO_x**
2008	1.5	4.5
2010	1.0	4.5
2012	1.0	3.5
2015	0.1	3.5
2020	0.1	0.5
2025	0.1	0.5

A significant decline in SOx emissions causes not only environmental improvements but also to health benefits for populations living near ports and coastlines. Semi-dry flue-gas desulphurisation systems, which reduce SO_2 emissions while moderating water usage, comply well with Annex VI requirements and provide an alternative to low-sulphur fuels. The IMO introduced a comparative indicator – the sulphur fuel equivalent allowing emission evaluation based on a reference relationship:

$$ER = \frac{SO\left[ppm, dry\right]}{CO\left[\%v / v, dry\right]} \qquad (1)$$

The above formula is commonly applied for assessment of operation of the scrubbers in marine engines. There should be noted that basing on limits of sulphur content in marine fuel at the level of 0.1%, the limiting level of emission ratio is ER = 4.3 according to the actual MARPOL legislation measures.

While many shipowners resort to low-sulphur fuels, equipping vessels with cleaning systems or applying blending strategies remain equally valid options. Additives improving fuel properties, including lubrication, may also support compliance. Paper [15] provides a cost analysis indicating that the implementation of Annex VI poses significant financial challenges for the shipping sector, potentially increasing freight rates.

Scrubber systems remain one of the most frequently adopted mitigation strategies. Wet scrubbing systems are further divided into open, closed, and hybrid loops depending on the method of water utilisation [7]. Dry scrubbers, relying on solid sorbents, eliminate the need for liquids. Among these solutions, wet scrubbers dominate due to their established desulphurisation efficiency. However, the installation of such systems is often hindered by engineering constraints. The need for sufficient residence time between gas and liquid requires tall structural designs, causing difficulties in vessel integration – such as limited space, complex exhaust routing, and potential effects on vessel stability and centre of gravity. Retrofitting typically involves substantial modifications, high cost, and extended installation times. Consequently, the search for more compact and easier-to-implement technologies continues.

One such alternative is the two-phase jet scrubber using low-pressure liquid-gas ejectors proposed in [8].

The presented research provides experimental results obtained from a prototype jet scrubber developed for flue gas treatment in 40 kW, 0.25 MW, and 1 MW marine diesel engines. All measurements were conducted by an accredited external laboratory.

Technical solution of jet-ejector scrubbers

Traditional marine scrubbers are designed primarily for SOx reduction from ship exhaust streams generated by main propulsion engines, auxiliary power units, and sometimes marine boilers. However, these systems present substantial practical limitations. Their considerable height and diameter – necessary to ensure sufficient gas-liquid contact – complicates installation, particularly in relation to space constraints, exhaust routing, and vessel stability. Retrofitting often requires extensive modifications and entails high operational downtime. This motivates the search for more compact, modular, and simpler alternatives.

Among the promising options are low-pressure liquid-gas ejector scrubbers featuring two-phase flow operation, as demonstrated by Butrymowicz et al. [8]. A schematic representation of such a configuration is shown in Fig. 1. The schematic illustrates the main ejector components: the motive nozzle, suction chamber, and the mixing section, together with the static pressure distribution along the scrubber. The volumetric entrainment ratio χ, defined as the volume flow rate of entrained gas divided by the volume flow rate of the motive liquid, may reach several tens under certain operating conditions.

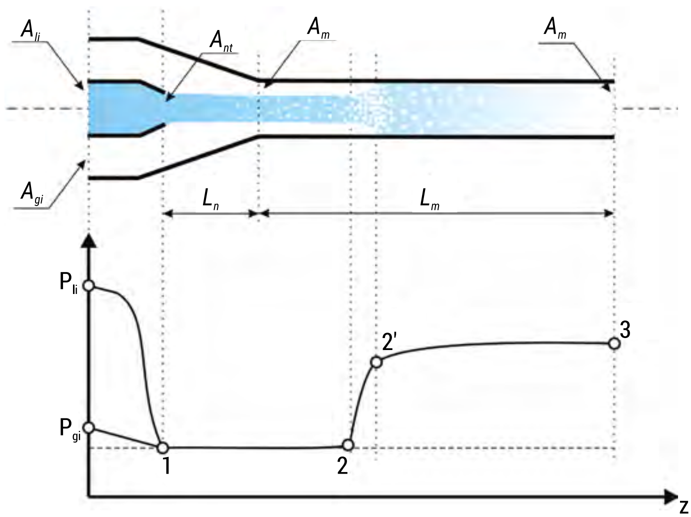

FIGURE 1. Schematic of liquid-gas ejector scrubber with static pressure profile along the scrubber

The motive liquid enters the ejector at pressure p_{li} through cross-section A_{li}. Inside the nozzle, the liquid accelerates and expands, discharging through A_{nt}. Flue gas is drawn into the suction chamber through area A_{gi}, entering the mixing chamber of cross-section A_m. At the mixing chamber inlet, an annular flow pattern normally forms. Further downstream, the liquid destabilises and breaks up, creating a liquid-gas foam region. Within this region, a mixing wave, analogous to a two-phase shock, develops, beyond which a quasi-uniform mixture flows at higher static pressure. Reverse mixture motion as foam flow pattern may appear in the initial part of the mixing chamber, forming recirculation zones that enhance momentum and mass transfer. The internal flow structure is complex due to the presence of the mixing shock wave and the evolving two-phase pattern. While this wave shares certain features with classical gas-dynamic shocks, such as rise in pressure and reduction in velocity, several differences exist. The process is essentially isothermal, slip velocity is present upstream, and the mixing wave has a finite spatial extent.

Although previous research has evaluated various ejector-based configurations, many are unsuitable for direct use in maritime systems [8]. Furthermore, the influence of geometric characteristics on jet-ejector scrubber hydrodynamics remains insufficiently studied. In particular, the length of the cylindrical mixing chamber – critical when shock-induced mixing occurs – has not been comprehensively discussed in the literature, where conical designs are more common.

Novelty of the paper is related with application of a two-phase ejector with cylindrical mixing chamber as a new type of exhaust gas cleaning device. Such application of jet scrubber for flue gas cleaning was proposed for the first time in paper [8]. Therefore, the first part of the researchfocused on the geometry of the scrubber and the determination of its required operating parameters. For this purpose, a model of a two-phase liquid-gas ejector was developed, and supplementary investigations were carried out in the field of hydrodynamics of a two-phase system using glass ejector. The aspects of the required geometry of the motive nozzle were considered. These studies focused on the identification of the flow structures with mixing shock wave that appears in the mixing section. The developed model of a two-phase liquid-gas ejector is beyond the scope of this paper and is not discussed there.

FIGURE 2. The CAD model of the tested jet-ejector scrubber for 40 kW engine

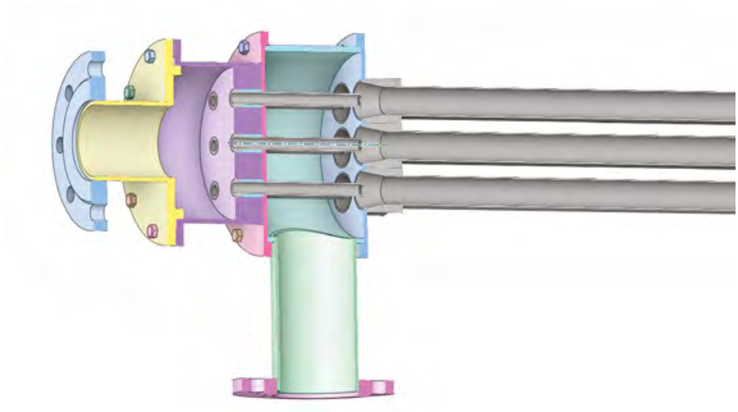

FIGURE 3. Cross-section of CAD model of the jet ejector scrubber designed for application for 250 kW diesel engine

Based on the results obtained from the experimental studies supported by modelling, a reactor dedicated for initial implementation in a 40 kW engine was proposed, see Fig. 2. The jetejector scrubber dedicated for the marine 250 kW unit is presented in Fig. 3. In the last case the proposed jet ejector scrubber has the form of a battery made up of nine sections consisting of the motive nozzle and the cylindrical mixing chamber. Three cases of the geometry of the tested jet ejector scrubbers were investigated with ratios of diameter of the liquid motive nozzle to diameter of the mixing chamber 0.067; 0.100, and 0.133. Sharp-edged orifice motive nozzles were applied for all of the individual scrubber section. The mixing section length to diameter ratio of 25 was applied.

Scrubbing Efficiency Assessment for 40 kW Unit

The laboratory testing stand (see Fig. 4) is located at Bialystok University of Technology. The testing stand is equipped with Lombardini LDW 2204 MG diesel engine of 40 kW maximum power. The feed pump is used to supply the jet reactor with sea water at designed pressure. The motive liquid stream parameters are determined using mass flow meter, pressure transducers, and temperature sensors. The mass flow rate of water supplied to the jet ejector scrubber is regulated by changing the rotational speed of the pump. In the tested jet ejector scrubber the motive stream entrains the exhaust gases. Mixing of the sea water with entrained gas occurs in the mixing chamber. Inside the jet ejector scrubber the sulphur compounds are absorbed by water mostly within mixing shock wave that is formed in the mixing chamber. Once the mixing process is completed, the two-phase mixture is directed to phase separator. The water stream leaving the jet reactor is directed outside the vessel while cleaned gas is released to the atmosphere. The testing stand was equipped with a recovery heat exchanger in which the exhaust gases optionally may be cooled. Motivation of the application of this heat exchanger comes from the potential application of discussed jet ejector scrubbers in flue gases exhaust system for heat recovery that covers the waste heat loop section. The potential condensation of water vapour from exhaust gas due to cooling process was also taken into consideration as it has significant effect on sulphur dioxide reduction process. Therefore, the experimental investigations were performed for the system in which the recovery heat exchanger was used as well as without using discussed heat exchanger. Mass flow rate of exhaust gas, its pressure and temperature at the inlet and outlet of the heat exchanger were measured. View of the laboratory testing stand is showed in Fig. 5.

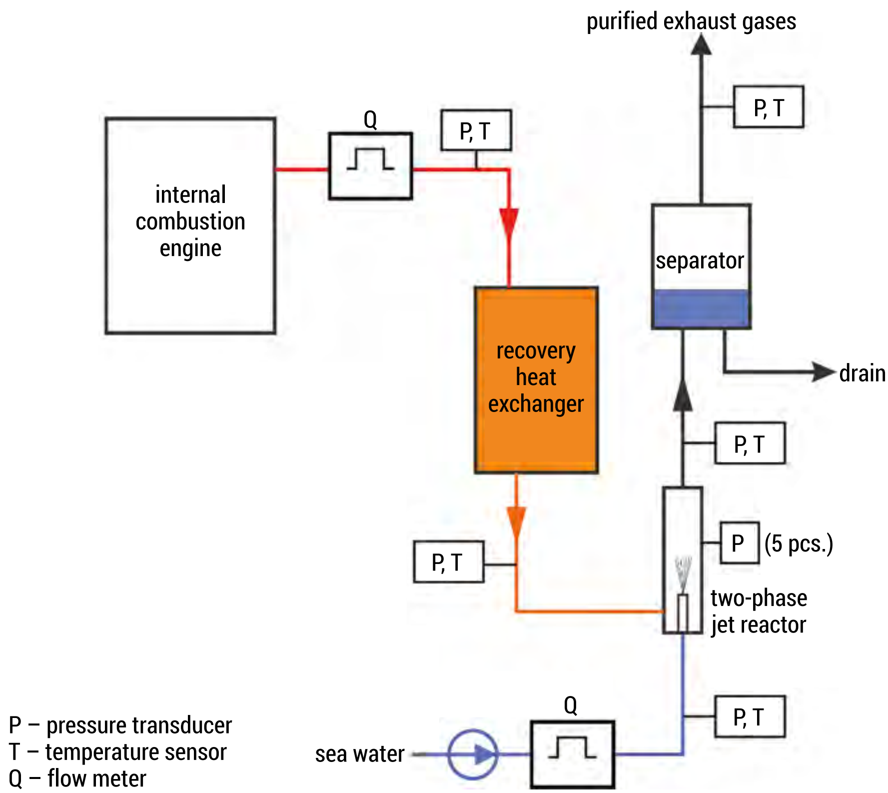

FIGURE 4. Schematic of laboratory testing stand for 40 kW engine equipped with the tested jet ejector scrubber; the measurement sensors locations are indicated

The measurement system based on National Instruments data acquisition system and LabVIEW software has been applied for the tested prototype system. In the test procedure, at least 100 readings (one reading per second) gathered at the steady-state conditions were taken and averaged to produce a single experimental point. Pressure and temperatures changes in the characteristic locations in the tested systems were observed and when no significant changes of pressure and temperature were observed, measured operation parameters were taken as the steady-state conditions.

Concerning the pressure transducers applied in the tests, their measurement accuracy was 0.25% of the full range. First-class K-type thermocouples were applied for the experiments. All of the thermocouples applied in the tested system were calibrated before the experimental investigations to achieve the total accuracy of temperature measurement ±0.2 K. Flow rate was measured with use of the Coriolis mass flow meters of the measurement accuracy 0.15% of the measured value. The flue gas composition was measured with use of AFRISO RGT-03 gas analyser, and the composition of cold flue gas emanating from the separator was measured with use of gas chromatograph INFICON 3000 Micro GC. Locations of the measurement transducers and sensors are shown in Fig. 4, the ranges of the measured parameters are presented in Table 2.

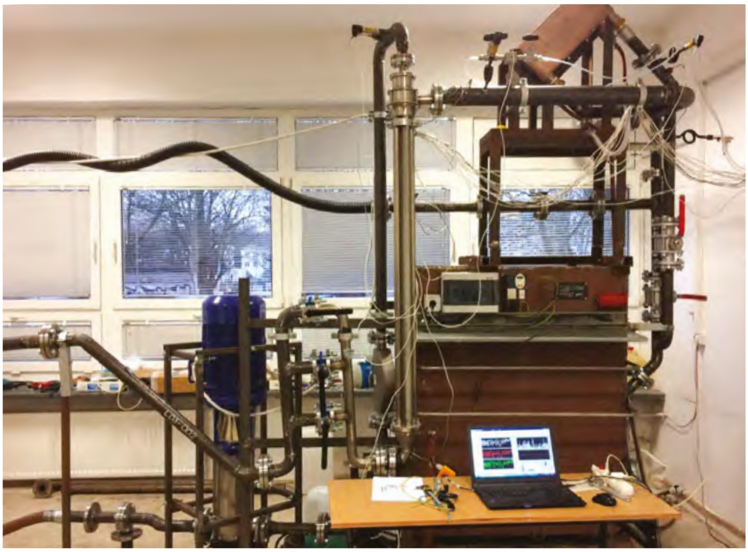

FIGURE 5. Photograph of the laboratory testing stand of 40 kW power

TABLE 2. Details of the measurement system components

Description	Range	Unit
exhaust gas flow rate	0–8.51	m^3/min
pressure of exhaust gas at the heat exchanger inlet	0–6	bar abs.
pressure of exhaust gas at the heat exchanger outlet	0–6	bar abs.
pressure of water at the scrubber inlet	0–16	bar abs.
pressure of water at the scrubber outlet	0–10	bar abs.
mass flow rate of water at the scrubber inlet	0–30	kg/h
temperature of exhaust gas at the heat exchanger inlet	0–500	°C
temperature of exhaust gas at the heat exchanger outlet	0–500	°C
temperature of water at the scrubber inlet	−10÷150	°C

Description	Range	Unit
temperature of water at the scrubber outlet	−10÷150	°C
pressure at various locations along the mixing section	0–6	bar abs.
rotational speed of the pump motor	0–100	%

TABLE 3. Operating parameters of the tested jet ejector scrubber for 40 kW marine unit

parameter	unit	without heat exchanger			with heat exchanger		
motive nozzle to mixing chamber diameter ratio	–	0.067	0.10	0.133	0.067	0.10	0.133
ea water mass flow rate	kg/h	2 874	9 113	11 994	3 307	9 341	12 034
motive pressure	MPa	1.53	1.451	1.453	1.512	1.502	1.457
outlet pressure	MPa	0.119	0.153	0.173	0.121	0.158	0.173
ea water temperature inlet	°C	21.9	11.5	9.2	21.9	18.4	13.8
ea water temperature outlet	°C	25.1	14.2	10.6	22.8	18.9	14.4
flue gas flow rate	Nm^3/min	1.78	1.51	1.49	1.43	1.22	1.19
flue gas pressure inlet	MPa	0.193	0.144	0.162	0.195	0.15	0.162
flue gas pressure outlet	MPa	0.118	0.146	0.161	0.119	0.15	0.161
flue gas temperature inlet	°C	203.7	227.6	224.9	230.7	206.8	220.5
flue gas temperature outlet	°C	152.3	173.5	167.7	34.4	33.2	36.6
entrained gas flow rate	Nm^3/min	0.08	0.5	0.74	0.06	0.45	0.66
pH of inlet water	–	7.98	7.98	7.84	8.01	7.91	7.92
pH of outlet water	–	7.75	7.12	7.83	7.01	6.84	6.86
flue gas inlet O_2	%	11.0	10.7	10.8	11.0	10.7	10.8
flue gas inlet CO/H_2	ppm	155	149	145	155	149	145
flue gas inlet CO	ppm	325	298	299	325	298	299
flue gas inlet CO_2	%	7.5	7.9	7.7	7.5	7.9	7.7
flue gas inlet NO	ppm	545	545	541	545	545	541
flue gas inlet NOx	ppm	562	559	557	562	559	557
SO_2 at the scrubber inlet	ppm	46.3	40	44	46.3	40	44
SO_2 at the scrubber outlet	ppm	0	0	0	0	0	0

The chemical composition of water used in the jet scrubber and the chemical composition of the condensate that condenses from the flue gas were performed. The exhaust gas composition was measured with a dedicated exhaust gas analyzer AFRISO RGT-03 and INFICON 3000 Micro GC gas chromatograph. The main parameters such as pressure, temperature, and mass flow rates as well as the composition of exhaust gas and sludge water were measured for the tested scrubbers for three types of sulphurised fuel supplied by Marine Projects Ltd. shipyards with mass sulphur content of 0.35%. The operating parameters of the tested jet ejector scrubbers are presented in Table 3. The provided results confirmed effective operation of the tested jet scrubber device and total reduction of sulphur dioxide content.

It should be noted that exhaust systems without after treatment process do not usually have a system for filtering particulate pollutants from the exhaust gas and particulates, especially TOC. New regulations on exhaust gases including particulates are expected to be introduced in the coming years. In addition to cleaning of sulphur compounds without additional filters, the system tested affects the amount of TOC extracted from the flue gas. The highest quantitative reduction was found for TOC (total organic carbon in the dust phase) with reduction result 46.2%. In the dust phase, TOC appears as unburned fuel in the form of soot. The exhaust gas cleaning system significantly reduces the emission of metals that are introduced with the fuel into the engine.

Scrubbing Efficiency Assessment for 0.25 MW Unit

The diagram presented in Fig. 6 illustrates the principal process loops and instrumentation installed on a 0.25 MW marine diesel engine test stand [16]. The seawater-cooled engine drives an electric generator whose output is absorbed by controllable electrical heaters. Exhaust gas can be directed either to the atmosphere or through the jet scrubber. The motive seawater is supplied by a dedicated pump.

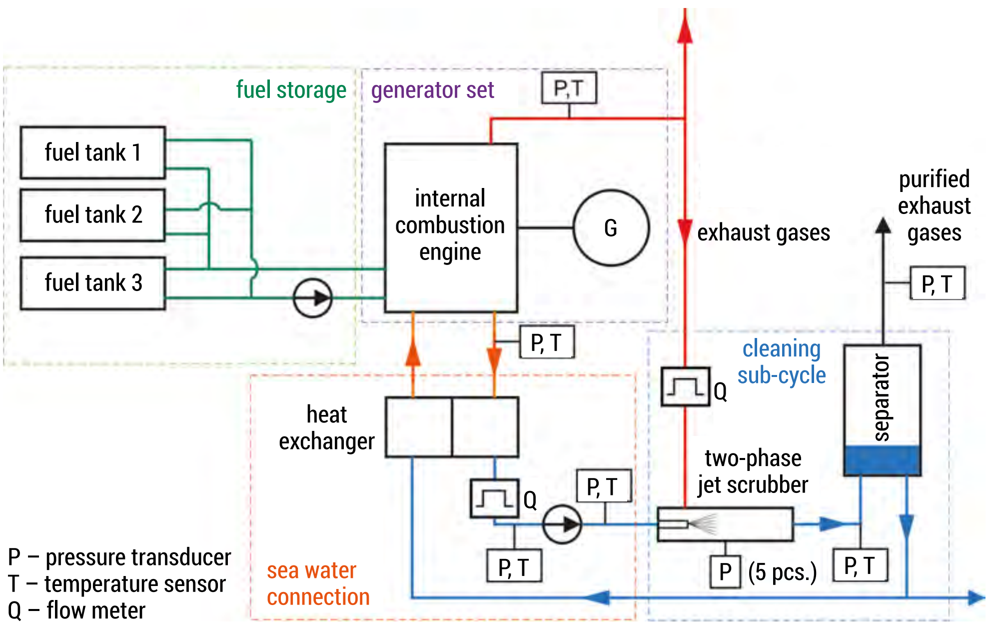

FIGURE 6. Schematic of the marine testing stand of maximum power 250 kW

The two-phase discharge from the scrubber flows to a liquid-gas separator. Cleaned gas is vented overboard, while sludge water is removed separately. Sampling valves allow the analysis of the separated wastewater.

TABLE 4. Details of the measurement system components

Description	Range	Unit
exhaust gas flow rate	0–8.51	m^3/min
exhaust gas pressure	0–6 (inlet/outlet)	bar abs.
exhaust gas temperature	0–500 (inlet/outlet)	°C
water pressure	0–16 (inlet) 0–10 (outlet)	bar abs.
water flow rate	0–30	kg/h
water temperature	−10÷150 (inlet/outlet)	°C
rotational speed of the pump	0–100	%
pressure along ejector	0–6	bar abs.

The exhaust loop is equipped with flow meters, thermocouples, pressure sensors, and gas sampling ports upstream and downstream of the scrubber. The details of the measurement system components are provided in Table 4. The seawater loop includes analogous instrumentation. Data acquisition was performed with a National Instruments system using LabVIEW. Each steady-state test point averaged at least 100 consecutive one-second measurements. Pressure sensors offered ±0.25% full-scale accuracy, temperature was measured with K-type thermocouples (±0.2 K), and Coriolis meters (±0.15%) measured flow rates. Hot exhaust gas composition (CO, CO_2, NO_2, SO_2, O_2) was analysed by TESMO Ltd. using a SIEMENS ULTRAMAT 23 NDIR analyser under accredited procedures. Cold gas analysis was carried out with an INFICON 3000 Micro GC chromatograph.

The experimental research conditions as well as obtained results of the tested scrubbers operation are presented in Table 5. For all of the operation conditions motive water pressure 1.0 MPa has been applied in tests.

The sulphur dioxide emission reduction can be evaluated on the basis of emissions ratio (ER) assessment and was adopted as a measure of scrubber performance:

$$\eta_{ER} = 1 - \frac{ER}{ER_{ref}}, \tag{2}$$

where 'ref' denotes reference conditions without scrubbing of flue gases. The analysis is based on 1549 measurement points of the jet scrubber operations.

TABLE 5. Tests conditio s and results of tested scrubbers operation for 0.25 MW unit

gas	unit	idle operation		engine load 50 kW		engine load 100 kW		engine load 200 kW	
		reference value no cleaning	scrubber operation	reference value no cleaning	scrubber operation	reference value no cleaning	scrubber operation	reference value no cleaning	scrubber operation
		jet scrubber L/D=25, fuel type SON120 with sulphur content 1.0624%							
CO	ppm	495	507	368	379	543	548	1070	1057
NO_2	ppm	157	173	487	511	657	685	885	905
SO_2	ppm	72	0	187	0	334	0	309	0
O_2	%	17.8	17.6	13.7	13.3	10.1	9	6.4	6.2
CO_2	%	25	26	5.2	5.4	7.8	8.4	10.5	10.3
SO_2/CO_2	–	28.8	0	36.0	0	42.8	0	29.4	0
		jet scrubber L/D=125, fuel type SON120 with sulphur content 1.0624%							
CO	ppm	522	529	388	393	482	489	794	828
NO_2	ppm	153	191	462	495	653	691	901	919
SO_2	ppm	80	0	185	0	317	0	437	0
O_2	%	17.9	17.5	13.9	13.3	10.2	9.2	7.5	6.9
CO_2	%	24	26	5.1	5.4	7.7	8.3	9.6	9.8
SO_2/CO_2	–	33.2	0	36.3	0	41.0	0	45.3	0
		jet scrubber L/D=25, fuel type CON120 with sulphur content 1.4750%							
CO	ppm	647	618	407	429	475	619	>1100	>1100
NO_2	ppm	172	204	477	505	656	694	907	892
SO_2	ppm	169	0	320	0	490	0	701	2
O_2	%	17.1	17.0	14.0	13.4	10.2	9.2	6.5	5.7
CO_2	%	29	3.0	5.1	5.3	7.7	8.4	10.5	10.9
SO_2/CO_2	–	57.7	0	63.1	0	63.4	0	66.8	0.2

Fig. 2 provides with relationship of the experimental values of the desulphurisation efficiency, η_{ER}, as a function of the compression ratio produced by the jet scrubber, π_d. Back pressure was adopted as a parameter describing the changes of static pressure during scrubbing process:

$$\pi_d = \frac{p_t - p_a}{p_{gi} - p_a}, \tag{3}$$

where: p_a – pressure at the separator at the scrubber discharge line; p_t – outlet pressure from the scrubber mixing chamber; p_{gi} – exhaust flue gas pressure at the inlet to the scrubber suction chamber.

The obtained experimental results allow for development of correlation for desulphurisation efficiency given by equation:

$$\eta_{ER} = 1 - 0.000266 b^{-0.0611} \chi_n^{0.7922} \pi_n^{-0.3089} \pi_d^{-0.6239}, \quad (4)$$

where: b is the geometric module defined as ratio of the motive nozzle throat to the mixing chamber cross section surface areas, π_n is the ratio or pressure at motive nozzle outlet to the inlet pressure, and χ is volumetric entrainment ratio. The determination coefficient for the developed efficiency correlation is $R^2 = 0.909$.

The comparison between measured results and the proposed correlation presented in Fig. 7 indicates a strong agreement for $\pi d > 0.96$, where the efficiency remains close to 1.0. For lower compression ratios ($\pi_d \approx 0.92$), a noticeable spread of experimental data is observed, which suggests increased process variability in this range. The model captures the general trend but does not fully account for the dispersion of results. At $\pi_d \approx 0.90$, the efficiency of the scrubber operations in terms of the emission ratio decreases sharply. Therefore, the compression ratio $\pi d \approx 0.90$ is assessed as the limiting threshold for the jet scrubber operations.

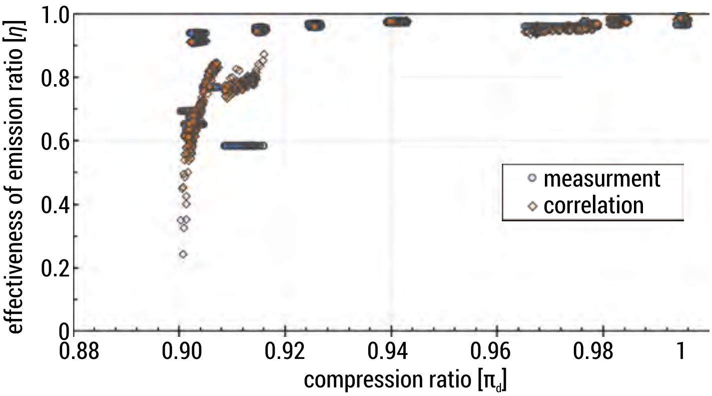

FIGURE 7. Relationship between scrubber efficiency η_{ER} and compression ratio π_d

The results indicate good overall agreement, with the correlation closely matching experimental values, particularly for η_{ER} above 0.90. The proposed relationship in eq. (4) is a basis for rational operation of the scrubbing system as limiting level according to the legislation measures is ER = 4.0, and in most of the cases of conventional marine scrubbers operation assumed level is app. ER = 2.5. Therefore, the provided relationship is a basis for rational usage of water flow rate and motive pressure in order to produce required emission ratio level for the jet scrubber.

Scrubbing Assessment for 1 MW Unit

Experiments for the 1 MW marine engine were conducted at the Marine Projects shipyard in Gdansk with multi-jet ejector scrubber presented in Fig. 8.

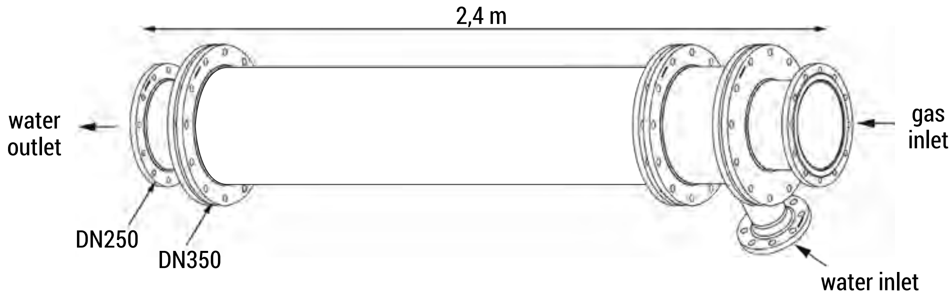

FIGURE 8. Geometry of the tested multi-jet scrubber applied for marine unit of 1 MW power

Tests covered the entire load range from idle to 1000 kW. Measurements of SO_2, NOx, O_2, CO_2, and particulate matter were performed using accredited reference methods. In the case of sulphur dioxide, concentrations decreased from over 2500 mg/m^3 to below 25 mg/m^3, yielding efficiencies above 99%.

The obtained data provide a foundation for refining the scrubber geometry and scaling the technology to larger propulsion systems. The study marks an important step towards widespread adoption of jet-ejector scrubbing as an alternative to conventional systems meeting MARPOL Annex VI requirements. Additional benefits included noticeable reductions in NOx emissions and particulate concentrations. The system demonstrated compactness, low energy demand, and operational simplicity.

The installation shown in Fig. 9 constitutes an integrated exhaust gas and water-treatment system for marine applications. It comprises of: a SCR reactor, a DPF filter, air compression units, heat exchangers, several process pumps, a water treatment section, sedimentation and circulation tanks, reagent storage, and sludge removal systems. The layout forms a closed loop ensuring the reduction of gaseous and particulate pollutants while simultaneously managing process wastewater.

Measurements – conducted by TESMO Ltd., accredited by the Polish Centre for Accreditation – included SO_2, NOx, O_2, CO_2 and PM concentrations upstream and downstream of the system at loads of 750 and 1000 kW as well as idle. PM measurements were performed with WHATMAN 19×90 glass-fibre filters, weighed before and after sampling. Measurement ports were installed following PN-EN 15259:2011 [9]. PM concentration was determined according to the Polish Regulation of 7 September 2021 [10] and PN-Z-04030-7:1994 [11]. Gaseous pollutants were recorded automatically under the standards PN-ISO 10396:2001 [12] and PN-EN 14789:2006 [13]. HORIBA PG 250 and PG 350 analysers, calibrated with reference gas mixtures (Air Liquide cylinders DH5L2, DLN1G), were used.

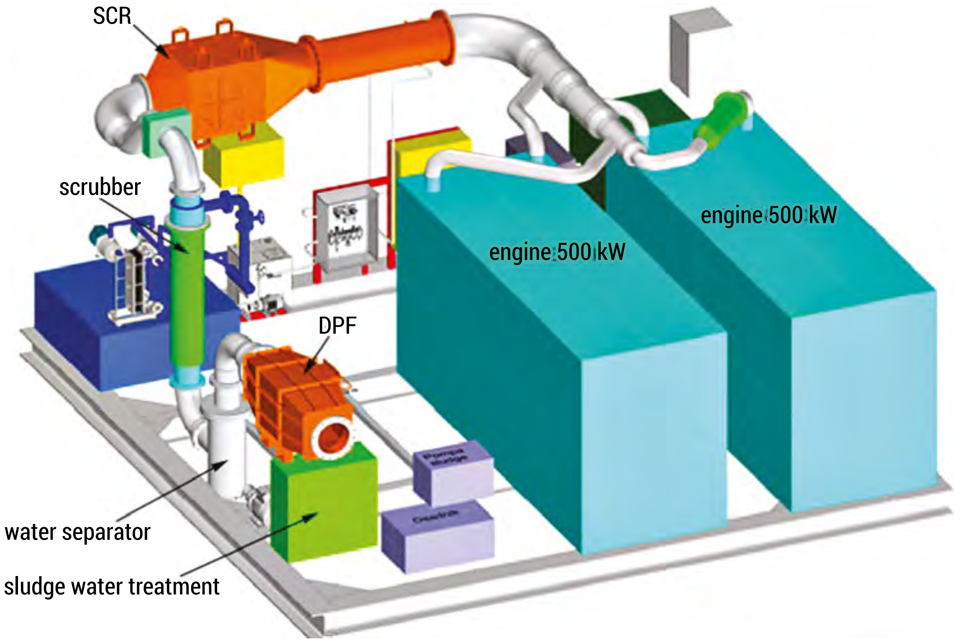

FIGURE 9. Schematic of tested flue gases cleaning system for 1.0 MW diesel engine unit

FIGURE 10. Photograph of the tested flue gases cleaning system fitted with multi-jet scrubber

Measurement uncertainties (expanded, k = 2) were:

- PM (gravimetric): ±11.1%,
- SO_2 (NDIR): ±3.41%,
- NOx (CLD): ±6.3%,
- O_2 (paramagnetic): ±3.6%,
- CO_2 (NDIR): ±3.8%.

Equipment used included:

- EMIOTEST 2598 dust meter,
- HORIBA PG-250A,
- HORIBA PG-350E,
- RADWAG AS 82/220.R2 scale.

TABLE 6. Results of measurements for 1.0 MW diesel engine for various fuel sulphur concentrations and various engine loads.

Exhaust gases at the inlet to system					Exhaust gases at the outlet of the system				
O_2	CO_2	SO_2	NO_x	PM	O_2	CO_2	SO_2	NO_x	PM
%	%	mg/m^3_U	mg/m^3_U	mg/m^3_U	%	%	mg/m^3_U	mg/m^3_U	mg/m^3_U
750 kW load									
8.13	10.27	6.30	1383	45.02	8.27	9.29	3.98	30.3	31.93
750 kW load									
9.82	8.96	1340.02	1075	40.86	9.90	7.92	15.84	28.4	28.58
1000 kW load									
7.90	10.42	2562.59	1976	–	7.92	9.45	22.97	6.7	–

The experimental research results for the 1 MW system are summarised in Table 6. DPF-based PM removal efficiency was assessed at the primary load of 750 kW. At 1000 kW, the emission ratio was ER = 0.91; at 750 kW, ER = 0.75. MARPOL imposes a limiting value of ER = 4.0, hence reductions were significantly greater than required. The pump feeding the jet scrubber consumed approximately 0.55% of engine rated power – comparable to conventional wet scrubbers.

Sludge water treatment

The presented paper provides validated results of an innovative approach for scrubbing process. However, another open issue that has been addressed in the research is the aspect of sludge water treatment process. In this case also an innovative approach has been proposed. This technology is based on utilisation of the partial vaporisation process using waste heat from marine diesel engine. Due to legislation measures and technical standards, the system operates under saturation temperature app. 80°C which requires pressure lower than atmospheric pressure.

The thermal treatment of sludge water significantly reduces the amount of sludge waste and improves the sludge water cleaning process. Evaporative unit applied in the system is shown in Fig. 11. Detailed investigations of the sludge water treatment process are out of the scope of the present paper.

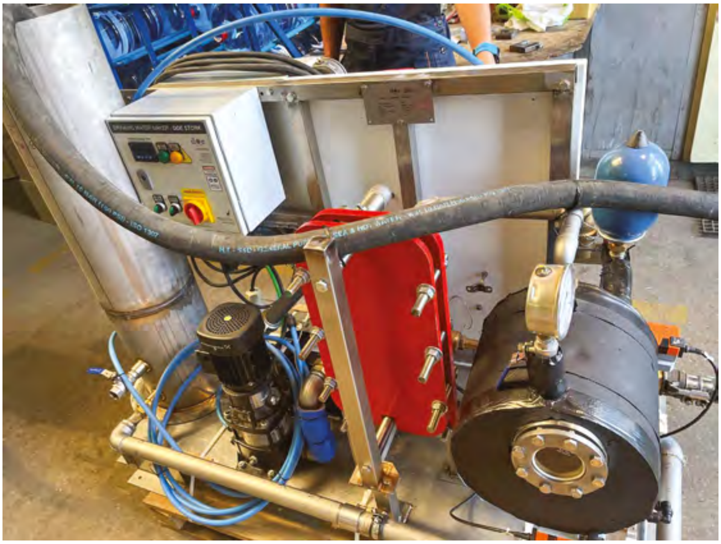

FIGURE 11. Photograph of an evaporative water treatment system for a 40 kW power plant at Marine Projects Ltd.

Conclusions

The investigations confirmed the high performance of the prototype jet scrubber for a 1 MW marine diesel engine. SO_2 levels dropped from above 2500 mg/m^3 to under 25 mg/m^3, corresponding to efficiency exceeding 99%. Noticeable reductions were also achieved for NOx and particulate matter. The system demonstrated low auxiliary power consumption – only 0.55% of engine output – and proved compact and operationally straightforward. A generalised empirical correlation was proposed to estimate emission ratio reduction as a function of principal operating parameters. Based on systematic testing, the limiting compression ratio for multi-jet scrubbers was established. The developed correlation enables rational operation of the scrubbing system with respect to energy use and emission-reduction targets.

Acknowledgement
The research results presented in the paper are supported by the National Centre of Research and Development, Contract No. POIR.04.01.04-00-0042/20-00. The authors would like to thank Tesmo Ltd. for providing a certified measurement system and for performing their evaluation tests and detailed analyses of the samples.

References

[1] Viana, M., Hammingh, P., Colette, A., Querol, X., Degraeuwe, B., de Vlieger, I., van Aardenne, J. (2014). Impact of maritime transport emissions on coastal air quality in Europe. *Atmospheric Environment*, *90*, 96–105. https://doi.org/10.1016/j.atmosenv.2014.03.046

[2] Xia, C., Wei, Z., Yongming, F., Tong, W., Yuanqing, Z., Majed, S., Xuefei, W., Weijian, Z. (2022). Investigation on Control Strategy Optimisation of Harsh Transient Condition for a Marine Natural Gas Engine. *Ships and Offshore Structures*, *18*(3), 1–14. https://doi.org/10.1080/17445302.2022.2116213

[3] Zhu, Y., Zhou, W., Xia, C., Hou, Q. (2022). Application and development of selective catalytic reduction technology for marine low-speed diesel engine: trade-off among high suplhur fuel, high thermal efficiency, and low pollution emission, *Atmosphere*, *13*(5), 731. https://doi.org/10.3390/atmos13050731

[4] Poulsen, R. T., Viktorelius, M., Varvne, H., Rasmussen, H. B., von Knorring, H. (2022). Energy efficiency in ship operations – Exploring voyage decisions and decision-makers. *Transportation Research Part D: Transport and Environment*, *102*, 103120. https://doi.org/10.1016/j.trd.2021.103120

[5] Smith, T. W. P., Jalkanen, J. P., Anderson, B. A., Corbett, J. J., Faber, J., Hanayama, S., O'Keeffe, E., Parker, S., Johansson, L., Aldous, L., Raucci, C., Traut, M., Ettinger, S., Nelissen, D., Lee, D. S., Ng, S., Agrawal, A., Winebrake, J. J., Hoen, M., Chesworth, S., Pandey, A. (2015). *Third IMO GHG Study 2014*. International Maritime Organization (IMO) London, UK, April 2015. https://imo.org.com

[6] US EPA. (2005). Protocol MARPOL 73/78 Anex VI – Regulation of Air pollution from ship, MARPOL Annex VI and the Act To Prevent Pollution From Ships (APPS).

[7] Zhao, J., Wei, Q., Bi, D., Liu, L., Wang, S., Ren, X. (2022). A brand new two-phase wet oxidation absorption system for the simultaneous removal of SO2 and NOX from simulated marine exhaust gas. *Chemosphere*, *307*(Pt. 2), 135830. https://doi.org/10.1016/j.chemosphere.2022.135830

[8] Butrymowicz, D., Gagan, J., Łukaszuk, M., Śmierciew, K., Pawluczuk, A., Kędzierski M., Zieliński T. (2021). Experimental validation of new approach for waste heat recovery from combustion engine for cooling and heating demands from combustion engine for maritime applications. *Journal of Cleaner Production*, *290*, 125206. https://doi.org/10.1016/j.jclepro.2020.125206

[9] PN-EN 15259:2011. (2011). Air quality. Measurements of emissions from stationary sources. Requirements for measurement sections and locations, measurement purpose and plan, and measurement report.

[10] Regulation. (2021). Regulation of the Minister of Climate and Environment of Poland of 7 September 2021 on requirements for conducting emission measurements. Polish Journal of Laws 2021, No. 1710.

[11] PN-Z-04030-7:1994. (1994). Measurement of dust concentration and mass flow in exhaust gases using the gravimetric method.
[12] PN-ISO 10396:2001. (2001). Stationary source emissions. Sampling for automatic measurement of gaseous component concentrations.
[13] PN-EN 14789:2006. (2006). Emissions from stationary sources. Determination of volumetric oxygen concentration. Reference method.
[14] Poulsen, R. T., Viktorelius, M., Varvne, H., Rasmussen, H. B., von Knorring, H. (2022). Energy efficiency in ship operations – Exploring voyage decisions and decision-makers. *Transportation Research Part D: Transport and Environment*, *102*, 103120. https://doi.org/10.1016/j.trd.2021.103120
[15] Notteboom, T., 2011. The impact of low sulphur fuel requirements in shipping on the competitiveness of Ro-Ro shipping in Northern Europe, WMU J Marit Affairs 10, 63–95.
[16] Gagan, J., Śmierciew, K., Łukaszuk, M., Pawluczuk, A., Butrymowicz, D., Kędzierski, M., Zieliński, T. (2023). Flue gas cleaning approach based on jet reactor prototype research. *Journal of Cleaner Production*, *418*, 138033.

DOI: 10.24427/978-83-68673-38-8_7

Chapter 7. Innovative technology of conversion of low-grade heat resources for cooling capacity of air-conditioning systems

Dariusz BUTRYMOWICZ[1], *Tadeusz ZIELIŃSKI*[2], *Jerzy GAGAN*[3], *Kamil ŚMIERCIEW*[4], *Michał ŁUKASZUK*[5], *Andrzej PAWLUCZUK*[6], *Mateusz PAWŁOWSKI*[7]

[1,3,4,5,6,7]*Bialystok University of Technology, Faculty of Mechanical Engineering*
[1]*e-mail: d.butrymowicz@pb.edu.pl, ORCID: 0000-0003-3869-8347;*
[2]*Klimor Ltd. Gdynia;*
[3]*e-mail: j.gagan@pb.edu.pl, ORCID: 0000-0002-7607-9654;*
[4]*e-mail: k.smierciew@pb.edu.pl, ORCID: 0000-0003-3869-8347'*
[5]*e-mail: m.lukaszuk@pb.edu.pl, ORCID: 0000-0002-8973-2405;*
[6]*e-mail: andrzej.pawluczuk@pb.edu.pl, ORCID: 0000-0003-3869-8347;*
[7]*e-mail: m.pawlowski@pb.edu.pl, ORCID: 0000-0003-3313-1261*

Streszczenie. Zrównoważony kierunek rozwoju technologii chłodniczej obejmuje łączenie agregatów strumieniowych zasilanych ciepłem z układami sprężarkowymi napędzanymi elektrycznie w celu efektywniejszego wykorzystania niskotemperaturowych źródeł ciepła. W pracy zostało przeanalizowane zastosowanie bezpiecznych dla środowiska czynników roboczych dla tych układów. Pomimo wyraźnego potencjału takich systemów ich praktyczne wdrażanie jest wciąż stosunkowo rzadkie. W niniejszym rozdziale przedstawiono eksperymentalną weryfikację innowacyjnej hybrydowej instalacji chłodniczej ze strumienicą parową i sprężarką o mocy 23 kW, pracującej w trybie hybrydowym, przeznaczonej do dostarczania wody lodowej o temperaturze 6/12°C do zastosowań klimatyzacyjnych. W zależności od warunków pracy instalacja może pracować w trybie zdominowanym przez podukład strumienicowy lub sprężarkowy, łagodząc znane ograniczenia strumienic przy podwyższonym ciśnieniu skraplania. Testy potwierdziły, że system stale zapewnia chłodzenie, osiągając współczynnik wydajności (COP) na poziomie 0.30 w trybie strumienicowym i średni COP 4,70 w trybie sprężarkowym. Przełączenie robocze – zdefiniowane jako punkt biwalentny – następuje przy temperaturze skraplania wynoszącej około 25°C. Przeprowadzona ocena energetyczna wskazuje na znaczne oszczędności energii podczas pracy w trybie strumienicowym, co dowodzi jego wysokiej efektywności w odpowiednich warunkach. Niniejsze badanie wypełnia lukę między koncepcjami teoretycznymi a praktycznymi rozwiązaniami, zapewniając eksperymentalną ocenę systemu hybrydowego. Uproszczona analiza ekonomiczna dodatkowo potwierdza praktyczność tego rozwiązania, gdyż oszacowano, że ciągła praca wymagałaby około 42 836 kWh energii elektrycznej rocznie. Podsumowując, wyniki dostarczają istotnych wskazówek inżynierom projektującym hybrydowe systemy chłodnicze, których celem jest zmniejszenie wpływu na środowisko przy jednoczesnym zapewnieniu szerokiego zakresu eksploatacyjnego.

Abstract. A sustainable direction in refrigeration technology involves coupling heat-powered ejector units with electrically driven compressors to exploit low-temperature heat sources more effectively. The aspects of environmentally safe working fluid selection have been analysed. Despite the clear potential of such systems, their practical deployment remains relatively rare. This paper reports the experimental verification of a 23 kW dual-mode hybrid vapour ejector–compressor refrigeration installation intended to supply chilled water at 6/12°C for HVAC applications. Depending on operating conditions, the setup can function either in ejector-dominated or compressor-dominated mode, mitigating the well-known constraints of ejectors at elevated condensation pressures. Tests confirmed that the system consistently delivers cooling, reaching a coefficient of performance (COP) of 0.30 in ejector operation and an average COP of 4.70 during compressor operation. The operational switch – defined as the bivalent point – appears at a condensation temperature of roughly 25°C. The performed energy assessment indicates notable energy savings when operating in ejector mode, demonstrating its high effectiveness under suitable conditions. This study narrows the gap between theoretical concepts and practical realization by providing an experimental assessment of the hybrid system. A simplified economic analysis further confirms the practicality of the solution, estimating that continuous operation would require about 42,836 kWh of electricity per year. Overall, the findings deliver essential guidance for engineers designing hybrid refrigeration systems aimed at lowering environmental impact while ensuring a wide operational range.

Słowa kluczowe: strumienica, czynniki o niskim wskaźniku GWP, hybrydowe układy chłodnicze, COP, efektywność energetyczna, praca biwalentna

Keywords: ejector, low-GWP refrigerant, hybrid refrigeration system, COP, energy efficiency, bivalent operation

Introduction

The worldwide shift toward more energy-conscious and environmentally responsible technologies has accelerated developments in refrigeration science. Conventional vapour compression units – although reliable and highly developed – rely on mechanical compression, making them electricity-intensive and environmentally burdensome [1]. These systems compress the refrigerant mechanically and remove heat through condensation, but this process comes at the cost of substantial electrical input and related greenhouse-gas consequences [2].

Ejector-based refrigeration, on the other hand, uses a high-pressure stream to entrain and compress a secondary low-pressure fluid. As they contain no moving components, ejectors represent durable and mechanically simple devices [3]. Their advantage becomes clear when low-temperature heat sources – such as waste heat – are available. Studies such as [4] discussed the integration of ejectors with other thermodynamic cycles in maritime energy systems, illustrating their compactness and efficiency. Shipboard air-conditioning applications were investigated in [5], showing meaningful reductions in operating costs and environmental impact. Solar-assisted ejector systems have also been demonstrated as effective [6]. As industrial processes often reject large amounts of thermal energy, they represent natural application areas for ejector-driven recovery solutions [7]. Numerical investigations of combined ejector-compressor setups have revealed their promise for improving system efficiency. Performance enhancements via compression-supported cycles were examined in [8], whereas in [9] solar-coupled configurations for urban cooling were explored. However, these contributions remain primarily numerical and typically do not verify their results through experiments. This work addresses this gap by experimentally analyzing separate ejector and compressor operation within a hybrid configuration to determine real-world working boundaries and evaluate achievable energy savings.

The performance of ejector-only systems is inherently sensitive to outdoor conditions, especially ambient temperature. As the condensation pressure increases, the cooling capacity drops significantly. Ejectors have therefore been studied extensively over the past decades [10]. Their geometry, thermodynamic behaviour, operating constraints, and refrigerant choices have all been explored through theory, simulations, and experiments. In [11], for example, a compound ejector cycle powered by both waste heat and solar energy was proposed, achieving notable COP improvements with low-GWP refrigerants such as R450A. In [12], ejector-compression concepts were adapted for vehicle cabin cooling using engine waste heat and low-GWP mediums like R1234yf, reporting substantial increases in COP and capacity. Similar efforts across many industrial branches confirm the potential of ejector technologies for reducing power consumption and operating expenses [13]. It was shown that solar-supported ejector units can enhance heat pump drying [14]. Adjustable-geometry ejectors [15] have demonstrated improved COP relative to fixed designs. In [16], solar installations with additional ejectors for expansion work recovery were assessed. In marine applications, a dual-loop ejector configuration for engine waste heat recovery was developed [17], improving fuel use and lowering CO_2 emissions. Flue-gas heat-powered air-conditioning systems for ships were assessed in [18]. In [19], a combined ejector–compressor solution for refrigerated ship compartments was introduced. Other researchers used ejectors to enhance hybrid or auxiliary systems: solar-powered ejector-desalination units were evaluated in [20]; ejectors were applied in [21] for battery temperature control with reduced compressor power; expansion-energy recovery ejectors in solar cycles were studied [16]; in [22] it was showed that multi-ejector systems in commercial refrigeration outperform parallel compression; in [23] ORC-supported refrigeration was improved with a multi-ejector control strategy; in [24] solar and air heat sources were combined in a dual-source heat pump with ejector enhancement.

The term “hybrid” encompasses a wide spectrum of system architectures, from CO_2 ejector-assisted booster arrangements to two-stage and expansion-energy-recovery configurations. Strong gains when merging a transcritical CO_2 cycle with an ejector were identified [25], especially with R32 as the refrigerant. In [26], refrigeration and power generation in a CO_2 ejector cycle were combined, improving energy efficiency through optimized back-pressure control. Two-stage ejector cycles were studied in [27]. Two-phase ejectors were reviewed in [28], confirming their useful role in cooling and heat pump systems. More complex cycles – such as cogeneration or cascade

– have also adopted ejectors. Efficiency improvements in cogeneration systems through ejector were demonstrated in [29]. ORC-supported ejector refrigeration in partial thermal storage conditions was evaluated in [30]. Solar ejector systems using R290 were optimized in [31]. Ejectors have also been explored directly as expansion-valve substitutes, improving overall cycle COP [22].

The innovative aspect of the system studied in this work lies in its ability to alternate between ejector-based and compressor-based operation depending on real-time condensation pressure and ambient conditions. The analogy to bivalent heat pumps is intentional: just as heat pumps rely on auxiliary heat sources under unfavourable weather, this hybrid unit supplements a heat-driven ejector with a mechanical compressor whenever condensation pressure becomes excessive. At low condensation temperatures, the ejector performs the vapour compression using only low-grade heat, reducing the load on the electrical compressor and improving overall efficiency. When outdoor temperatures rise and condensation pressure exceeds allowable limits, the compressor assumes full responsibility for maintaining cooling performance. This operational flexibility is particularly useful in environments with large temperature swings, where ejectors alone cannot manage peak loads.

The bivalent point – where system operation must switch from ejector to compressor – plays a central role in defining this strategy. In heat pumps, the bivalent point is the outdoor temperature at which auxiliary heating becomes necessary. Analogously, in the hybrid cycle studied here, the bivalent point corresponds to a condensation pressure beyond which the ejector can no longer deliver the required cooling. Past this threshold, compressor operation ensures uninterrupted air-conditioning performance.

From a fluid-dynamic perspective, the ejector may function in double-choked (on-design) or single-choked (off-design) regimes. Under double choking, the entrainment ratio remains constant despite variations in back-pressure. Once back-pressure surpasses a specific transition value, entrainment decreases. This transition pressure corresponds directly to the bivalent point. Designing an ejector with a higher entrainment ratio shifts the transition point to lower pressures, while lower entrainment ratios result in higher allowable back-pressures. The designer can select the optimal trade-off depending on local climate conditions. In the hybrid system, the ejector effectively reduces compressor energy consumption when conditions are favourable, while the compressor provides robustness when ejector operation becomes infeasible. To the authors' knowledge, such an approach has not been widely documented previously.

This research provides experimental results of the evaluation of a hybrid ejector–compressor refrigeration device capable of switching between two fully independent operating regimes. The ejector is intended for periods of low condensation pressure, whereas the compressor maintains operation at high condensation pressure. This capability allows for continuous air-conditioning performance without sacrificing efficiency. Prior publications have primarily focused on numerical simulations of multi-stage, cascade, or advanced absorption–ejector cycles. While useful, such analyses do not account for real-world limitations. In contrast, the present work confronts these practical challenges, including flow stability, mode switching, and the identification of the actual bivalent point. Despite overlapping terminology with previous studies, the experimental method, emphasis on practical operation, and dual-mode functionality distinguish this system sharply from earlier concepts. The results confirm the feasibility of integrating ejector and compressor functionalities into a single device and open pathways for future developments, such as advanced control strategies for dynamic mode switching.

Other thermally driven technologies (absorption, adsorption) cannot form bivalent systems of the type examined here. An ejector system uniquely allows for a seamlessly embedded compressor that can be activated as needed through a suitable control algorithm. This architecture ensures uninterrupted cooling delivery regardless of the state of the motive heat source, the district heating network, or off-design conditions in the heating loop. Under unfavourable ejector performance, the compressor cover ensures stable operation.

The hybrid configuration can be supplied by various heat sources depending on application. Three potential heat sources for the presented system include: (a) district heating networks, (b) solar thermal collectors, and (c) waste heat streams. Ejector refrigeration cycles involve three characteristic temperature levels. For typical use cases, the following temperature ranges are relevant: (a) motive heat: 55 to 120°C, (b) evaporation: 0 to16°C, (c) condensation: 20 to 40°C. A key advantage of ejector technology is its ability to operate on low-grade heat that cannot drive absorption or adsorption units. However, ejector performance is highly sensitive to condensation temperature, particularly at the lower end of motive-heat availability.

District heating typically offers the least favourable heat source conditions, especially during summer, with supply temperatures usually below 65°C due to recent EU regulations [32]. While some networks still operate at higher temperatures, ongoing modernization efforts aim at lowering them progressively. Although no strict physical constraints prevent using lower motive temperatures, energy efficiency inevitably decreases. Waste heat can vary widely but often exceeds 70°C. Solar-collector systems can reach temperatures above 120°C, though exceeding the refrigerant's critical temperature pushes the cycle into supercritical operation.

Standards such as [33, 34], and [35] establish expected chilled-water temperatures (6/12°C) for typical HVAC systems, implying evaporating temperatures of 0–3°C. For high-temperature cooling (14/17°C or 14/19°C), the evaporating temperature may be 8–10°C. Condensing temperatures are generally expected to fall between 20 and 40°C.

Although district heating represents the most challenging heat source, using its surplus capacity for summertime cooling is increasingly important in modern energy systems. For that reason, the present study focuses on operating conditions representative of district-heating temperatures. The experimental results presented later include performance curves enabling estimation of COP, cooling capacity, motive-heat consumption, and feasible working ranges.

To verify assumptions about the hybrid system's bivalent nature and performance boundaries, experiments were conducted on the developed test stand. Details of the research procedure are provided.

Working fluid selection for ejector refrigeration systems

The efficiency of an ejector depends on numerous factors, including inlet and outlet pressures and temperatures, thermo-physical properties of the working fluid, and the ejector geometry. A considerable body of numerical and experimental work has explored ejector performance under various working fluids and boundary conditions. Among these factors, fluid selection remains critical due to its strong influence on cycle efficiency. Equally important are the operating parameters of the cycle. Since ejector systems use thermal energy as the driving force, they are often compared with absorption units. In absorption cycles, the generator temperature $t_{(g)}$ typically exceeds 100°C. When the generator temperature decreases, cycle performance rapidly deteriorates due to diminishing concentration differences between the strong and weak solutions. As a result, vapour generation temperature $t_g < 80°C$ is generally considered the lower practical limit for absorption operation.

In contrast, most working fluids used in ejector systems do not require generator temperatures near 100°C, and there is no inherent physical barrier preventing ejector operation at much lower temperatures. Therefore, ejector cycles operating below $t_g < 80°C$ become especially attractive and, in this range, may compete effectively with absorption units [36]. For low-temperature heat sources, organic fluids offer clear advantages over water due to the significantly lower specific volume of their vapour, which becomes important in compact system designs.

Another aspect of fluid selection is the suitability of a refrigerant for a given ejector cycle configuration, which depends on the shape of its saturation dome and saturation pressure level. Most low-boiling fluids exhibit a "bell-shaped" saturation curve in the T–s diagram, with substances such as water or ammonia forming nearly symmetric liquid and vapour lines due to their high latent heat. However, several low-boiling synthetic refrigerants display highly asymmetric vapour saturation curves.

Based on the slope of the saturated vapour curve, refrigerants can be categorised as wet fluids (with a negatively sloped vapour saturation line); isentropic fluids (whose vapour saturation line is nearly vertical); and dry fluids, characterised by a positively sloped vapour saturation line. The most preferred selection for the ejector refrigeration systems are dry fluids.

The supersonic ejector performance with various working fluids has been widely investigated [37, 38]. Numerous theoretical and experimental studies have analysed the behaviour of ejectors operating with different refrigerants [39, 40, 41]. Literature findings consistently indicate that isobutane (R600a) is one of the most advantageous choices for ejector applications [37, 42]. Isobutane is inexpensive, well-characterised, and already used in many practical systems, with the primary drawback being its flammability and potential explosiveness. Therefore, safety considerations must be taken into account when designing ejector refrigeration systems using isobutane. The most critical precaution is minimising the total refrigerant charge, which substantially enhances safety without altering the fundamental operating characteristics. Proper system tightness and the use of safety valves compliant with EN 378 are also essential.

Current regulation concerning fluorinated refrigerants [43] effectively bans the use of new refrigerants with a GWP above 150 in most refrigeration applications. This significantly narrows the range of workable candidates for AC-R and heat-pump systems. Consequently, increasing attention is given to the new class of synthetic HFO refrigerants, particularly R1234, which has become available on the European market [44]. Since these fluids are still relatively unfamiliar, their key thermodynamic properties are compared here with well-known refrigerants of similar characteristics: isobutane (R600a), the discontinued HCFC R123, and the widely used R134a (see Fig. 1–3).

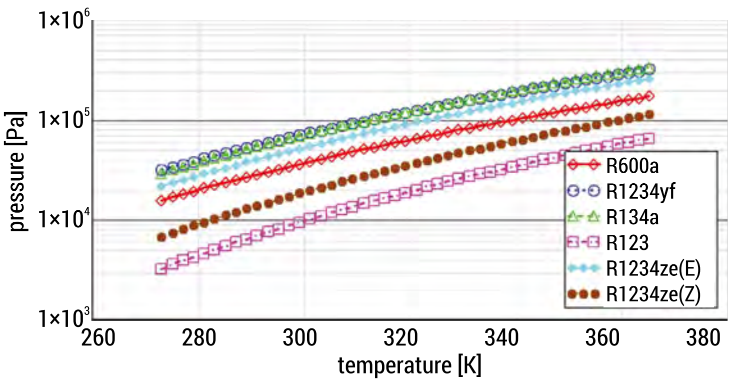

FIGURE 1. Saturation pressure versus temperature for selected environmentally friendly working fluids

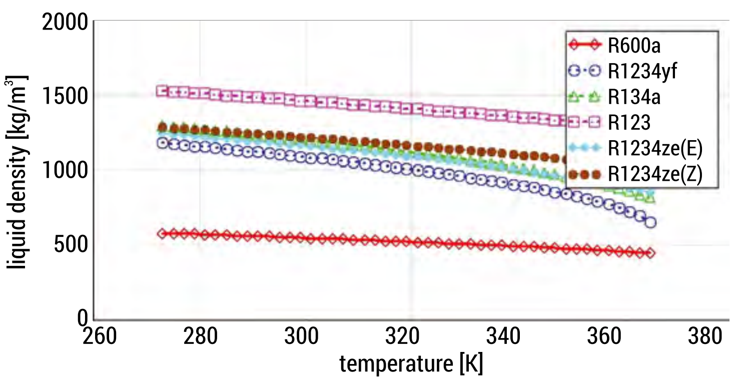

FIGURE 2. Liquid density versus temperature for selected environmentally friendly working fluids

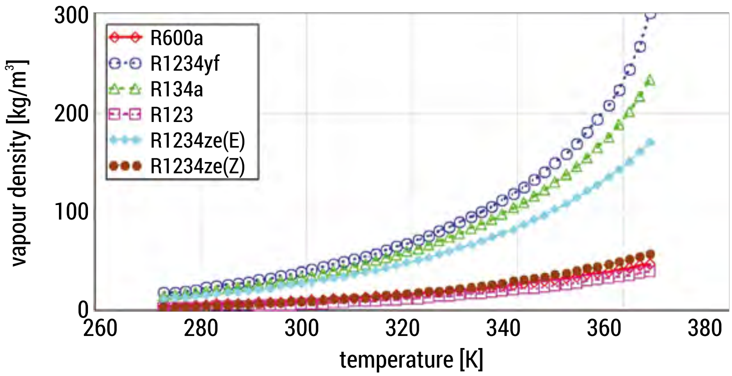

FIGURE 3. Vapour density vs temperature for selected environmentally friendly working fluids

Analysis of the presented diagrams leads to the following observations:

- All examined fluids show similar saturation-curve shapes, particularly on the vapour side, meaning they all behave as "dry" refrigerants in ejector applications.
- Saturation pressures of R1234ze(Z) and R123 are lower than those of R600a; in turn, R600a exhibits lower saturation pressures than R1234ze(E), R1234yf, and R134a.
- Liquid density is lowest for isobutane and highest for R123; refrigerants from the R1234 family display liquid densities comparable to each other and close to R134a.
- Vapour densities rise with temperature for all fluids, but the magnitude of this change separates them into two groups: R1234yf and R134a show the largest increase, while R123, R1234ze(Z), and R600a display much smaller variations. R1234ze(E) falls between these two extremes.

The outcomes of the numerical analysis for the selected refrigerants are presented in the figures that follow. The examined set includes both synthetic fluids (R-123, R-134a, and the R-1234 family) and a natural refrigerant (isobutane). It also spans representatives of "dry" fluids (isobutane, R-123, R-1234 types) as well as one "wet" refrigerant (R-134a). It should be emphasized that R-123 is an HCFC, and its use in newly installed systems is prohibited in the United States, the European Union, and numerous other countries. For the remaining fluids, no dedicated restrictions exist beyond the general limitations on HFC emissions defined in the European F-Gas Regulation [43].

Analysis of the results indicates that, across a broad spectrum of operating conditions, all investigated refrigerants provide comparable cycle efficiencies. Each of them can therefore be regarded as an attractive candidate relative to other fluids commonly referenced in the literature. It is worth noting that ejector-cycle performance data for R-1234 refrigerants have not yet been reported in published studies. Based on the characteristics illustrated in Fig. 1–3 and Fig. 4 and Fig. 5, refrigerant R-123 would appear to be the most favourable option, as it ensures similar cycle performance while operating at reduced pressures and lower vapour densities. Nonetheless, R-123 cannot be treated as a viable choice because of its non-zero ODP (ODP > 0), which led to its phase-out.

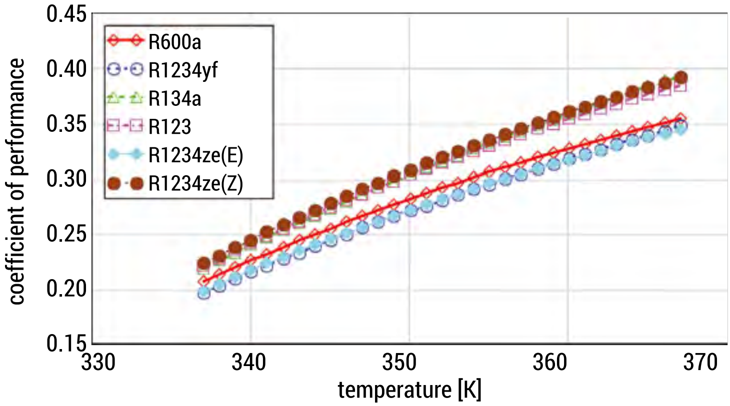

FIGURE 4. COP versus vapour generation temperature for evaporation temperature T_e = 278 K and condensation temperature T_c = 301 K

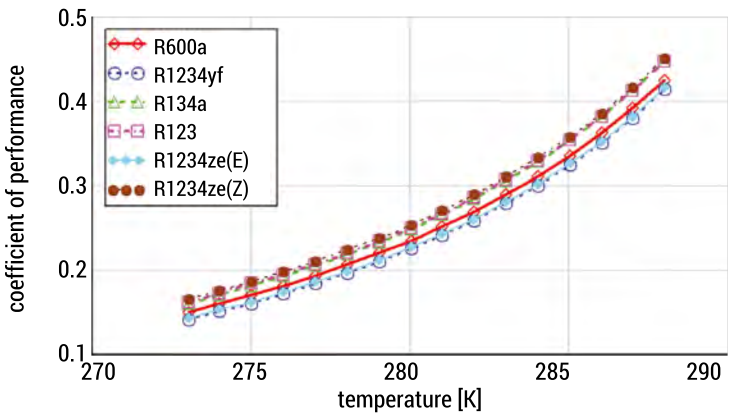

FIGURE 5. COP versus evaporation temperature for vapour generation temperature T_g = 333 K and condensation temperature T_c = 301 K

Refrigerant R-134a is also being discontinued due to its high GWP of 1400. The closest drop-in successor is R-1234yf, already implemented in automotive air-conditioning systems, although it is mildly flammable. Previous work by the authors demonstrated that isobutane can operate effectively in ejector refrigeration systems. Its primary advantage is that it is a natural refrigerant with negligible environmental impact, and for systems with very small refrigerant charges – similar to household refrigerators widely used across Europe – its flammability presents no significant hazard. In contrast, for larger-capacity installations, the explosive nature of isobutane may raise safety concerns.

The above discussed limitations motivated the search for another low-GWP refrigerant appropriate for ejector-cycle applications. Based on the comparative results presented, R-1234ze(E) emerges as a promising synthetic alternative. It offers operating characteristics and achievable cooling capacities that are broadly comparable to those obtained with isobutane, making it a strong candidate for further development in ejector refrigeration systems.

Testing bench

The experimental campaign was performed on the setup presented in Fig. 6. Photographs of the hybrid refrigeration unit and the wind tunnel used during the tests are shown in Fig. 7. The working fluid throughout the tests was R1234ze(E), a refrigerant selected in the previous section of this paper and characterised by extremely low GWP and widely regarded in the European Union as an environmentally acceptable option [44]. The main elements of the installation included a vapour generator, condenser, evaporator, compressor, refrigerant pump, regenerative heat exchanger as well as throttling, regulating, and shut-off valves. The system layout was selected so that stable refrigeration operation could be maintained across the full spectrum of operating conditions, irrespective of variations in motive heat supply or ambient temperatures.

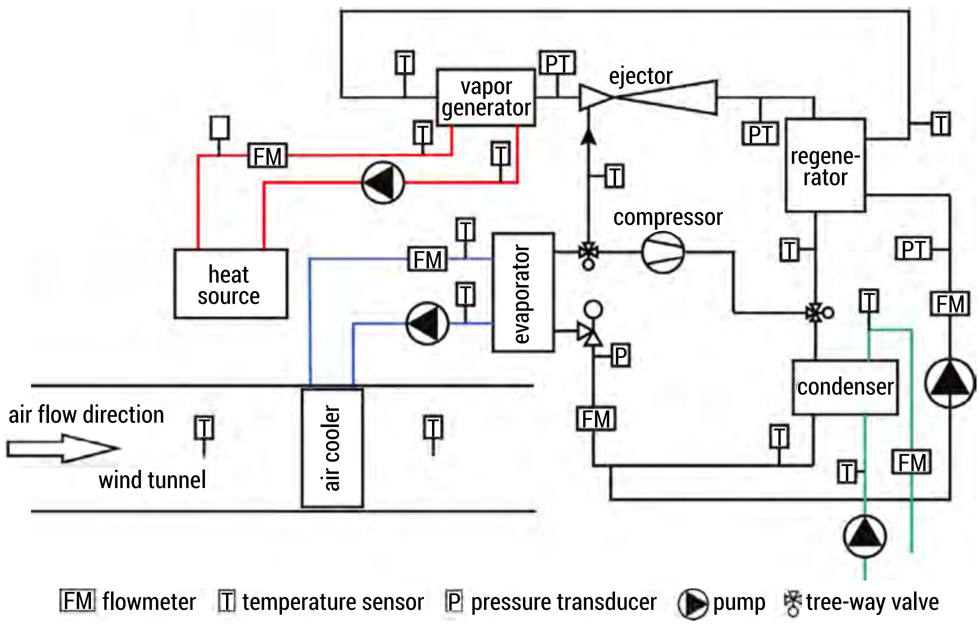

FIGURE 6. Schematic of the tested hybrid ejector-compressor refrigeration system

FIGURE 7. **Photo of the tested hybrid refrigeration unit**

When the unit operated in ejector mode, the thermal energy delivered by the heat source (e.g., district heating network) was supplied to the vapour generator, where the working fluid evaporated under elevated pressure. The resulting vapour – often superheated – was directed into the ejector, expanding through the motive nozzle to very low pressure and high velocity, typically reaching supersonic values. The pressure at the motive nozzle outlet remained below that in the evaporator, and the combined effect of this pressure difference and the high momentum of the motive stream caused vapour suction from the evaporator. Mixing and subsequent compression of the motive and entrained streams took place within the ejector body. At the ejector outlet, the medium was still a superheated vapour, enabling efficient heat transfer in the regenerator, where this excess heat was passed to the liquid entering the vapour generator. After the regenerator, the vapour entered the condenser and was liquefied. The condensed refrigerant was then divided: one fraction was routed through a circulation pump to the regenerator and subsequently to the vapour generator, while the remainder passed through the expansion valve to the evaporator. In compressor mode, the heat-supply loop and the ejector were disabled, and the installation worked as a conventional vapour-compression system.

The supersonic ejector was instrumented with paired temperature and pressure sensors located in the suction chamber, mixing chamber, and diffuser. The placement of RTD temperature sensors and pressure transducers is indicated in Fig. 6. The measurement accuracies were as follows: 0.25% for pressure transducers, 0.20% for RTD sensors, and 0.15% for Coriolis mass-flow meters. These values relate to the instrument readings and ensured precise monitoring of the thermal and flow parameters during operation. Measurement uncertainties were determined using the total derivative method. All sensors and measurement lines were calibrated prior to each test run. The data acquisition system continuously recorded all measurements, which were then stored on a PC. Only one flow meter was installed downstream of the ejector; the mass flow rate through the motive nozzle was evaluated using gas-dynamic relations, since under critical (choked) conditions the flow becomes dependent solely on upstream pressure and temperature. This method offers an accuracy of approximately ±1% [45] while also minimizing additional flow resistance. The accuracy parameters for the measurement equipment are summarized in Table 1.

TABLE 1. Accuracy of experimental equipment

Measurement Parameter	Sensor Type	Accuracy	Notes
Pressure	Pressure transducers	±0.25% of reading	Located in suction, mixing, and diffuser
Temperature	RTD sensors	±0.20% of reading	Calibrated before each run
Mass flow rate	Coriolis mass flow meters	±0.15% of reading	Single flow meter downstream of ejector
Electric power	Three-phase, Three-wire Active Power Transducer	±0.5% of reading	Compliant with EN 60688 and EN 61010-1 standards

Three auxiliary loops were integrated into the experimental rig: one for applying the thermal load to the evaporator, one for condenser cooling, and one delivering heat to the vapour generator. Each loop contained a PROMASS Coriolis meter

and temperature sensors installed at the inlet and outlet of the respective heat exchangers, enabling wide-ranging control of refrigerant flow rate and operating conditions. The evaporator load system used glycol as the heat-transfer medium, whereas water served as the working fluid in both the condenser cooling loop and the generator heating loop. The cooling loop was connected to both the evaporator and an air cooler positioned inside the wind tunnel. An automatically regulated dry cooler ensured stable condenser cooling, while the motive-heat loop incorporated a 100 kW electrically powered heater with automatic control. Control valves from CAREL and DANFOSS allowed fine adjustment of system parameters. A Hydra-Cell diaphragm pump driven by a 3 kW/700 RPM motor circulated the liquid refrigerant. The hybrid system used a Frascold Q7-28.1-AXH compressor. The generator, condenser, and evaporator were built using plate heat exchangers from SWEP and SECESPOL, and a regenerative plate heat exchanger was installed between the ejector outlet and the condenser. The wind tunnel was equipped with components enabling simulation of an air-handling unit; however, as most were not used for the purposes of this study, the diagram in Fig. 6 shows only the functional elements. Airflow rate and air temperatures (fresh and processed air) were also measured.

Results of Experimental Investigations

Two full experimental campaigns were executed, each consisting of a sequence of operating points. For every point, measurements were taken only after the system reached a steady thermal and flow regime – defined as fluctuations limited to the magnitude of inherent measurement noise rather than changes caused by the system approaching thermodynamic equilibrium. Once stability was confirmed, over one hundred data samples were recorded at 5-second intervals. These samples were subsequently averaged into a single representative data point. After adjusting the operating conditions, particularly by increasing the condensation pressure, the same procedure was repeated to obtain the next averaged point. This ensured a sufficiently robust dataset for evaluating the system performance. In ejector mode, each of the two measurement series contained six averaged points. The aggregated results are provided in Tables 2–4. An analogous methodology was applied in the compressor-mode investigations. These tests began at elevated condensation temperatures, where the ejector was no longer capable of delivering sufficient cooling performance. In this mode, run Series 1 yielded 10 averaged points, while Series 2 produced 8 points.

For run No. 1, the typical operating conditions were: $t_{g,sat}$ = 59.0°C, superheat Δt_g = 3–5 K, and $t_{e,sat}$ = –1.0°C. For run No. 2, the averaged values were: $t_{g,sat}$ = 57.5°C, superheat Δt_g = 7–9 K, and $t_{e,sat}$ = 3.0°C. In both campaigns, condensation temperature was treated as the primary variable. Temperatures of the heat-transfer fluids entering and exiting the heat exchangers are listed in Table 2), where HW and CW correspond to hot-water and chilled-water flows. These chilled-water values reflect the actual stable measurements obtained during controlled operation.

TABLE 2. Operation parameters for the tested ejector system

Heat carrier fluid (hot water)		Chilled water		Heat carrier fluid (hot water)		Chilled water	
t_{HWin}	t_{HWout}	t_{CWin}	t_{CWout}	t_{HWin}	t_{HWout}	t_{CWin}	t_{CWout}
°C	°C	°C	°C	°C	°C	°C	°C
run No.1				run No.2			
64.7	59.9	13.9	5.5	66.5	61.6	13.7	4.4
63.8	59.1	14.0	5.5	66.3	61.4	13.5	4.4
63.4	58.8	14.2	5.9	65.9	61.1	13.5	4.0
63.0	58.3	14.5	8.0	65.3	60.5	13.5	3.8
62.9	58.3	13.4	7.0	64.3	59.7	13.2	3.7
63.0	58.4	13.7	7.8	63.3	58.8	13.0	5.6

The necessary thermal and flow variables – including temperatures, pressures, and mass flow rates – were recorded and subsequently used to determine specific enthalpies and specific volume. These quantities served as inputs to the heat-flux calculations. The results are shown in Table 3 and Table 4. The symbol definitions for quantities used in the above tables are as follow: p_c – condensation pressure; Q_g – thermal heating load; Q_e – cooling capacity; W – power consumed by liquid pump; m_g – mass flow rate of primary (motive) fluid; m_e – mass flow rate of secondary (entrained) fluid; *U* – mass entrainment ratio; *COP* – Coefficient of Performance.

TABLE 3. Mean operating parameters for run No. 1.

p_c	Q_g	Q_e	*W*	m_g	m_e	*U*	*COP*	p_c	Q_e	*W*	*COP*
kPa	kW	kW	kW	kg/s	kg/s	–	–	kPa	kW	kW	-
Ejector mode								Compressor mode			
453.6	95.0	24.3	0.45	0.469	0.110	0.235	0.254	–	–	–	–
465.9	92.9	24.4	0.43	0.466	0.112	0.241	0.262	–	–	–	–
496.6	91.1	23.8	0.41	0.463	0.111	0.241	0.260	500.3	24.4	5.2	4.70
505.9	90.9	12.8	0.38	0.461	0.079	0.171	0.141	527.7	24.7	5.2	4.78
510.4	90.5	10.3	0.36	0.461	0.057	0.124	0.113	569.7	24.0	6.1	3.90
515.9	90.1	7.8	0.35	0.461	0.050	0.108	0.086	601.0	23.6	6.0	3.94
–	–	–	–	–	–	–	–	614.9	22.6	7.6	2.97
–	–	–	–	–	–	–	–	659.1	23.6	4.5	5.21
–	–	–	–	–	–	–	–	713.2	22.8	5.4	4.23
–	–	–	–	–	–	–	–	757.1	22.8	4.2	5,46
–	–	–	–	–	–	–	–	872.2	23.0	2.8	8.16
–	–	–	–	–	–	–	–	1005.6	21.2	5.7	3.75

TABLE 4. Mean operating parameters for run No. 2.

p_c	Q_g	Q_e	*W*	m_g	m_e	*U*	*COP*	p_c	Q_e	*W*	*COP*
kPa	kW	kW	kW	kg/s	kg/s	–	–	kPa	kW	kW	–
Ejector mode								Compressor mode			
456.7	96.1	26.3	0.41	0.443	0.143	0.324	0.272	–	–	–	–
473.5	95.6	25.4	0.40	0.441	0.146	0.330	0.265	–	–	–	–
484.4	94.4	25.1	0.39	0.445	0.136	0.307	0.265	–	–	–	–
496.8	93.0	22.6	0.38	0.448	0.113	0.252	0.242	–	–	–	–
502.6	91.1	17.9	0.37	0.450	0.096	0.214	0.196	503,9	24.4	2.3	10.53
518.6	89.3	10.8	0.36	0.459	0.067	0.146	0.121	555.8	23.7	4.3	5.57
–	–	–	–	–	–	–	–	578.3	23.8	2.8	8.50
–	–	–	–	–	–	–	–	616.3	23.3	2.5	9.36
–	–	–	–	–	–	–	–	667.2	22.5	2.7	8.31
–	–	–	–	–	–	–	–	729.8	25.8	2.4	9.64
–	–	–	–	–	–	–	–	871.3	21.9	3.4	6.38
–	–	–	–	–	–	–	–	1012.8	21.2	3.0	7.07

The experimental results demonstrate that the hybrid refrigeration system successfully utilized motive heat at temperatures slightly above 60°C to generate cooling. In ejector mode, approximately 25 kW of cooling output was produced using about 100 kW of heating power. Differences between heat-flux values on the hot and cold sides of the heat exchangers were within 9% for the generator, 13% for the evaporator, and 12% for the condenser. As expected, pump power consumption remained below 1% of the supplied heating capacity, confirming that the pumping power can legitimately be neglected when assessing the COP of the ejector cycle. Evaporator saturation temperatures of 0–2°C correspond to typical chilled-water air-conditioning conditions. All COP and cooling-capacity values reported in this study are based directly on controlled experimental measurements, ensuring their reliability.

Performance curves for both ejector and compressor modes are illustrated in Fig. 8 and Fig. 9. The initial objective was to determine the point at which the ejector transitions into off-design operation. The slope of this off-design segment is particularly important: a steep slope suggests a narrow stable operating window, whereas a gentler slope indicates a more forgiving ejector performance. This behaviour determines when the system should switch to compressor mode. The slope characteristics depend on working-fluid thermo-physical properties as well as the ejector geometry.

In both test series, the ejector exhibited strong sensitivity to variations in condensation pressure under off-design conditions, resulting in steep performance curves. Consequently, the compressor mode should be activated as soon as the entrainment ratio shows a declining trend. The observed relationships between condensation pressure and cooling capacity align with core thermodynamic principles, confirming the robustness of the test results. Compression-mode tests began when condenser pressure was slightly below the transition point, and the measurements were collected once this threshold was reached. The resulting curves clearly depict the operating domains of both ejector and compressor modes.

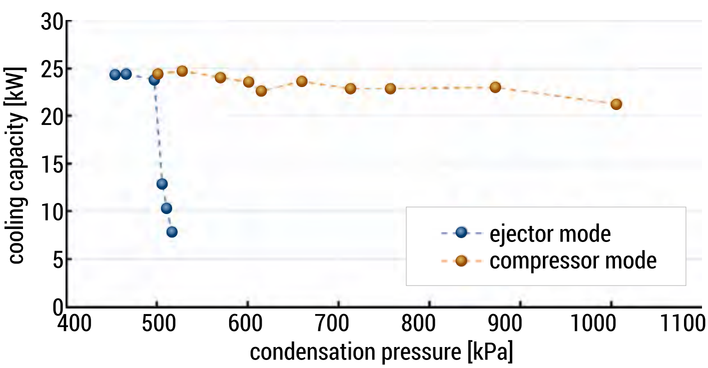

FIGURE 8. The tested hybrid ejector-compressor refrigeration system performance lines for ejector and compressor modes, run No. 1

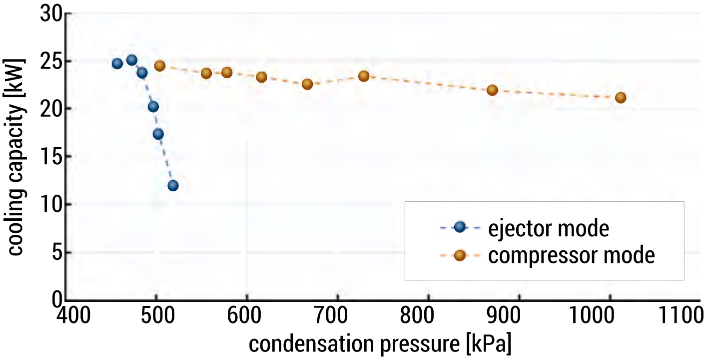

FIGURE 9. The tested hybrid ejector-compressor refrigeration system performance lines for ejector and compressor modes, run No. 2

The results highlight the contrasting characteristics of the two modes. For the ejector, cooling capacity rapidly declines once condensation pressure surpasses ~500 kPa, reflecting high sensitivity to increasing condensation temperature. Conversely, the compressor mode remains stable across a much broader pressure range, reliably delivering cooling even when the ejector becomes ineffective. This demonstrates that the hybrid concept effectively leverages the strengths of each mode, enabling efficient adaptation to variable thermal conditions.

The ejector operated in on-design mode until pc ≈ 500 kPa, beyond which the system entered off-design behaviour characterized by a noticeable reduction in cooling capacity. At pc = 500 kPa, both the ejector and compressor produced comparable cooling output, which is essential for seamless switching between modes without affecting user comfort. No additional system adjustments were required during mode transitions. Therefore, for the tested prototype, pc ≈ 500 kPa (corresponding to ~25°C condensation temperature) can be identified as the bivalence point under these conditions.

The ability to operate with low-temperature heat sources – such as district heating water – demonstrates strong applicability in moderate climates. The bivalence pressure serves as a guideline for designing hybrid systems and selecting optimal control strategies. Substantial energy-saving potential exists in regions where outdoor temperature remains below 25°C for most of the year. In Central Europe, annual mean temperatures of 7–10°C are typical, with only 20–50 days above 25°C. As a result, air-conditioning systems may operate in ejector mode for the vast majority of the year, which is particularly advantageous in facilities requiring 24/7 cooling (data centres, pharmaceutical production, electronics manufacturing, hospitals). It is important to emphasize that the presented validation tests were performed under the least favourable expected conditions: lowest motive-heat temperature and standard cooling loads with evaporator saturation of 0–2°C. Higher motive-heat temperatures or medium-temperature cooling applications would yield even higher efficiencies.

The additional test covered investigations of the system performance connected to a wind-tunnel test facility, enabling variation of the thermal load imposed on the air cooler by adjusting airflow rate. The results are summarized in Table 5.

TABLE 5. Results of operation of the bivalent hybrid system applied to the wind tunnel

	V_{Air}	t_{HWin}	t_{HWout}	t_{CWin}	t_{CWout}	$t_{g.sat}$	$t_{e.sat}$	$t_{c.sat}$	$t_{Air.in}$	$t_{Air.out}$	Q_e	Q_g	U	COP
	m³/h	°C	°C	°C	°C	°C	°C	°C	°C	°C	kW	kW		
E	2000	71.9	67.4	12.9	8.0	59.1	6.7	26.5	34.8	15.7	28.6	91.3	0.39	0.31
E	3000	71.5	67.2	12.5	8.1	59.6	6.5	26.8	33.8	16.4	27.9	84.8	0.36	0.33
C	3000	–	–	13.0	8.1	–	3.3	24.4	34.2	16.5	22.6	–	–=	7.00
E	3500	68.4	64.4	11.8	7.3	60.0	5.6	26.8	33.3	16.3	26.0	81.9	0.34	0.32

The airflow rate was regulated by adjusting the fan rotational speed, with tests performed at 2000, 3000, and 3500 m³/h. For nearly all conditions, the system operated in ejector mode (denoted as E in Table 5), except for the 3000 m³/h case, where compressor mode (C) was deliberately activated. The goal was to achieve conventional air-conditioning conditions, namely chilled-water temperatures of 6/12°C. Fresh-air temperature entering the tunnel ranged from 33–35°C. The system maintained evaporator saturation temperatures near 6°C. Chilled-water inlet temperature remained 12–13°C, with a typical 5 K temperature drop resulting in outlet temperatures near 8°C. Maintaining these conditions required generator saturation temperatures around 60°C and heating-water supply temperatures of approximately 70 ± 2°C. The outlet air temperature from the tunnel was around 16°C, which matches typical supply-air temperatures used in comfort-cooling systems. For indoor comfort levels of 22–23°C, supply air of 15–18°C is required. During these tests, condensation temperature was close to 26.5°C, corresponding to a saturation pressure of ~520 kPa.

In the ejector mode, cooling capacity ranged from 26–29 kW, with motive-heat input of 82–91 kW, yielding a COP of approximately 0.30. The recorded mass-entrainment ratios (0.34–0.39) are very favourable, indicating efficient ejector operation. Since generator saturation temperature matched earlier tests and evaporator saturation temperature was slightly higher – beneficial for ejector stability – the ejector likely operated close to its on-design regime.

In the compressor mode (C), stable operation was observed once evaporator temperature decreased from 6°C to 3°C, causing a roughly 4 kW reduction in cooling capacity. No noticeable changes in chilled-water or outlet-air temperatures were recorded.

Compared to earlier theoretical studies on hybrid systems, the present investigations provide with experimental validation under real operating conditions. While simulations have suggested strong potential for ejector-compressor systems, these results provide tangible evidence and highlight practical constraints – particularly the narrow operating range of ejectors at elevated condensation pressures.

Assessment of Energy Savings for Hybrid Operation

The use of the proposed hybrid system may offer meaningful reductions in energy consumption. A detailed analysis has been provided in [46]. This analysis is based solely on the experimental results and can be extended to wider operating ranges. The approach assumes continuous operation and considers only the electrical power demand of the compressor; auxiliary electrical demands (control systems, displays, fans, etc.) are neglected. It is assumed that the cooling capacity is 23 kW and the average COP in compressor mode is 4.70. If the compressor is needed only when outdoor temperature exceeds 25°C, which is assumed as 45 days per year (representative for Central Europe), then annual energy consumption is 5 281 kWh/a, and energy savings are 37 555 kWh/a. On this basis there could be assessed percentage savings of 87.8%.

These savings consider only the reduced electricity use of the compressor. Regarding investment costs, the hybrid system differs from a conventional vapour-compression system only by the addition of a vapour generator, an ejector, and a circulation pump. A modification using a two-phase ejector instead of a mechanical pump is also under development [47], although still at laboratory scale. Additional benefits stem from the ability to utilize waste heat or other low-grade heat sources.

The energy-savings analysis follows a continuous-operation scenario typical for applications such as data centres, where uninterrupted cooling is essential. Systems in the 25 kW cooling-capacity range are common in medium-scale facilities, including hospital operating rooms, pharmaceutical storage and manufacturing areas, food-processing facilities, and various industrial environments requiring stable thermal control.

This scenario illustrates the upper bound of annual savings while emphasizing the strong energy-efficiency potential of the hybrid concept. Although additional operational scenarios could be assessed, the continuous-load case demonstrates system performance under the most demanding conditions. The presented configuration is particularly well suited for applications utilizing low-grade heat sources (district heating, industrial waste heat). Although reversible heat pumps combined with PV systems are an alternative, their performance strongly depends on solar conditions. In contrast, ejector-driven systems deliver stable cooling when integrated with consistent thermal sources. The results clearly show the strong potential of the hybrid system in terms of energy efficiency and practical applicability across diverse climatic conditions. The main conclusions and future research directions follow below.

Conclusions

This study presents the first experimental confirmation of the operating performance of a bivalent hybrid ejector–compressor refrigeration system. The measurements show that the system achieved a COP of 0.30 in ejector mode and 4.70 in compressor mode. Under the conditions examined, the hybrid concept offers the potential for energy savings approaching 80%, making it an attractive option for continuous-duty applications such as industrial cooling, hospital environments, and data centres. From the experimental campaign, the following key conclusions can be formulated:

- Refrigerant R1234ze(E) has been selected as the most suitable for application in ejector and hybrid ejector-compressor refrigeration systems utilising low grade heat resources.
- A comprehensive series of laboratory experiments was completed, assessing the performance of a prototype bivalent hybrid ejector–compressor refrigeration system operating under temperature levels representative for typical air-conditioning systems.
- Despite the relatively low temperature of the motive heat source, the obtained results should be regarded as highly encouraging.
- For the first time, operating characteristics of this type of hybrid configuration have been experimentally established.
- The bivalent point for refrigerant R1234ze(E) was identified at approximately 500 kPa, corresponding to a condensation temperature of 25°C and motive-heat temperature near 65°C.

The findings presented in this paper offer a representative dataset describing the behaviour of a bivalent hybrid ejector–compressor system driven by low-grade heat sources relevant to air-conditioning applications, such as district heating networks. Although the experiments confirm key performance trends and highlight the system energy-saving potential, additional research is planned. Future work will extend the analysis to a broader spectrum of operating conditions, including other heat sources and alternative working parameters. These efforts aim to expand the current understanding of the hybrid system capabilities and strengthen the basis for its practical implementation.

Acknowledgement
The research results presented in the paper were financed by the Pomerania Development Agency Co., Contract No. RPPM.01.01.01-22-0041/17.

References

[1] Agathokleous, R., Bianchi, G., Panayiotou, G., Arestia, L., Argyrou, M. C., Georgiou, G. S., Tassou, S. A., Jouhara, H., Kalogirou, S. A., Florides, G. A., Christodoulides, P. (2019). Waste heat recovery in the EU industry and proposed new technologies. *Energy Procedia*, *161*, 489–496. https://doi.org/10.1016/j.egypro.2019.02.064

[2] Solanki, N., Arora, A., Singh, R. K. (2023). Performance enhancement and environmental analysis of vapour compression refrigeration system with dedicated mechanical subcooling. *International Journal of Air-Conditioning and Refrigeration*, *31*, 26. https://doi.org/10.1007/s44189-023-00042-8

[3] Rogdakis, E. D., Alexis, G. K. (2000). Design and parametric investigation of an ejector in an air-conditioning system. *Applied Thermal Engineering*, *20*(2), 213–226. https://doi.org/10.1016/S1359-4311(99)00013-7

[4] Braimakis, K., Karellas, S. (2024). Thermodynamic investigation of integrated organic Rankine cycle-ejector vapour compression cooling cycle waste heat recovery configurations for cooling, heating and power production. *Energy*, 304, 132020. https://doi.org/10.1016/j.energy.2024.132020

[5] Mastrullo, R., Mauro, A. W., Napoli, G., Viscito, L. (2024). Thermo-economic optimization and environmental analysis of a waste heat driven multi-ejector chiller for maritime applications. *Case Studies in Thermal Engineering*, *54*, 104081. https://doi.org/10.1016/j.csite.2024.10408

[6] Wang, X., Yan, Y., Li, B., Hao, X., Gao, N., Chen, G. (2020). Prospect of solar-driven ejector-compression hybrid refrigeration system with low GWP refrigerants in summer of Guangzhou and Beijing. *International Journal of Refrigeration*, *117*, 230–236. https://doi.org/10.1016/j.ijrefrig.2020.04.035

[7] Agathokleous, R., Bianchi, G., Panayiotou, G., Arestia, L., Argyrou, M. C., Georgiou, G. S., Tassou, S. A., Jouhara, H., Kalogirou, S. A., Florides, G. A., Christodoulides, P. (2019). Waste heat recovery in the EU industry and proposed new technologies. *Energy Procedia*, *161*, 489–496. https://doi.org/10.1016/j.egypro.2019.02.064

[8] Xu, Y., Jang, N., Han, X., Han, W., Mao, N., Chen, G. (2018). Performance evaluation and energy-saving potential comparison of a heat-powered novel compression-enhanced ejector refrigeration cycle with an economizer. *Applied Thermal Engineering*, *130*, 1568–1579. https://doi.org/10.1016/j.applthermaleng.2017.11.106

[9] Xu, Y., Shi, Q., Chen, N., Shen, X., Wang, C., Han, X. (2021). Seasonal energy performance evaluation with new perspective on partial-coupling ejection--compression solar cooling system for modern city buildings. *Energy Conversion and Management*, *233*, 113875.

[10] Besagni, G., Mereu, R., Inzoli, F. (2016). Ejector refrigeration: A comprehensive review. *Renewable and Sustainable Energy Reviews*, *53*, 373–407. https://doi.org/10.1016/j.rser.2015.08.059

[11] Al-Sayyab, A. K. S., Mota-Babiloni, A., Navarro-Esbrí, J. (2021). Novel compound waste heat-solar driven ejector-compression heat pump for simultaneous cooling and heating using environmentally friendly refrigerants. *Energy Conversion and Management*, *228*, 113703. https://doi.org/10.1016/j.enconman.2020.113703

[12] Suresh, R., Datta, S. P. (2022). Drop-in replacement of conventional automotive refrigeration system to hybrid-ejector system with environment-friendly refrigerants. *Energy Conversion and Management*, *266*, 115819.

[13] Ashrafi, O., Bashiri, H., Esmaeili, A., Sapoundjiev, H., Navarri, P. (2018). Ejector integration for the cost effective design of the Selexol™ process. *Energy*, *162*(C), 380–392. https://doi.org/10.1016/j.energy.2018.08.053

[14] Yu, M., Yu, J., (2022). Thermodynamic analyses of a solar assisted ejector enhanced vapour injection cycle with subcooler for heat pump dryer application. *Solar Energy*, *232*, 376–387. https://doi.org/10.1016/j.solener.2022.01.013

[15] Galindo, J., Dolz, V., Tiseira, A., Ponce-Mora, A. (2021). Numerical assessment of the dynamic behaviour of a solar-driven jet-ejector refrigeration system equipped with an adjustable jet-ejector. *International Journal of Refrigeration*, *121*, 168–182. https://doi.org/10.1016/j.ijrefrig.2020.10.019

[16] Yadav, V. K., Sarkar, S., Ghosh, P. (2022). Thermodynamic, economic and environmental analyses of novel solar-powered ejector refrigeration systems. *Energy Conversion and Management*, *264*, 115730. https://doi.org/10.1016/j.enconman.2022.115730

[17] Jiang, Y., Wang, Z., Ma, Y., Ji, Y., Cai, W., Han, F. (2022). Supercritical CO_2 Power Cycle and Ejector Refrigeration Cycle for Marine Dual Fuel Engine Efficiency Enhancement by Utilizing Exhaust Gas and Charge Air Heat. *Journal of Marine Science and Engineering*, *10*(10), 1404. https://doi.org/10.3390/jmse10101404

[18] Kędzierski, M., Śmierciew, K., Gagan, J., Butrymowicz, D. (2018). *Application Of Waste Low Heat As A Motive Source For Ejection Air-Conditiong Systems For Motor Yachts*. International Refrigeration and Air Conditioning Conference. Paper 2041.

[19] Shestopalov, K., Khliyeva, O., Ierin, V., Konstantinov, O., Khliiev, N., Neng, G., Kozminykh, M. (2024). Novel marine ejector-compression waste heat-driven refrigeration system: Technical possibilities and environmental advantages. *International Journal of Refrigeration*, *158*, 202–215. https://doi.org/10.1016/j.ijrefrig.2023.11.015

[20] Almahmoud, H. A., Al-Sulaiman, F. A., Ibrahim, N. I., Mansour, R. B., Alkhulaifi, Y. M. (2021). Energetic performance analysis of a solar-driven hybrid ejector cooling and humidification-dehumidification desalination system. *Energy*, *230*(C), 120849. https://doi.org/10.1016/j.energy.2021.120849

[21] Alkhulaifi, Y. M., Qasem, N. A. A., Zubair, S. M. (2022). Exergoeconomic assessment of the ejector-based battery thermal management system for electric and hybrid-electric vehicles. *Energy*, *245*, 123252. http://doi.org/10.2139/ssrn.3931676

[22] Haida, M., Banasiak, K., Smolka, J., Hafner, A., Eikevik, T. M. (2016). Experimental analysis of the R744 vapour compression rack equipped with the multi-ejector expansion work recovery module. *International Journal of Refrigeration*, *64*, 93–107. https://doi.org/10.1016/j.ijrefrig.2016.01.017

[23] Wu, J., Liang, Y., Sun, Z., Zhu, Y., Ye, J., Lu, J. (2024). Dynamic analysis and control strategy of ORC coupled ejector expansion refrigeration cycle driven by geothermal water. *Journal of Cleaner Production*, *445*, 141309. https://doi.org/10.1016/j.jclepro.2024.141309

[24] Li, S., Yang, H., Yuan, J., Zeng, X., Yang, Z., Lu, J. (2024). Thermodynamic and economic analyses of modified ejector enhanced solar-air composite dual-source

heat pump system in residential buildings. *Energy and Buildings*, *308*, 113978. https://doi.org/10.1016/j.enbuild.2024.11397

[25] Kumar, K., Kumar Gupta, H., Kumar, P. (2020). Analysis of a hybrid transcritical CO_2 vapour compression and vapour ejector refrigeration system. *Applied Thermal Engineering*, *181*, 115945. https://doi.org/10.1016/j.applthermaleng.2020.115945

[26] Ipakchi, O., Mosaffa, A. H., Garousi Farshi, L. (2019). Ejector based CO_2 transcritical combined cooling and power system utilizing waste heat recovery: a thermoeconomic assessment. *Energy Conversion and Management*, *186*, 462–472. https://doi.org/10.1016/j.enconman.2019.03.009

[27] Yang, D., Li, Y., Xie, J., Wang, J. (2022). Exergy destruction characteristics of a transcritical carbon dioxide two-stage compression/ejector refrigeration system for low-temperature cold storage. *Energy Reports*, *8*, 8546–8562. https://doi.org/10.1016/j.egyr.2022.06.066

[28] Sarkar, J. (2012). Ejector enhanced vapour compression refrigeration and heat pump systems – A review. *Renewable and Sustainable Energy Reviews*, *16*, 6647–6659. https://doi.org/10.1016/j.rser.2012.08.007

[29] Rooholamini, S., Ghorbani, B., Ebrahimi, A. (2021). Introducing a novel hybrid system for cogeneration of liquefied natural gas and hot water using ejector-compression cascade refrigeration system (energy, exergy, pinch and sensitivity analyses). *Applied Thermal Engineering*, *196*, 117283. https://doi.org/10.1016/j.applthermaleng.2021.117283

[30] Yaïci, W., Entchev, E., Longo, M. (2024). Organic Rankine cycle-ejector heat pump hybrid system using low GWP zeotropic mixtures for trigeneration application. *Energy Conversion and Management*, *299*, 117853. https://doi.org/10.1016/j.enconman.2023.117853

[31] Zarei, A., Elahi, S., Pahangeh, H. (2022). Design and analysis of a novel solar compression-ejector cooling system with eco-friendly refrigerants using hybrid photovoltaic thermal (PVT) collector. *Journal of Thermal Science And Engineering Progress*, *32*, 101311.

[32] European Commission. Directorate-General for Energy, District Heating and Cooling in the European Union. (2022). *Overview of Markets and Regulatory Frameworks under the Revised Renewable Energy Directive, Main Report*. Publications Office of the European Union.

[33] ASHRAE. (2014). *ASHRAE Handbook – Fundamentals*. ASHRAE American Society of Heating Refrigerating & Engineers.

[34] CIBSE. (2016). CIBSE Guide B: Heating, Ventilating, Air Conditioning and Refrigeration.

[35] EN 14511-2:2022/09 – Part 2: Test conditions. (2022).

[36] Butrymowicz, D., Śmierciew, K., Karwacki, J., Gagan, J. (2014). Experimental investigations of low-temperature driven ejection refrigeration cycle operating

with isobutane. *International Journal of Refrigeration*, *39*, 196–209. https://doi.org/10.1016/j.ijrefrig.2013.10.008

[37] Śmierciew, K., Gagan, J., Butrymowicz, D., Karwacki, J. (2014). Experimental investigations of solar driven ejector air-conditioning system. *Energy and Buildings*, *80*, 260–267. https://doi.org/10.1016/j.enbuild.2014.05.033

[38] Pridasawas, W. (2006). *Solar-driven refrigeration systems with focus on the ejector cycle* [Doctoral thesis].

[39] Yapici, R., Ersoy, H. K., Aktoprakoğlu, A., Halkaci, H. S., Yiğit, O. (2008). Experimental determination of the optimum performance of ejector refrigeration system depending on ejector area ratio. *International Journal of Refrigeration*, *31*(7), 1183–1189. https://doi.org/10.1016/j.ijrefrig.2008.02.010

[40] Selvaraju, A., Mani, A. (2004). Analysis of an ejector with environment friendly refrigerants. *Applied Thermal Engineering*, *24*(5–6), 827–838. https://doi.org/10.1016/j.applthermaleng.2003.08.016

[41] Huang, B. J., Chang, J. M., Petrenko, V. A., Zhuk, K. B. (1998). A solar ejector cooling system using refrigerant R141b. *Solar Energy*, *64*(4–6), 223–226. https://doi.org/10.1016/S0038-092X(98)00082-6

[42] Pridasawas, W., Lundqvist, P. (2007). A year-round dynamic simulation of a solar-driven ejector refrigeration system with iso-butane as a refrigerant. *International Journal of Refrigeration*, *30*(5), 840–850. https://doi.org/10.1016/j.ijrefrig.2006.11.012

[43] European Parliament, Council of the European Union. (2024). Regulation (EU) 2024/573 of the European Parliament and of the Council of 7 February 2024 on fluorinated greenhouse gases, amending Directive (EU) 2019/1937 and repealing Regulation (EU) No 517/2014.

[44] Honeywell International Inc. (2018). S*olstice® ze Refrigerant (HFO-1234ze (E))* [Brochure].

[45] Mastrowski, M., Smolka, J., Butrymowicz, D., Antczak, L., Gagan, J., Śmierciew, K. (2024). Experimental validation of the theoretical ejector model in a low-grade waste heat refrigeration system using R1233zdE as a working fluid. *Applied Thermal Engineering*, *236*, 121716.

[46] Gagan, J., Śmierciew, K., Pawluczuk, A., Łukaszuk, M., Dudar, A., Butrymowicz, D. (2025). The First Experimental Tests of Novel Bivalent Hybrid Ejector-Compressor Refrigeration System. *Energy*, *317*, 134646. https://doi.org/10.1016/j.energy.2025.134646

[47] Śmierciew, K., Pawluczuk, A., Gagan J., Butrymowicz, D. (2019). Thermodynamic analysis of two-phase injector for various working fluids. *Applied Thermal Engineering*, *157*, 113713. https://doi.org/10.1016/j.applthermaleng.2019.113713

DOI: 10.24427/978-83-68673-38-8_8

Chapter 8. Examination of the temperature dependence between the measuring points of the heat cost allocator

Leszek BARGŁOWSKI[1], *Mariusz ADAMSKI*[2]

Bialystok University of Technology,
Faculty of Civil Engineering and Environmental Sciences
[1]*ORCID: 0000-0002-4782-6155, e-mail: leszek.barglowski@sd.pb.edu.pl ,*
[2]*ORCID: 000-0002-1686-8301, e-mail: mariusz.adamski@pb.edu.pl*

Streszczenie. Przedstawiono budowę i zasadę działania elektrycznych podzielników kosztów ciepła. Skupiono się na poprawnej interpretacji temperatury sond pomiarowych podzielnika oraz odpowiadających im temperatur grzejnika i otoczenia. Przeprowadzono badania, a także opracowano własne analizy i wnioski w celu udoskonalenia metody obliczania ciepła oddanego z grzejnika.

Abstract. The structure and operating principle of electric heat cost allocators are presented. The focus is on correctly interpreting the temperature of the allocator temperature sensors, as well as the corresponding heater and ambient temperatures. Research was conducted and analyses and conclusions were developed to improve the method of calculating the heat emitted from the radiator.

Słowa kluczowe: podzielnik kosztów ciepła, czujnik temperatury, moc cieplna grzejnika, centralne ogrzewanie

Keywords: heat cost allocator, temperature sensor, thermal output of radiator, central heating

Introduction

Heat cost allocators with electrical power supply [1, 2] are used for establishing the heat consumption value of room heating radiators. This standard specifies that heat cost allocators shall not be used for heating systems where the temperature of the heating system falls below or exceeds the temperature limits of the heat cost allocators, where the rating factor for the thermal output, K_Q, cannot be clearly specified or where the heating surface is inaccessible. This applies usually to the following heating systems:

- floor heating,
- radiant ceiling heating,
- flap-controlled radiators,
- radiators with ventilators,

- fan-assisted air heaters,
- heating systems with steam-operated radiators.

Paper [3] presents the results of analyses of convection radiators from various manufacturers that can be used with cost allocators. The analyses focused on the volume, mass and length of the convection radiators, using the appropriate indicators Q_M, Q_V and Q_L. The papers [4, 5] present the evaluation criteria for heat cost allocator recordings based on the 2009 VDI 2077 guidelines, which align well with the realities of multi-family residential buildings for housing associations in eastern Poland. The purpose of article [6] is to provide a brief overview of the requirements set out in the PN EN 834 standard. It also provides the values of the EB coefficients necessary for analysing the accuracy of heat consumption recording. The standard defines the basic condition of the radiator, and the control diagrams should be constructed in such a way that the radiators on which the cost allocators are mounted release heat to the room in ambient conditions.

The temperatures supplied to the radiators in the flats were compared with the requirements for electronic heat cost allocators set out in PN-EN 834. Due to the requirements of electronic heat cost allocators, new design temperatures for central heating systems were proposed [7]. If cost allocators operate outside the baseline state, the readings of heat consumption are nonlinear. Paper [8] identified three cases of radiator operation. In the first case, the allocator registered too many heat units; in the third case, it failed to register the heat delivered to the room. The second case was unstable, meaning the allocator initially registered too much heat, but then failed to register the heat transferred by the radiator to the room when the flow through the radiator was minimally reduced. In work [9], the amount of heat Q_{obl} theoretical transferred by the radiator to the room was calculated using equation

$$Q_{obl} = Q_n \left(\frac{\Delta t}{\Delta t_{ln}} \right)^n dt \tag{1}$$

where Q_n – catalogue heater power [W], Δt_{ln} – logarithmic temperature difference according to the manufacturer's assumptions, for catalogue heater power of radiator, Δt – logarithmic temperature difference during measurements, $n = 1.33$ – coefficient characteristic for a given type of heater. The total power of the heater during the measurement was multiplied by the test time *dt* of individual periods (24 hours) and was expressed in kWh.

The value Q_{obl} was then compared with the values Q_r read from the cost allocator and with the values Q_{Wobl} determined using equation [8]

$$Q_{Wobl} = K \int \left(\frac{t_H - t_L}{60} \right)^{1.33} dt \tag{2}$$

where t_H – measured radiator surface temperature at the sensor location, t_L – ambient temperature, $K = K_Q K_C K_T$ – conversion factor [1].

The results of heat consumption analyses were conducted on a building [10], housing estate [11] and city scale [12].

This article aims to present the relationship between the measurement sites t_H, t_{HS}, t_{RS} and t_L (Fig. 1).

Electronic heating cost allocators

Electronic heating cost allocators are devices that account for the costs of central heating in multi-family buildings. They are used in calculations to allocate the overall heating costs to individual users of the premises, depending on their heat consumption. Mounted on radiators in apartments, they work by measuring the temperature difference between the radiator and the air in the room. As they are indicators rather than measures, their readings may be misinterpreted; however, they encourage heat conservation and enable fairer settlements. They do not measure thermal energy in physical units (GJ or kWh); they only indicate consumption units, which are used for heating cost accounting. Two temperature sensors ensure their operation, and heat consumption units are calculated based on the difference in their values.

One t_{HS} sensor measures the temperature of the heater t_H.

The second t_{RS} sensor measures the air temperature in the room t_L.

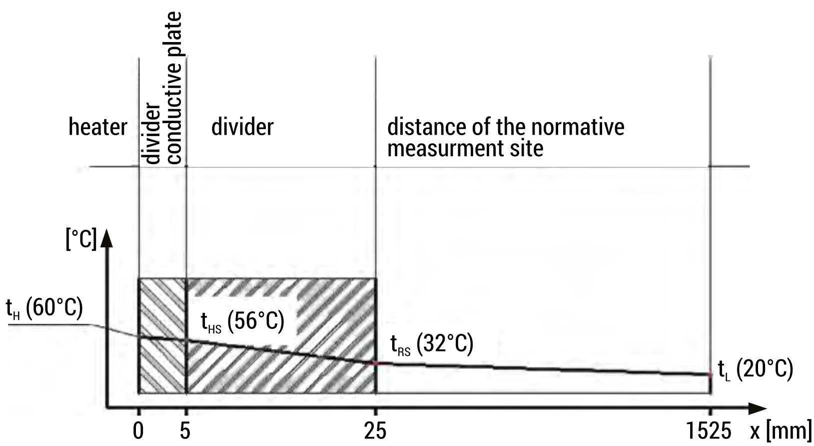

FIGURE 1. An example of a temperature drop between the heater (t_H), the divider sensors (t_{HS} and t_{RS}) and the ambient temperature (t_L)

Measurement stand

The test was performed on a heater with a power output of Q_n = 2310 W at an inflow temperature of 90°C and an outflow temperature of 70°C and a room temperature of 20°C. Fig. 2 below shows the diagram for mounting the measuring probes. In place of the original NTC thermistor sensors in the divider, temperature sensors have been installed that are connected to an electronic recorder which collects data in a text file.

The measurements were carried out in the actual operating conditions of the radiator.

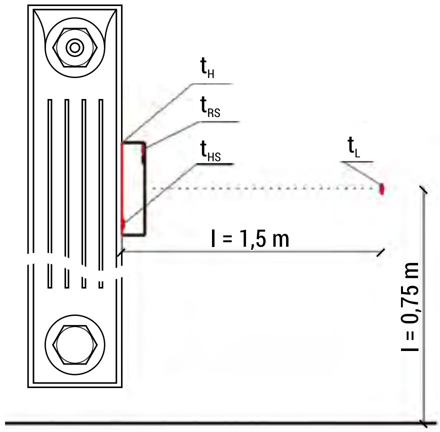

FIGURE 2. Diagram showing the arrangement of the tested measurement points

Measurement results

Fig. 3 shows the measurement data that has been analysed and archived. More than 34,000 measurement cycles were recorded.

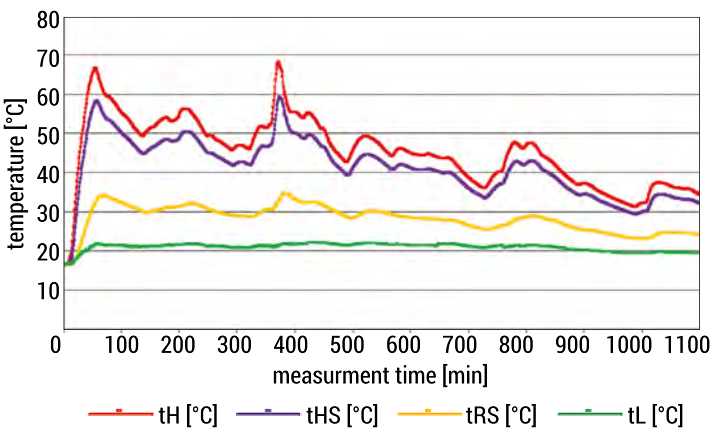

FIGURE 3. Graph showing the results of temperature measurements (t_H, t_{HS}, t_{RS} and t_L)

Analysis of measurement results

The analysis results are presented in Figs. 4 and 5.

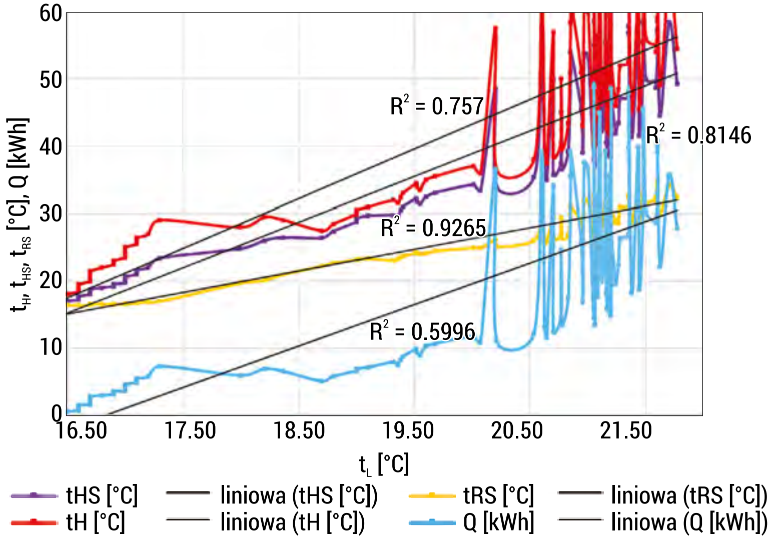

FIGURE 4. Data obtained versus room temperature t_L

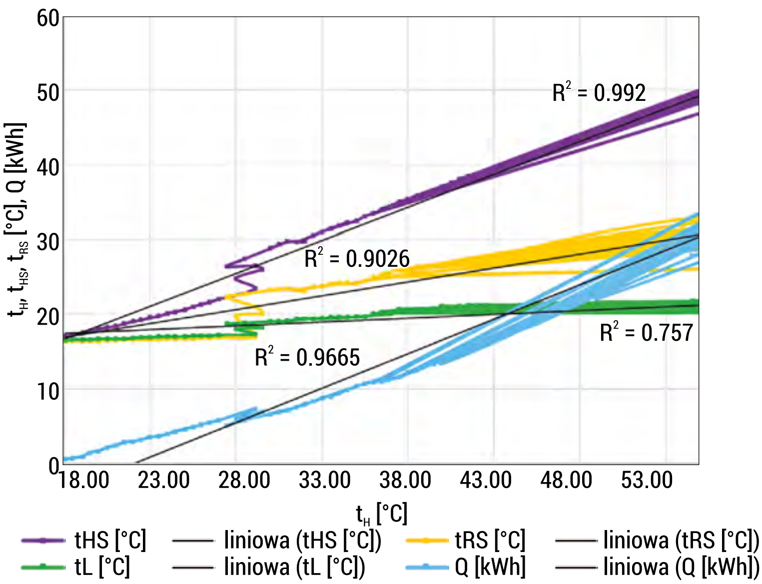

FIGURE 5. Data obtained versus radiator temperature at the location of the allocator t_H

Room temperatures t_L (Fig. 4) fluctuate around 20°C. Temperatures below 18°C are not included in the definition of the radiator's normal operating conditions. Such temperatures may occur in unoccupied rooms. Significant temperature fluctuations are possible for room temperatures above 20°C.

The graph (Fig. 5) shows that the measured temperatures versus the radiator temperature at the allocator location t_H vary linearly, and the actual values of temperatures (t_{HS}, t_{RS} and t_L) can be approximated quite well by linear functions. The correlation coefficient R between the presented data and the temperature t_H is as follows:
$t_H \rightarrow t_{HS} = 0.996$,
$t_H \rightarrow t_{RS} = 0.950$,
$t_H \rightarrow t_L = 0.870$,
$t_H \rightarrow Q$ [kWh] = 0.983.

Conclusions

The above study examined the relationship between the temperatures t_H, t_{HS}, t_{RS}, t_L. The correlations between these temperatures and the heater temperature t_H at the point of installation of the cost allocator, as well as the ambient temperature t_L were determined.

The temperature t_H has the greatest correlation to the temperature t_{HS} = 0,996; however, the coefficient of determination R2 of the linear trend line for t_{HS} is 0.992. This indicates a high degree of convergence in the data, but the temperatures t_H and t_{HS} are different.

The greatest correlation with the ambient temperature (t_L) is with the external sensor temperature (t_{RS}), with a coefficient of determination (R^2) of 0.962. However, the temperatures (t_L and t_{RS}) are different.

The temperature measured by the electronic divider's sensors (t_{HS} and t_{RS}) is primarily dependent on the surface temperature (t_H) of the heater at the installation site. By contrast, the ambient temperature (t_L) varies over a relatively small range and has a smaller impact on the values recorded by the allocator.

Temperatures follow the inequalities $t_H > t_{HS} > t_{RS} > t_H$, and no anomalies caused by disruptive factors have been identified.

Acknowledgments
The authors gratefully acknowledge the financial support for this work from the Ministry of Science and Higher Education of Poland under grant No. W/WB-IIŚ/2/2022 *of Bialystok University of Technology.*

References

[1] PN-EN 834:2013-12. (2013). Heat cost allocators for the determination of the consumption of room heating radiators – Appliances with electrical energy supply.

[2] EN 834:2013 / AC:2015. (2015). Heat cost allocators for the determination of the consumption of room heating radiators – Appliances with electrical energy supply.

[3] Bargłowski, L., Adamski, M., Rebman, M. (2023). Analysis of structural solutions for radiators in buildings. *Civil and Environmental Engineering Reports*, *33*(1), 139–149. https://doi.org/10.59440/ceer-2023-0010

[4] Michnikowski, P., Skiba, J. (2014). Test the Settlement of Individual Heating Costs on the Basis of Indications Radiator Electronic Allocators (Testy poprawności rozliczania indywidualnych kosztów ogrzewania na podstawie wskazań nagrzejnikowych podzielników elektronicznych). *Ciepłownictwo, Ogrzewnictwo, Wentylacja*, *45*(9), 347–351. https://doi.org/10.13140/RG.2.2.25432.98562

[5] Michnikowski, P., Grzywacz, M. (2015). Validation of heat cost accounting based on allocators indications (Sprawdzanie poprawności rozliczania kosztów ogrzewania na podstawie wskazań podzielników). *Rynek Instalacyjny,1–2*, 71–74.

[6] Adamski, M., Bargłowski, L., Rebman, M. (2022). Standards PN-EN 834 for Electronic Heating Cost Distributors (Normy PN-EN 834 dotyczące elektronicznych podzielników kosztów ogrzewania). *Ciepłownictwo, Ogrzewnictwo, Wentylacja*, *53*(10), 36–38. https://doi.org/10.15199/9.2022.10.6

[7] Bargłowski, L., Adamski, M. (2024). Central Heating Control Charts for the Economic Use of Energy in Residential Buildings. *Civil and Environmental Engineering Reports*, *34*(3), 1–15. https://doi.org/10.59440/ceer/190249

[8] Adamski, M. (2017). Radiator temperature field and recorded heat (Pole temperatury powierzchni grzejnika a wskazania podzielnika kosztów). *Ciepłownictwo, Ogrzewnictwo, Wentylacja*, *48*(10), 418–422. https://doi.org/10.15199/9.2017.10.6

[9] Adamski, M., Bargłowski, L. (2024). Testing the linearity of values recorded by the cost allocator (pp. 256–259). In *Збірник наукових праць: XVII Міжнародної науково-практичної конференції академічна й університетська наука: Результати та перспективи*. Полтавська політехніка імені Юрія Кондратюка.

[10] Bargłowski, L., Adamski, M., Furdas, Y., Myroniuk, K., Zhelykh, V. (2025). Analysis of Changes in Heat Consumption in the Developing Housing Estate. *Inżynieria Mineralna*, *2*. https://doi.org/10.29227/im-2025-02-02-012

[11] Adamski, M., Bargłowski, L., Zhelykh, V., Myroniuk, K., Furdas, Y. (2025). Energy Consumption Indicators in Residential Buildings in North-Eastern Poland. *Inżynieria Mineralna*, *2*. https://doi.org/10.29227/im-2025-02-02-101

[12] Kapalo, P., Adamski, M. (2021). The Analysis of Heat Consumption in the Selected City, Lecture Notes in Civil Engineering. In Z. Blikharskyy (Ed.), *Proceedings of EcoComfort 2020. Lecture Notes in Civil Engineering* (Vol. 100, pp. 158–165). Springer. https://doi.org/10.1007/978-3-030-57340-9_20

List of Tables

List of Figures

Politechnika
Białostocka